

UNIVERSITÀ DEGLI STUDI DI ROMA
"TOR VERGATA"

DIPARTIMENTO DI FISICA

DOTTORATO DI RICERCA IN FISICA (XXXIII CICLO)

PH.D. THESIS

**Calibration of the HEPD detector
on board CSES and preliminary
analysis on galactic proton flux**

Author:

Luca CARFORA

Supervisor:

Prof. Roberta SPARVOLI

Co-supervisor:

Dr. Alessandro SOTGIU

Coordinator:

Prof. Roberto BENZI

A.A. 2020/2021

Introduction

This work reports my activity as Ph.D. student in the framework of the Limadou experiment High Energy Particle Detector (HEPD), installed on board the Chinese Seismo-Electromagnetic Satellite (CSES), and my contribution to the instrument data validation and data analysis in cosmic ray physics.

The interest in cosmic ray physics was always of primary importance in the astrophysics field for a better understanding of our Universe; in particular their origin and propagation were deeply studied, but acceleration mechanisms and cosmic ray sources are still mostly unknown. Furthermore, the antiparticle components in cosmic rays allow to obtain information about other astrophysical open questions, such as dark matter composition.

CSES is one of the latest experiments involved in this topic. It is a scientific mission devoted to studying and monitoring electromagnetic field and waves, plasma and particle perturbations of atmosphere, ionosphere and magnetosphere induced by natural sources and anthropogenic emitters and their correlation with the occurrence of seismic events; in this scientific framework, the main objectives of CSES are the investigation of Van Allen belts stability, the study of the radiation environment around Earth in solar quiet conditions and during solar impulsive phenomena, like CMEs or solar flares, the measurements of cosmic rays for comparison with other flying space missions like PAMELA and AMS, space weather measurements in the incoming 25th solar cycle. The satellite mission is part of a collaboration program between the China National Space Administration (CNSA) and the Agenzia Spaziale Italiana (ASI). The satellite was successfully launched from the Jiuquan satellite launch center in the Gobi Desert (inner Mongolia, China) by the Chinese rocket Long March 2C on February, 2nd 2018.

The HEPD is one of the scientific payloads installed on CSES; it was projected, developed and integrated by the Italian members of CSES mission (CSES-Limadou collaboration). The Limadou project is funded by ASI and INFN (Istituto Nazionale di Fisica Nucleare), through a collaboration that includes several INFN Divisions (Bologna, Napoli, Perugia, Roma Tor Vergata), the INFN Center TIFPA of Trento, the INFN Laboratori Nazionali di Frascati, the Universities of Roma Tor Vergata, Trento, Uninettuno and the

Institutes INAF-IAPS (Istituto Nazionale di Astrofisica e Planetologia) and INGV (Istituto Nazionale di Geofisica e Vulcanologia).

In particular, the HEPD is a particle detector able to identify the particle type, measure the direction of the particle to establish the angle between its trajectory and the Earth magnetic field (pitch angle) and detect its energy. The high-inclination orbit allows the instrument to detect particles of different nature during its revolution: galactic cosmic rays, SEPs, particles trapped in the magnetosphere. It was designed to provide electron rates in the energy range 3-100 MeV, proton rates in the energy range 30-200 MeV and light nuclei. Its scientific goals are the study of low-energy cosmic rays, Van Allen belt stability and solar phenomena like CMEs, SEPs and the monitoring of the solar modulation.

Author's contribution

During my Ph.D. course of three years, I have participated to the simulation software and to the data analysis of the High Energy Particle Detector (HEPD), with several contributions listed below.

At the beginning of my Ph.D. course, I contributed to the improvement of the Monte Carlo (MC) software of the instrument, realizing a user-friendly structure for the output file and supporting in simulation analysis. In particular, my personal contribution in the first period was to identify the main features of the calorimeter (like acceptance and particle discrimination). Moreover, I worked on MC physics list packages to select the most suitable for space application experiments and in particular for the physics of HEPD.

On February 2nd, 2018 the CSES satellite was successfully launched and some hours later the HEPD was turned on for a health check of sub-detectors and electronics. The check was followed by a commissioning phase, in which I was personally involved with numerous other members of Limadou project, held at the Institute of Crustal Dynamics (ICD) in Beijing, China. The aim of this period, lasted from February to May 2018, consisted in verifying the HEPD status and its stability over time and choose the optimal trigger configuration for the HEPD data taking.

Before launch, some beam tests had been developed on the Flight Model of HEPD with protons, electrons and atmospheric muons. In this framework, my work on the MC software consisted in realizing several configurations of HEPD, each one devoted to a particular beam test, and a particular configuration for the simulation of flight conditions. I then used this configurations to simulate the beam test response of the detectors, in energy and light yield, and to compare it to real data PMT signals. The last effort in this task was the creation of a software to make MC output as similar as possible to the detector one, but containing also the event-by-event MC truth info.

The contribution that I carried on at this point, and which turned out to be crucial for data analysis and flux estimation, was the digitization of the MC software. The idea consisted in tuning the simulation on the PMT response of the HEPD Flight Model to the beam tests, in order to have a MC able to reproduce also PMT response. To achieve this goal I implemented the

Geant4 optical physics list in the MC and studied the elements involved in the generation, transport and collection of the optical photon inside scintillators and at PMT window. Particular attention was given to the parameters of the scintillating materials, of the scintillator wrapping surface and of the geometry and quantum efficiency of the PMT.

The development of the MC digitization was crucial for several steps in the subsequent data analysis; without an instrument redundancy for the measurement of same quantity, the only way to check the detector response or study efficiencies of selection cuts is to use the MC. MC truth can provide a general description of performance, but for a higher precision, only digitization can include electronic or physical effects (such as saturation, light transport or PMT collection). I was then engaged in the event reconstruction chain, and I worked in particular to the development of a cross-check method for energy calibration, based on the exploitation of last plane hit by the event, and on data analysis using digitized MC runs.

I was finally involved in a preliminary analysis of cosmic rays fluxes, partly reported in this thesis. A fine analysis was conducted with the help of MC digitization for defining the event selections and particle identification; after calculation of selection efficiencies, geometrical factor and live time, I focused on the calculation of galactic protons flux and compared the obtained results with models and measurements from other satellite and balloon experiments. My presence at North-West University in Potchefstroom, South Africa was fundamental for analysis exchange ideas with groups involved in other CR experiments (PAMELA and AMS-02, for instance) and for the opening to international scientific community.

A parallel work during my Ph.D. consisted in the development of a Monte Carlo particle software, programmed for a second detector belonging to the long-term CSES mission programme. The CNSA foresees in fact for next decades several other missions following CSES-01, consisting in satellites for seismo-electromagnetic studies; each of them will contain a particle package. In the framework of a collaboration program between CNSA and ASI, the particle package for next mission (CSES-02) was assigned to Limadou collaboration, which has decided to name the detector HEPD-02, in continuity with the previous one. Indeed, this particle detector shares with HEPD-01 most of scientific objectives, and foresees some important optimizations in order to improve low-orbit and Earth atmosphere observations.

Outline of the Thesis

This work presents HEPD in the theoretical reference frame of the experiment, as part of the CSES mission. It describes in detail the energy reconstruction of an event, highlighting the importance of MC software and digitization in calibration and data analysis. Finally, some of the first results of proton fluxes in the context of cosmic ray physics are reported.

The 1st chapter of this work describes the physics reference frame of the experiment HEPD. It illustrates the main features of cosmic ray physics and GCR (Galactic Cosmic Rays), including origin, propagation and solar modulation; a general description of the main scientific objectives of CSES, such as Van Allen belts and solar physics, is given.

In the 2nd and 3rd chapter, general outlines of CSES mission and of the HEPD experiment are exposed respectively. Chapter 2 presents the general features of CSES, together with an overall description of its payloads. Chapter 3 focuses on the HEPD instruments geometry, electronics and general functioning mode.

Chapter 4 introduces the Monte Carlo software of the experiment, to which I personally worked, with particular mention to the digitization procedure and its importance in the data analysis; the energy reconstruction follows, explaining in detail beam test data analysis and calorimeter calibration.

Chapter 5 presents the event selections for a galactic proton flux, together with the geometrical factor, the selection cut efficiencies, the live time and the galactic selections. Some preliminary results about the data analysis on cosmic ray fluxes are presented, too, in particular on galactic protons in the energy range observed by HEPD.

After conclusions, showing a general review of objectives highlighted in this thesis and results reached with this work, a final chapter is dedicated to the HEPD-02 project, a particle detector foreseen in the CSES-02 mission; a description of its geometry and of the construction of the corresponding MC is explained in detail, showing in particular some structural improvements with respect to HEPD-01 for a full achievement of its scientific objectives.

Contents

Introduction	iii
Author's contribution	v
Outline of the Thesis	vii
1 Cosmic Rays Physics	1
1.1 Cosmic rays	1
1.1.1 Spectrum and composition of primary cosmic rays	2
1.1.2 Origin of cosmic rays	4
1.1.3 Propagation	6
1.1.4 Modulation	8
1.2 Van Allen belts	11
1.3 Solar physics	12
2 The CSES mission	15
2.1 General features	15
2.2 Scientific objectives	17
2.2.1 Stability of the Van Allen belts	17
2.2.2 Litosphere-ionosphere-magnetosphere coupling	18
2.2.3 Solar physics	22
2.2.4 Space weather	23
2.3 The satellite	24
2.4 The payloads	27
3 The High Energy Particle Detector	33
3.1 Detector instruments	34
3.1.1 The detectors	36
Silicon detector	37
Trigger detector	37
Calorimeter	38
Veto detector	39
Photo Multiplier Tubes	43

3.1.2	The power supply	44
3.1.3	The electronics	46
	CPU board	47
	TM/TC Power Control board	47
	PMT/Trigger board	48
	DAQ board	48
3.2	Operation modes and in-flight calibration	49
3.3	Trigger configurations and orbit settings	51
3.4	Beam test	53
4	Monte Carlo software and energy reconstruction	57
4.1	Monte Carlo software	57
	4.1.1 Code structure	58
	4.1.2 Configurations	60
	4.1.3 HEPD simulated performances	61
4.2	Digitization procedure	65
4.3	Beam test calibration	74
	4.3.1 Equalization	75
	4.3.2 Calorimeter energy calibration	75
4.4	Range energy reconstruction	80
4.5	Machine learning reconstruction	84
5	Flux measurement	87
5.1	Event selections	87
	5.1.1 Particle type selection	89
5.2	Efficiencies	93
5.3	Unfolding	97
5.4	Galactic selection	101
5.5	Live time	102
5.6	Flux estimation	103
	Conclusions	107
	The HEPD-02 project	111
	Bibliography	131

List of Figures

1.1	All particle flux	3
1.2	Particle fluxes	5
1.3	Solar modulation	9
1.4	Earth magnetic field	9
1.5	Particle "magnetic bottle" in Earth magnetic field	11
1.6	AP8 and AE8	12
1.7	Solar physics	13
1.8	Solar flare	14
2.1	CSES and its payloads	16
2.2	Coupling mechanism	18
2.4	CSES - dimensions	25
2.5	CSES	26
2.6	SCM	28
2.7	EFD	29
2.8	Langmuir probe	30
2.9	HEPP	31
3.1	HEPD design	34
3.2	HEPD connections	35
3.3	HEPD detectors	36
3.4	HEPD silicon	37
3.5	HEPD trigger	37
3.6	HEPD calorimeter	38
3.7	HEPD LYSO cubes	39
3.8	EJ-200 emission spectrum	41
3.9	LYSO emission spectrum	42
3.10	LYSO radioactivity spectrum	43
3.11	Hamamatsu PMT features	44
3.12	Electronics block diagram	45
3.13	Electronics box	46
3.14	CPU board	47

3.15 EASIROC	48
3.16 DAQ	48
3.17 HEPD trigger rate	52
3.18 Beam spot electrons	53
3.19 Beam position electrons	54
4.1 HEPD MC geometry	59
4.2 HEPD MC proton configuration	61
4.3 Optical photons chain	62
4.4 HEPD minimum and maximum range simulated	63
4.5 Geometrical factor definition	64
4.6 Geometrical factor	65
4.7 Particle discrimination	66
4.8 Distribution of PE and ADC for digitization.	67
4.9 Silicon test beam analysis	69
4.10 MC digitization	71
4.11 MC digitization compare	72
4.12 GF with optics	74
4.13 Position reconstruction using MC	76
4.14 Tower calorimeter signal	78
4.15 Tower calorimeter calibration curve	79
4.16 LYSO calorimeter calibration curve	80
4.17 Energy range distributions	81
4.18 Energy range curve	82
4.19 Last plane electrons	83
4.20 Range calibration comparison	83
4.21 ML scheme	84
4.22 NN and test beam comparison	85
5.1 Event selection	89
5.2 Particle discrimination using digitized MC	90
5.3 Particle discrimination with beam tests	91
5.4 Particle discrimination profile proton	92
5.5 Particle discrimination profile electron	92
5.6 Particle discrimination with NN	93
5.7 Particle discrimination flight data	94
5.8 Proton identification efficiency	96
5.9 Unfolding test	98
5.10 Interacting protons	99

5.11	Interaction points	99
5.12	Longitudinal profile of interacting proton	100
5.13	Smearing matrix for unfolding	100
5.14	Cutoff map	102
5.15	HEPD hydrogen flux	104
5.16	HEPD hydrogen flux	105
5.17	HEPD hydrogen flux	105
5.18	HEPD hydrogen fluxes	106
19	CSES-02 satellite	112
20	HEPD-02 CAD design	114
21	HEPD-02 frontal view	114
22	HEPD-02 tracker	116
23	HEPD-02 Monte Carlo project	117
24	HEPD-02 simulated event e 30 MeV	118
25	HEPD-02 minimum and maximum energy range	119
26	HEPD-02 energy release	120
27	HEPD-02 energy release	121
28	HEPD-02 MIP energy release	122
29	HEPD-02 multiple scattering	123
30	HEPD-02 reconstructed energy fraction	124
31	HEPD-02 Alpide geometric inefficiency	125
32	HEPD-02 LYSO radioactive photons	126
33	HEPD-02 LYSO radioactive electrons	126
34	HEPD-02 LYSO energy deposition	127

List of Tables

2.1	HEPP parameters	31
3.1	EJ-200 properties	40
3.2	LYSO properties	41
3.3	Beam spot protons	55
4.1	HEPD MC materials	58
5.1	Plane efficiency	96
2	HEPD-02 requirement	113

Chapter 1

Cosmic Rays Physics

One of the most relevant topics in Particle Physics research concerns the origin, propagation and acceleration mechanisms of cosmic rays. Since their discovery, in the first years of XX century, numerous experiments have been built up to better understand cosmic charged particles, whether directly coming from outside the Solar System, or originating by interactions in Earth atmosphere. Nowadays, a strong effort in this field is not only spent to deduce general behaviours of cosmic ray fluxes, but it is also employed in the possibility of studying the near-Earth environment and associated phenomena: space weather, Earth magnetic field, heliosphere dynamics.

In this chapter, a brief description of spectra and composition of cosmic rays is given, with particular attention to actual hypothesis about their propagation and trapping mechanisms around Earth (particle drift and modulation).

1.1 Cosmic rays

Cosmic rays have been studied for the first time in 1912 by Victor Hess (Hesse, 1912). Until that, it was believed that radiation measured at sea level was emitted from Earth surface; in his balloon experiments, Hess actually discovered that radiation intensity decreases up to 1500 m from ground, but increases after that. The term "cosmic rays" was firstly used in 1926 by Millikan to indicate the extraterrestrial ionizing radiation; now it indicates all charged particles entering in the Earth atmosphere from space, and often is extended to include high-energy photons or neutrinos. The first observations of single-track cosmic rays became possible with the invention of Wilson cloud chambers in first years of XX century; hence, the positron and the muon were respectively discovered in 1932 and in 1937 and, until the advent of accelerator machines, physicists used cosmic rays for the newly born field of elementary particle physics. After that, the interest in cosmic rays was focused on their origin, acceleration mechanisms and propagation from sources to Earth.

1.1.1 Spectrum and composition of primary cosmic rays

Cosmic rays include all stable charged particles and nuclei. In an astrophysics context, they are divided in two categories: a particle produced at an astrophysical source and accelerated in the Galaxy is defined "primary", while a particle produced after an interaction of a primary with the interstellar medium is a "secondary". Thus, electrons, protons, helium and a little percentage of carbon, oxygen, iron and other nuclei synthesized in stars, are primary particles; nuclei that are not abundant end-products of stellar nucleosynthesis (such as lithium, beryllium and boron) are secondaries; in fact, these elements show a different relative abundance with respect to their abundance in the Solar System. Also antiprotons and positrons are in large part secondary; an actual open question in astroparticle physics is whether a small fraction of these particles may be primary.

Two important quantities describe the spectra of the cosmic radiation. The magnetic rigidity is the gyroradius r_L of the particle multiplied by the magnetic field intensity B or, in the same way, the momentum of the particle p per charge unit Ze :

$$R = \frac{pc}{Ze} = r_L B \quad (1.1)$$

and is an alternative way to refer to the particle energy; it is typically expressed in GV .

The differential flux Φ is defined as the number of particles of a given type dN per unit area dA , measure time dt , solid angle $d\Omega$ and energy dE :

$$\Phi(E) = \frac{dN}{dA dt d\Omega dE} \quad (1.2)$$

The flux of primary nucleons in the energy range from several GeV to something beyond 100 TeV is proportional to

$$\Phi_N(E) \propto (E/1\text{GeV})^{-\alpha} \frac{\text{nucleons}}{\text{m}^2 \text{s sr GeV}} \quad (1.3)$$

where E is the energy-per-nucleon (including rest mass energy) and α is the differential spectral index of the cosmic ray flux; its value is approximately 2.7 in this energy region.

Composition and energy spectra of particles and nuclei in cosmic rays are generally interpreted in terms of generation, propagation and acceleration models, in which the sources of the primary cosmic radiation are located within the Galaxy (A. W. Strong, 2007).

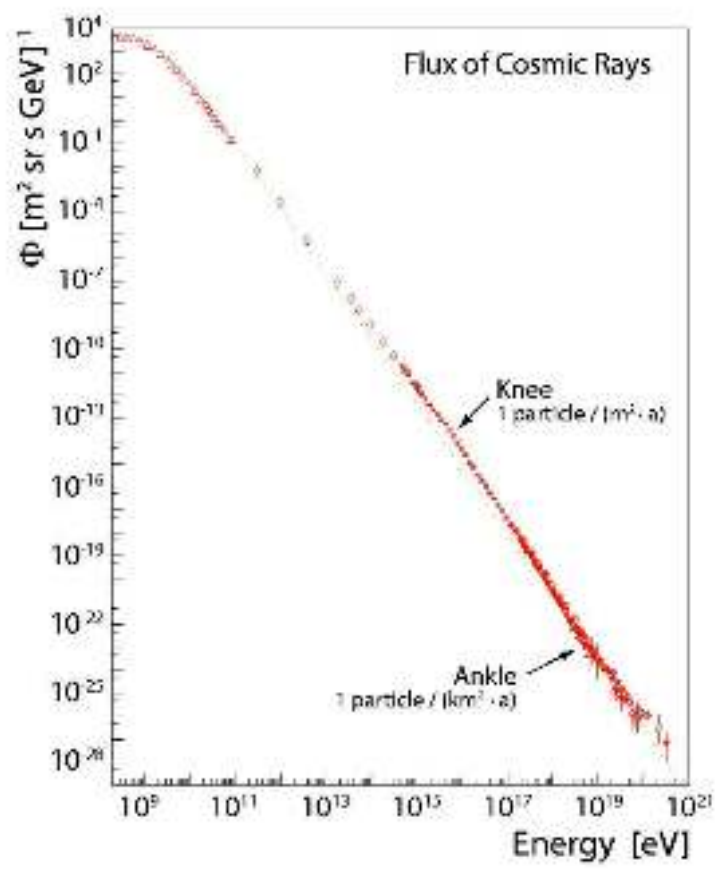


FIGURE 1.1: Differential all-particle flux of the highest-energy cosmic rays.

Fig. 1.1 shows the spectrum of all the different components summed together (the "all-particle" spectrum) up to the highest measured energies; today, this spectrum is known with good precision up to $\sim 10^{19}$ eV; the differential spectral index α for the all-particle spectrum depends on the energy region. The maximum around some hundreds MeV/nucleon is explained by the domination at low energy of the solar modulation, due a combined effect of solar wind and Earth magnetic field; in the energy region 10^9 - 10^{15} eV the measured spectral index is about 2.7; then the spectrum steepens at higher energies with a spectral index of 3, and above $5 \cdot 10^{18}$ eV the spectrum flattens with spectral index 2.8. These behaviors of the cosmic ray spectrum curve are respectively called "knee" (at $\sim 10^{16}$ eV) and "ankle" (at $\sim 5 \cdot 10^{18}$ eV); the reason for their existence is not well understood yet, but it is commonly believed that this changes in the power law are probably related to different mechanisms of particle acceleration and propagation.

About 74% of the primaries are protons and about 70% of the rest are nucleons bound in helium nuclei. Fig. 1.2 shows the major components of primary cosmic rays in particles per energy-per-nucleus. Actually, the composition of cosmic rays depends in general on the energy range considered: for example, below 1 TeV, where direct measurements exist, percentages are about 85% of protons, 15% helium nuclei and less than 1% electrons and minor abundances of heavier nuclei and antiparticles.

Because of the wide range of cosmic-ray spectra and of the large variation in the particles number, different kinds of experimental techniques were adopted to perform measurements in different energy regions. Direct measurements of cosmic rays can be done by means of detectors on board of aerostatic balloons or satellites, with the highest energy measurable of about 10^{15} eV; at higher energies the rate is too low, and the technique consists in the study of the showers of particles produced by the interaction of primary cosmic rays with the atmosphere: ground-based large-array detectors and fluorescence detectors (like ARGO-YBJ and the Pierre Auger observatory) are used to investigate the higher energy region.

1.1.2 Origin of cosmic rays

Standard theories on the origin of cosmic rays state that most of the non-solar component is produced by the shock waves existing in the regions around supernovae explosions inside our galaxy. Spectrum and composition of cosmic rays for energies up to the knee is compatible with a production of the

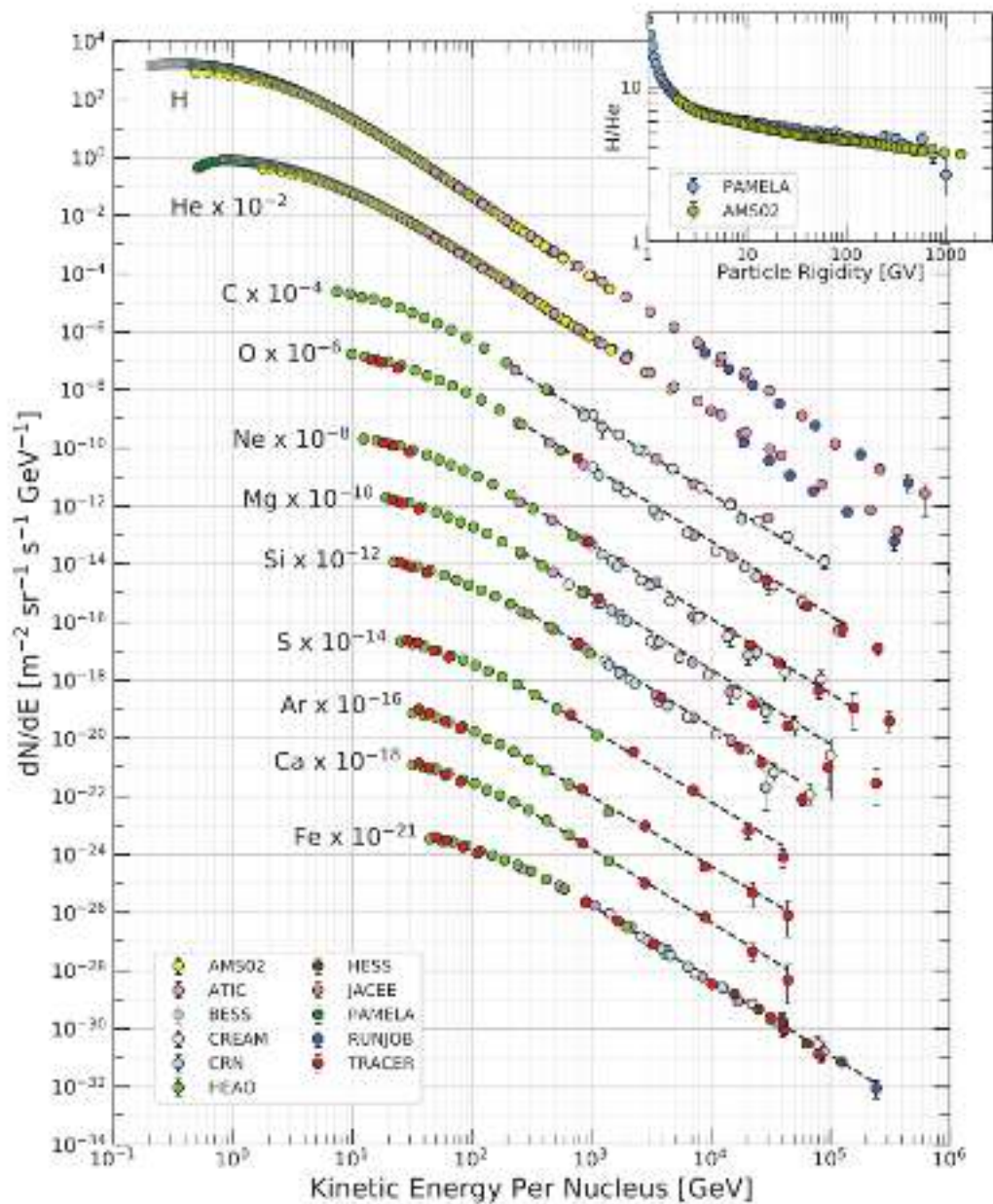


FIGURE 1.2: Fluxes of nuclei in the primary cosmic radiation in particles per energy-per-nucleus are plotted vs energy-per-nucleus using data from ((PAMELA Collab.), 2011; (AMS02 Collab.), 2015b; (BESS Collab.), 2016; (JACEE Collab.), 1998; (ATIC Collab.), 2009; (RUNJOB Collab.), 2005; (CREAM Collab.), 2009; (HEAO3-C2 Collab.), 1990; (CRN Collab.), 1991; (TRACER Collab.), 2008; (HESS Collab.), 2007) The inset shows the H/He ratio at constant rigidity ((PAMELA Collab.), 2011; (AMS02 Collab.), 2015a)

nuclei in supernovae explosions and with a successive acceleration using the so called "Fermi mechanism". This mechanism was proposed in 1949 by E. Fermi (Fermi, 1949) and is based on the assumption that particles in collision with macroscopic moving objects, such as magnetic fields in shock waves of supernovae, could undergo repeated finite energy gains. It states that at each interaction the particle gains a fraction of its initial energy and eventually escapes the acceleration region with a certain probability, which depends on its energy. This model naturally predicts the observed spectral shape and the fact that the maximum energy which the Fermi mechanism can give to a nucleus increases with its charge. As a consequence, cosmic-ray composition becomes heavier around and above the knee, since heavier elements may be accelerated to higher energies. According to this scenario the lower-energy change in the spectral index at the knee could reflect the fact that some of the galactic accelerators of cosmic rays have reached the upper limit beyond which the process no longer provides particles in an efficient way.

The Fermi model cannot explain particles with energy greater than 10^{18} eV. The origin of the highest portion of the spectrum remains unclear but several possible explanations have been proposed, suggesting for example that the cosmic rays above the ankle could have origin from extragalactic sources. There are only 4 classes of objects able to accelerate particle above 10^{20} eV: high magnetic field neutron stars, Active Galactic Nuclei (AGN), lobes of giant radio galaxies and Gamma-ray bursts. All these sites are characterised by strong magnetic fields or by large physical dimensions. Recent measurements (The Pierre Auger Collab., 2007) found a correlation with nearby AGN, favouring these kind of object as sources of cosmic rays with $E > 10^{19}$ eV. Also (Peretti E. et al., 2019) demonstrates that the most significant candidates are star burst galaxies.

1.1.3 Propagation

Observed cosmic-ray particles are produced somewhere in the galactic volume and maybe, for extremely high energy component, also in extragalactic sources. Then, on their way on Earth, they are involved in many kinds of processes, such as scattering off the interstellar medium and interaction with magnetic fields. The immediate consequence is that cosmic rays lose their original direction (they are isotropized) and energy. A careful study of the propagation models in the galaxy is needed in order to compare the observed data with those expected according to some theoretical production rate.

The process of propagation of charged particles in the galaxy can be modeled as a random walk, which can be described by the following diffusion equation:

$$\frac{\partial N}{\partial t} = \nabla \cdot (D \nabla N - \vec{u} N) - \frac{N}{\tau_{esc}} - \frac{\partial}{\partial E} (b(E) N) + Q \quad (1.4)$$

where $N = N(\vec{r}, t, E)$ is the cosmic-ray number density with energy E at a point \vec{r} and time t and $Q = Q(\vec{r}, t, E)$ is their source number density. The first term on the right hand side contains the diffusion coefficient D and the velocity \vec{u} of convective particle transport in the galaxy. The second term represents the losses of particles by collision and decay with a mean escape time τ_{esc} . The third term describes the energy variation through the energy loss rate $b(E) = dE/dt$. This term depends strictly on the nature of the propagating particle. In fact, while for hadrons the energy loss is mainly due to ionization, electrons and positrons, because of their small masses, suffer large radiative losses through Bremsstrahlung emission, inverse-Compton scattering with the ambient photons and synchrotron radiation in the magnetic field. Their relative importance depends in the electron energy expressed through $\gamma = E/m_e c^2$ for relativistic particles, in details

$$b(E) = A_1 \ln \gamma + A_2 \gamma + A_3 \gamma^2 \quad (1.5)$$

The first term describes ionization losses which have a logarithmic dependence on the energy; the second term accounts for Bremsstrahlung losses; the third for inverse Compton and synchrotron losses. The last processes dominate over ionization and Bremsstrahlung energy losses for electron energy greater than 1 GeV.

The most frequently used models are the leaky box model and the diffusion model. In the first one, the sources of cosmic rays are uniformly distributed in the galactic disk, which is surrounded by the halo, and they diffuse freely in a confinement volume: at each encounter with its boundary they can be reflected and the probability per unit of time of escaping into intergalactic space is constant. The diffusion model is based on the assumption that sources and matter are located in the galactic disk, then they diffuse through the disk and the halo and escape freely from the boundary. This model takes into account the spatial properties of the Galaxy (its structure, the spatial distribution, the interstellar radiation and the magnetic fields), so it is more realistic than the leaky box model.

1.1.4 Modulation

Radiation environment on Earth consists of galactic cosmic rays, solar particles and trapped particles, which vary in time and with geographical position; the fluxes of these populations are modulated by two processes: the solar activity and the Earth magnetic field.

Solar activity is measured using the number of solar sunspots that appear periodically on Sun surface; when the Sun shows a greater number of sunspots, the Sun is in a phase of maximum activity and emits major energy in the outer space. The solar activity is variable in time with a period of 22 years; it varies from a maximum level to a minimum and then returns to a maximum in 11 years, then there is a reversion of the magnetic field (J. F. Valdés-Galicia, 2016). This cyclic activity causes an effect called solar wind, a continuous flow of plasma, mainly composed by low-energy electrons and light ionized nuclei, coming out from the sun corona; it travels with a speed ranging from 300 to 800 km/s and extends out beyond Pluto. This plasma movement originates the interplanetary magnetic field because it carries the solar magnetic field into the solar system.

The interstellar cosmic rays entering in the solar system interact with the solar wind and the magnetic field deflects the low-energy component of the incoming particles. This results in a variation of the flux that was experimentally established to be strongly anti-correlated with the Sun activity: the higher is the production of solar particles, the lower is the number of galactic cosmic rays capable of reaching the Earth. Solar cycles are tracked since 1755, following the original numbering proposed by Wolf in the mid-19th century (Kane, 2002): the 24th solar cycle began in December 2008 and the solar maximum was reached in April 2014; sunspot numbers in polar regions in December 2016, April 2018 and November 2018 indicate that a transitional phase to solar cycle 25 is in progress (see Fig. 1.3).

The effect of solar modulation depends on the energy of the particle; in particular, it decelerates incoming low-energy particles and excludes some of them with energies below 1 GeV, while the effect becomes negligible above ~ 10 GeV.

Sun activity is not limited only to solar wind modulation; other short-time events contribute to the cosmic-ray spectrum, for example bursts of energetic particles up to some tens of GeV emitted during solar flares or coronal mass ejections.

Another contribution to the cosmic-ray spectrum modulation is the Earth magnetic field influence. In the vicinity of the Earth its magnetic field can

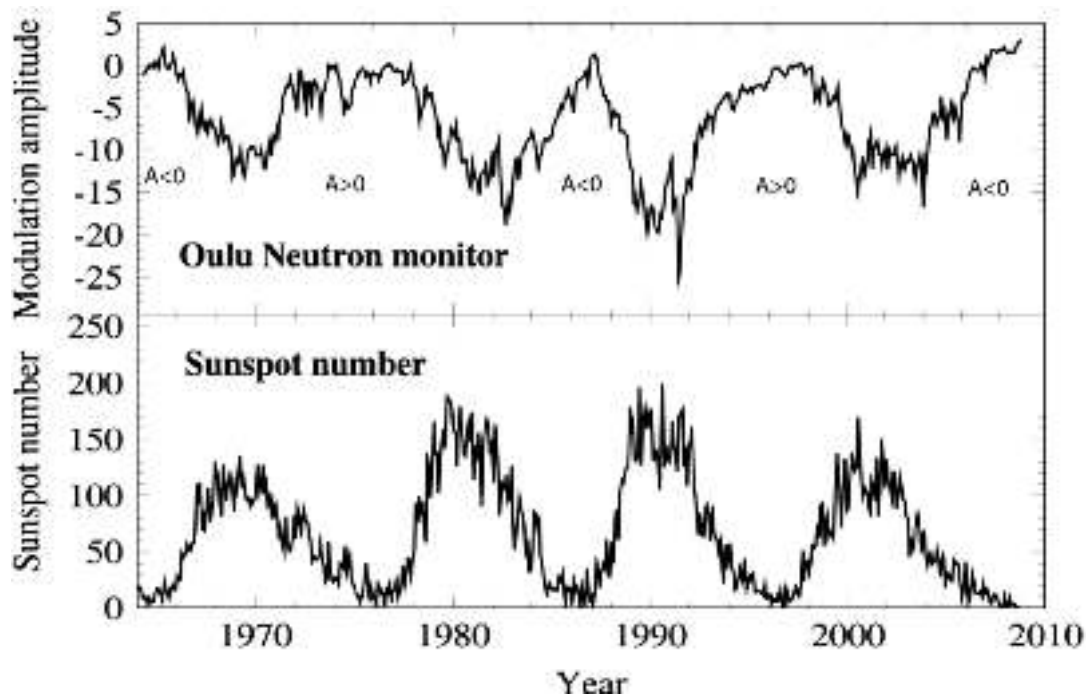


FIGURE 1.3: Anti-correlation between cosmic ray intensity, measured by Oulu neutron monitor, and the sunspot number (B. Heber et al., 2009).

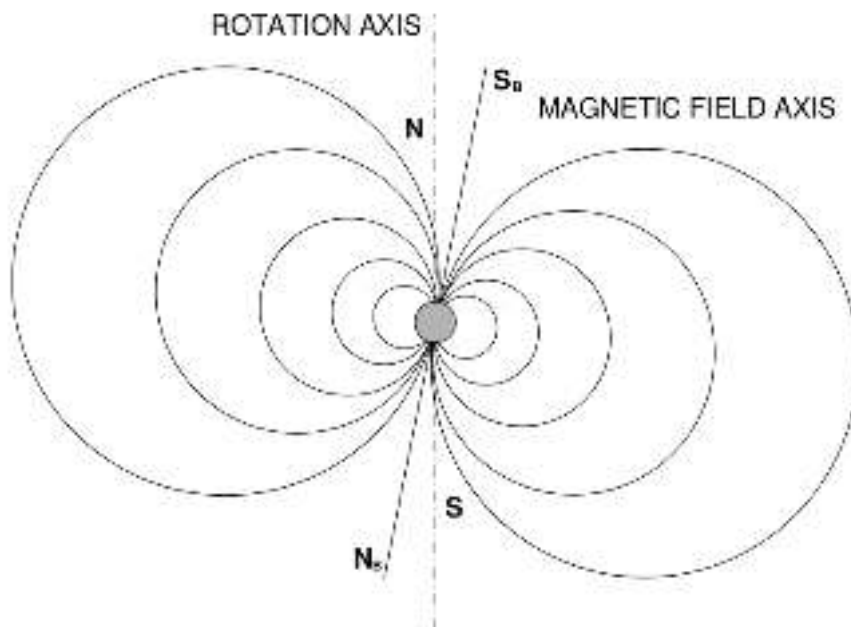


FIGURE 1.4: Earth dipole magnetic field, showing the inclination of the magnetic axis and the location of magnetic poles with respect to the geographic ones.

be well approximated by a dipole field, as shown in Fig. 1.4. The axis of the dipole is inclined of about 11° with respect to the Earth rotational one, and its magnetic North pole is located somewhere in the southern emisphere. The intensity of the field is given approximately by:

$$B(\lambda, r) \simeq \frac{B_{EQ}}{(r/r_E)^3} \sqrt{1 + 3 \sin^2 \lambda} \quad (1.6)$$

where λ is the geomagnetic latitude, which depends on both geographical latitude and longitude, because of the inclination of the dipole axis, B_{EQ} is the magnetic field intensity at Equator and its value is approximately 0.31 G, r_E is the Earth radius and r is the distance from its center. The geometry and the intensity of the terrestrial magnetic field define the geomagnetic cut-off effect: there exists a minimum momentum that an incoming particle must have in order to reach Earth despite the magnetic field deflection. Rigidity is the best quantity to describe this behaviour, because particles with different momentum and charge but identical rigidity are bent in the same direction with the same curvature by Lorentz force. The vertical geomagnetic cutoff is larger at the equator than in the polar regions; its variation with geomagnetic latitude λ can be approximately described by the following expression (Longhair, 1981):

$$R_{CO} \simeq 14.9 \cdot \cos^4 \lambda (GV/c) \quad (1.7)$$

This is actually an approximation that can be considered highly valid in vertical conditions of the incoming particle; furthermore, the 14.9 coefficient is only effective in a specific time modulation period ((PAMELA Collab.), 2015).

Particles are defined trapped if they are bound in the dipolar terrestrial field because of mirroring in the "magnetic bottle" (see Fig. 1.5). The motion of trapped particles consists of 3 periodic and contemporary movements: gyration around a magnetic field line, movement of the gyration centre along the field (guiding centre motion) and slow longitudinal drift of the guiding centre path around Earth, towards west and east for respectively positive and negative charged particles. The resulting trajectory lies on a toroidal surface, called drift shell, centered on the Earth's dipole centre. Particles confined in a drift shell can also remain there for long periods, even years for protons at altitude of some thousand kilometers.

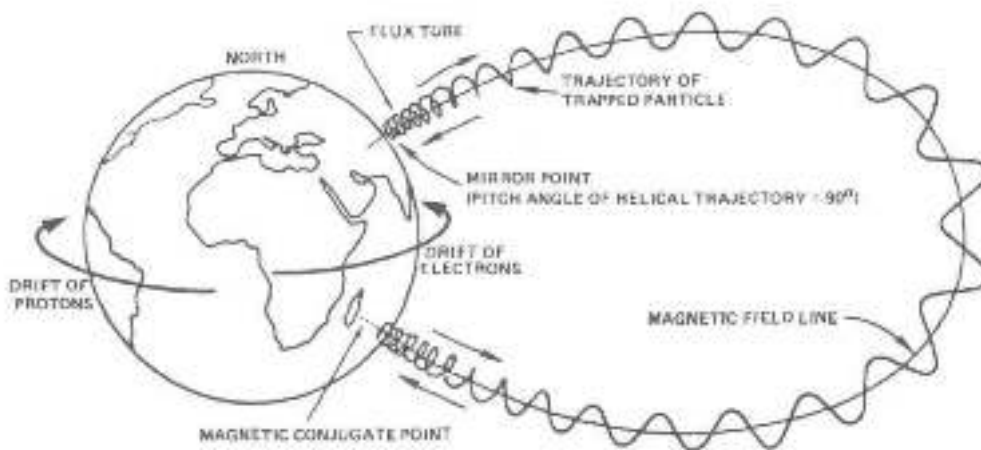


FIGURE 1.5: Particle drift in Van Allen belts.

1.2 Van Allen belts

There exist two stable radiation belts (Van Allen belts, from the name of the American scientist who deduced their existence in 1958, James Van Allen), where trapped particles are mostly concentrated. The outer belt is mainly composed by electrons with energy up to 10 MeV; the inner belt is populated by protons with energies up to few hundreds MeV. There is a region off the coast of Argentina where the inner belt is closer to Earth surface (the region is called South Atlantic Anomaly, SAA) due to the fact that the magnetic field and the belts are tilted compared to Earth rotational axis. Both shape and strength of the radiation belts are modified by Sun activity, but in quiet conditions the inner belt extends typically between 1.5 and 2.5 Earth radii from Earth surface, the outer one from 4 to 6 Earth radii. There is also evidence for the existence of a narrow region centered around altitudes of about one Earth radius containing trapped heavy ions which are believed to be anomalous decelerated cosmic ray particles; the intensities of these ions are several orders of magnitude below the intensities of trapped energetic protons in this region.

Fig. 1.6 shows the distribution of trapped protons with energies above 10 MeV, as predicted by the NASA AP-8 MAX model (D. M. Sawyer, 1976) and of trapped electron population above 1 MeV, from AE-8 MAX model (Vette, 1991), in invariant coordinate space. The region of space covered by higher energy protons diminishes with increasing energies and the location of the highest intensities moves inward.

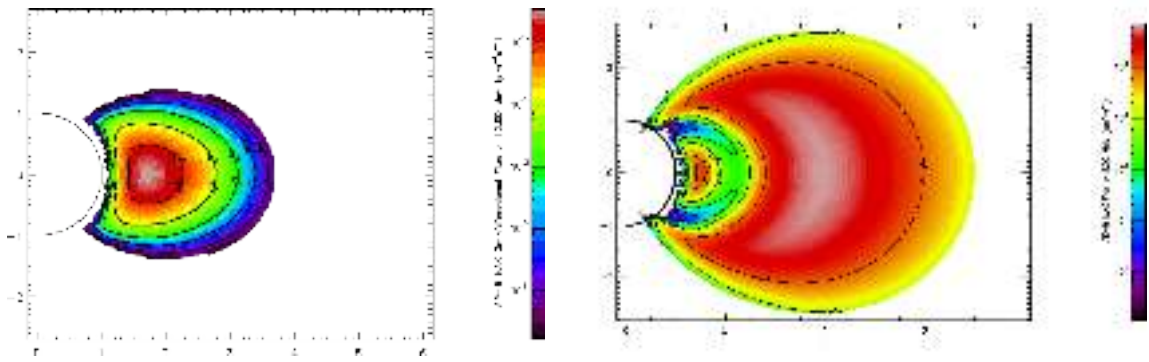


FIGURE 1.6: Left: Invariant coordinate map of the AP-8 MAX integral proton flux > 10 MeV. Right: Invariant coordinate map of the AE-8 MAX integral electron flux > 1 MeV. The semi-circles represent Earth's surface, distances are expressed in Earth radii. (*SPENVIS*)

The outer and inner Van Allen radiation belts are extremely variable in composition, especially when powerful SEPs (Solar Energetic Particles) encounter the magnetic field lines (Piersanti M. and Villante U., 2016). These kind of interactions between cosmic radiation and the magnetosphere generate a set of particles called albedo (upward direction), which can be further identified either as re-entrant (if their trajectory is bent by the geomagnetic field, allowing them to remain trapped with a downward direction) or splash albedo (if they are able to escape the magnetosphere (Treiman, 1953)). The former family comprises quasi-trapped and untrapped particles, depending on whether or not they are confined in the equatorial region below the inner Van Allen belt respectively. New and accurate measurements of the high-energy (>70 MeV) cosmic radiation at LEOs have been reported in ((PAMELA Collab.), 2011) as a function of energy and angle between the magnetic field and the direction of the incoming particle.

1.3 Solar physics

The heliosphere, the region shaped by the presence of the solar wind flowing from the upper atmosphere of the Sun (the corona), presents different levels of variability, some of them still poorly understood. These changes in the solar wind parameters (i.e., density, flow velocity, temperature) lead to the appearance of dynamic phenomena on many spatial and temporal scales (Balogh et al., 2008).

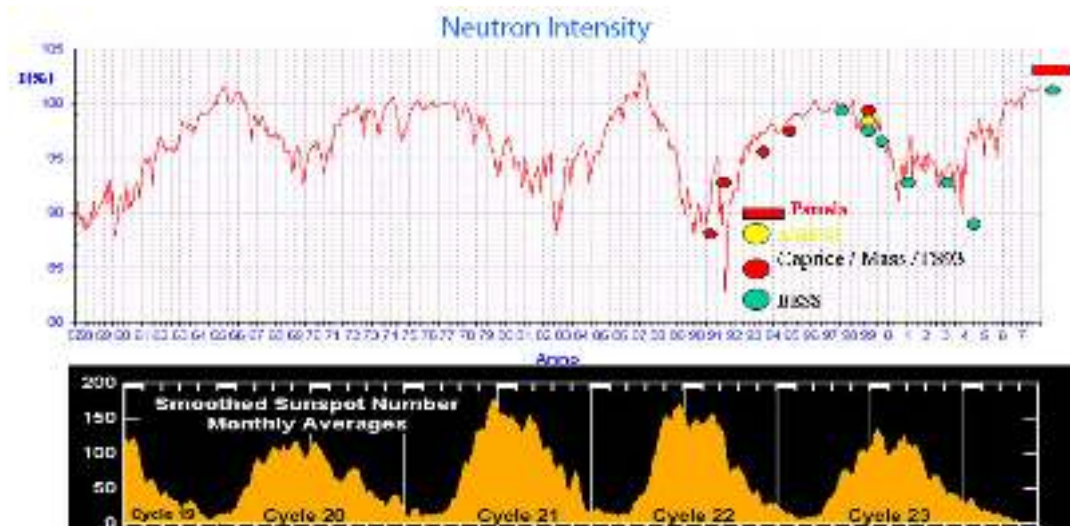


FIGURE 1.7: Neutron intensity percentage measured by PAMELA, AMS, Caprice/Mass/TS93 and BESS and sunspot number function of time.

Because solar activity varies strongly with time, cosmic rays of galactic origin respond to it, generating the so called modulation effect. This is evident in neutron monitor data, which show a clear anticorrelation between particle intensities and solar activity, quantified with the number of solar sunspots (Fig. 1.7). Particles with rigidities up to at least 30 GV are mainly affected and the effect becomes progressively larger as the rigidity decreases.

Solar activity is also characterized by a number of transient phenomena, a wide variety of shorter timescale transients coming from the Sun, such as solar flares and CMEs (Coronal Mass Ejections), when a huge amount of matter and magnetic field is emitted, or solar particle events.

A solar flare (fig. 1.8) is a sudden flash of increased brightness on the Sun, usually observed near its surface and in close proximity to a sunspot group. Powerful flares are often, but not always, accompanied by a Coronal Mass Ejection. Even the most powerful flares are barely detectable in the solar irradiance. Solar flares occur in a power law spectrum of magnitudes; an energy release of typically 10^{20} J of energy suffices to produce a clearly observable event, while a major event can emit up to 10^{25} J. Flares are closely associated with the ejection of plasma and particles through the Sun's corona into outer space; flares also often emit radio waves. If ejected particles are able to escape the Sun magnetic field and the ejection is in the direction of the Earth, these particles, transported through the heliosphere, can penetrate into the ionosphere and cause bright auroras and geomagnetic storms by interacting

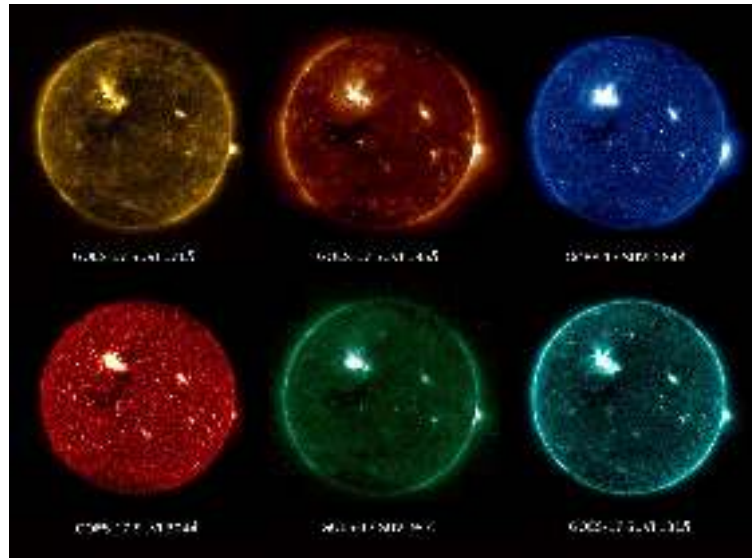


FIGURE 1.8: A C2-class solar flare detected by GOES-17 on May 28, 2018 across different spectral bands.

with the outermost layers of the magnetosphere, with the possibility of disrupting long range radio communication. It usually takes days for the solar plasma ejecta to reach Earth.

Chapter 2

The CSES mission

CSES (China Seismo-Electromagnetic Satellite) is a scientific mission dedicated to studying and monitoring electromagnetic field and waves, plasma and particles perturbations of ionosphere induced by natural sources and anthropogenic emitters and their correlation with geophysics activity.

The satellite mission is part of a collaboration program between the China National Space Administration (CNSA) and the Agenzia Spaziale Italiana (ASI), and is developed by the China Earthquake Administration (CEA) and the Istituto Nazionale di Fisica Nucleare (INFN), together with several Chinese and Italian Universities.

After a general presentation of the mission features, the chapter reports the scientific goals in the fields of Van Allen belts stability, lithosphere-ionosphere coupling, solar physics and space weather. An itemized description of orbit times and periodic data transmission follows. The last part of the chapter is dedicated to a brief report on the nine payloads installed on the satellite.

2.1 General features

The satellite was successfully launched on February 2nd, 2018 and placed at a 97.4° Sun-synchronous circular orbit with an altitude of about 507 km. The satellite mass is about 730 kg and the peak power consumption about 900 W. The expected lifetime of the mission is set to be 5 years.

CSES is based on the Chinese CAST2000 platform and it hosts on board several instruments (Fig. 2.1), among which magnetometers and electric field detector, plasma analyser detectors and several energy particle detectors.

CSES is the first satellite of a space monitoring system proposed in order to investigate the topside ionosphere with the most advanced techniques and equipment in the field. It was designed in order to gather world-wide data of the near-Earth electromagnetic environment. Data collected by the mission allow also studying the radiation environment around the Earth in solar quiet conditions and during solar impulsive phenomena, like Coronal Mass

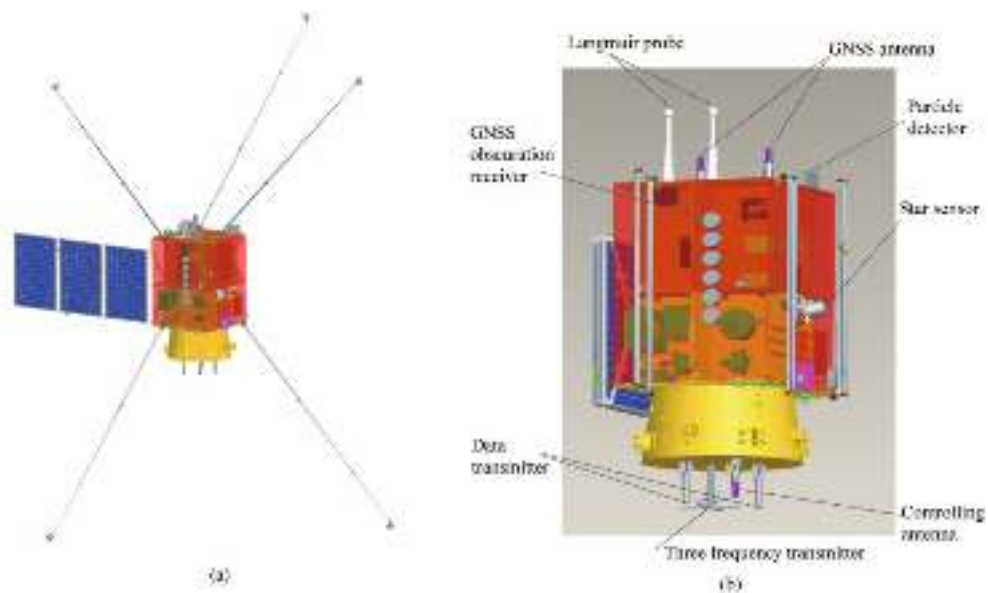


FIGURE 2.1: Configuration of CSES. (a) The satellite platform and (b) the position of scientific payloads.

Ejections (CMEs) or solar flares. CSES can also complement the cosmic-ray measurements of other flying space missions like PAMELA or AMS and compare the particle spectra with those from GOES and ACE missions, up to few hundreds MeV and the cosmic-ray solar modulation. Moreover, CSES is a powerful instrument for space weather measurements in the incoming solar cycle, for the study of magnetic field variation sources and of consequences on terrestrial physics and human activity.

The satellite mission is part of a collaboration program between the CNSA and ASI, and is developed by the CEA and INFN, together with several Chinese and Italian Universities. In particular, Italy participates to the CSES mission with the Limadou project, in honor of the Chinese transliteration of the name of the Italian Jesuit priest Matteo Ricci (1552-1610), acknowledged as one of the most important missionaries in China. The Italian collaboration to the mission was funded by ASI and INFN, through a collaboration that includes several INFN Divisions and universities (Bologna, Naples, Perugia, Roma Tor Vergata), the INFN Center TIFPA (Trento Institute for Fundamental Physics and Applications) of Trento, the INFN Laboratori Nazionali di Frascati, the University of Uninettuno and the Institutes INAF-IAPS (Istituto Nazionale di Astrofisica e Planetologia) and INGV (Istituto Nazionale di Geofisica e Vulcanologia).

2.2 Scientific objectives

As mentioned before, the main scientific goal of CSES is the study and monitor of electromagnetic fields and waves, plasma and particle variations in atmosphere, ionosphere and magnetosphere, perturbed by natural and anthropogenic emitters and study their correlation with geophysics activity (in particular, with the occurrence of seismic events); in this sense, the investigation of Van Allen belts stability is a prominent research field, that has been repeatedly reported in literature by various experiments, though a statistical significance was always difficult to claim (L. Wang et al., 2015; X. Zhang et al., 2013; V. Sgrigna et al., 2005). The mission can also study the radiation environment around Earth in solar quiet conditions and during solar impulsive phenomena, like CMEs or solar flares. Another primary goal is to complement the cosmic-ray measurements of other flying space missions like PAMELA and AMS and compare the particle spectra with those from GOES and ACE missions, up to few hundreds MeV and the cosmic-ray solar modulation. Moreover, CSES is a powerful instrument for space weather measurements in the incoming 25th solar cycle.

2.2.1 Stability of the Van Allen belts

The CSES mission can have a crucial role in the investigation of the acceleration mechanism, the global distribution, and the variability of trapped particles in the Van Allen belts thanks to the multi-instrument payloads on board, which allow simultaneous measuring of the electro-magnetic field, particles and plasma. Indeed, it is well known that the geomagnetic field changes under geomagnetic active conditions, giving rise to a redistribution of radiation-belt particles on both spatial and temporal scales.

The simultaneous and continuous monitoring of particle fluxes, electromagnetic fields, and plasma composition is a requirement to determine how and where waves control the radiation-belt dynamics. Even though the largest changes in the geomagnetic field are due to the ring-current variation during a geomagnetic storm, resonant wave-particle interactions also strongly affect belt electrons. Indeed, the chorus can both accelerate relativistic electrons and make them precipitate, while the plasmaspheric hiss can control the location and dynamics of the "slot" region. In this context, the HEPD payload on board the CSES ensures the highest-quality measurement of charged particles below the inner Van Allen belts at energies intermediate between those

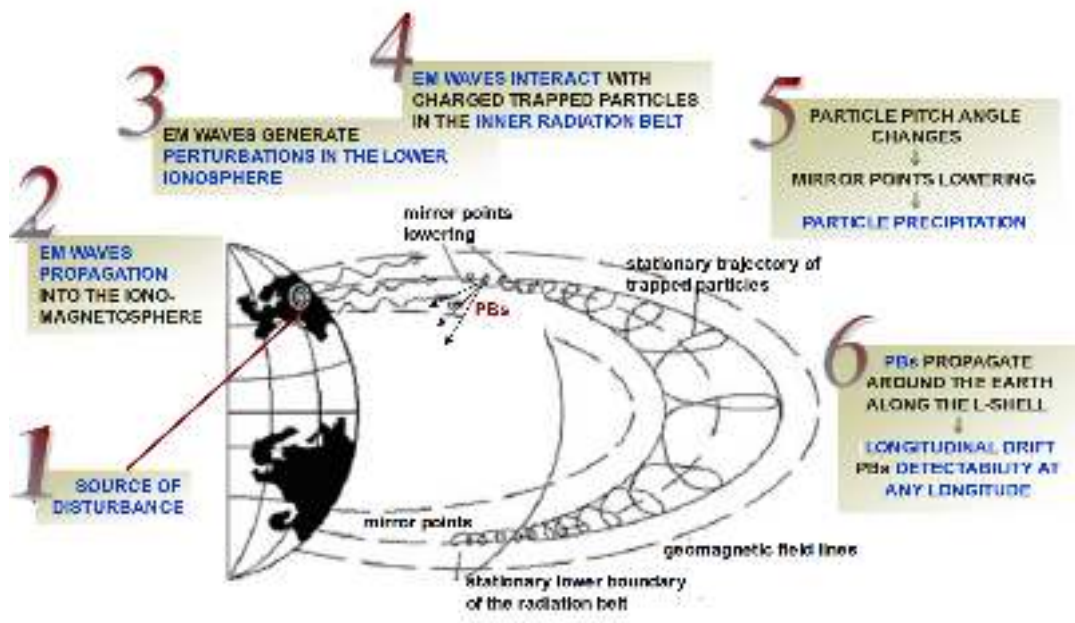


FIGURE 2.2: Schematic representation in a meridian plane of the trajectories of charged particles trapped by the geomagnetic field lines. PBs stands for "particle bursts".

detected by the Radiation Belt Storm Probes. Therefore, CSES data can extend and complement the observations from Van Allen Probes, as well as those performed by PAMELA and AMS-02.

2.2.2 Litosphere-ionosphere-magnetosphere coupling

The litosphere-atmosphere-ionosphere coupling is a complex subject involving many physical effects and interactions that occur from the Earth surface up to the magnetosphere. The investigation of such coupling mechanism, and in particular of the partially unknown behavior of the ionosphere-magnetosphere transition region, is of fundamental importance for Earth remote sensing, monitoring of the near-Earth electromagnetic environment and studying of natural hazards. A great part of these effects is caused by natural non-seismic and anthropogenic electromagnetic emissions, but of particular relevance are the electromagnetic disturbances associated with the seismic activity that can produce ionospheric perturbations as well as the precipitation of particles from the Van Allen belts, observed before, during and after earthquakes of medium and strong magnitude (V. Sgrigna et al., 2005). All of these phenomena must be distinguished from those induced by sources external to geomagnetic activity and by atmospheric events.

Ground-based measurements revealed slow electrostatic and magnetic field variations as well as preseismic ground potentials. The latter are generated as streaming potentials when saline water moving through porous rocks entrains ionic charge, or through stress applied to rocks as quartz. Ground low-frequency (ULF/ELF) electromagnetic emission signals have also been documented in connection with relevant earthquakes and preliminary explanations have been reported on the subject. More observations of local ground-based seismo-electromagnetic emissions have been obtained on a larger (ULF-HF) frequency band. Space observations of atmospheric and ionospheric perturbations over seismic regions have been reported and discussed on the occasion of several strong earthquakes.

The above ground-based measurements, space observations, and related theoretical speculations, together with laboratory experiments suggest different possible scenarios for the generation and propagation mechanisms of the broad-band seismo-electromagnetic perturbations. One of such scenario is to consider these perturbations as due to waves generated by preseismic sources and transmitted into the near-Earth space. Another one is to interpret these disturbances as a secondary effect produced by other mechanisms induced by seismic activity (V. Sgrigna et al., 2005; R. Battiston and V. Vitale, 2013; D. Pisa, M. Parrot and O. Santolik, 2018; M. Piersanti et al., 2017).

A relatively new result is that preseismic electromagnetic disturbances produced in a seismic area with one of the above-described mechanism, are thought to reach the inner Van Allen belt, where they may interact with trapped particles with a bouncing frequency in the same band (e.g., between ULF waves and electrons of energy >1 MeV or protons of energy of the order of some tens of MeV). When the wave frequency matches the particle bouncing frequency, the particle experiences the wave particle field E at every passage over the perturbed zone. This could produce a variation in the particle pitch angle, a lowering of its mirror points, and the possible precipitation of the affected particle. Due to the standard longitudinal drift, the precipitating particles also continue to drift around the Earth along the same unperturbed L-shell where the interaction occurred, thus creating a particle wave that propagates around the Earth, with electrons drifting eastward and protons drifting westward. This wave gets slowly damped due to energy losses in the residual atmosphere and spreads in space due to dispersion of particle angular velocity. Due to the drift of trapped particles around Earth,

any particle burst of seismic origin can be observed not only above the epicenter but also at any longitude where the satellite crosses the disturbed L-shell. Therefore, if the seismic nature of the particle bursts were confirmed and their statistical significance assessed, these three factors would, in principle, allow one to reconstruct the geographic zone of the incipient earthquake (M. E. Aleshina et al., 1992).

Some authors (V. Sgrigna et al., 2002b; Aleksandrin S. Yu et al., 2003) also made attempts to confirm the preseismic character of these particle bursts, by using statistical correlations of the temporal difference between burst and earthquake, and under the hypothesis that preseismic ULF/ELF wave-trapped particle interaction may cause the precipitation of radiation belt electrons and protons. They proposed that in a certain portion of the ionosphere-magnetosphere transition zone such a low frequency content of this radiation (from \sim DC to some hundred Hz) can propagate as Alfvén waves along the geomagnetic field lines. Near the radiation belt boundary, the waves may resonantly interact with trapped particles causing particle precipitation as a result of the pitch angle diffusion (V. Sgrigna et al., 2005).

It is worth remarking that on-the-ground and iono-magnetospheric electromagnetic perturbations possibly induced by seismicity must be carefully distinguished from the large background caused by geomagnetic natural fluctuations and electromagnetic emissions of anthropogenic origin. To this purpose, on the one hand, data collected during geomagnetic perturbed periods (selected by mean of geomagnetic indices such as Kp, Dst, Ap, etc.) cannot be used for statistical analysis. On the other hand, ground-based signals from radio navigation and communication VLF transmitters can interact with trapped particles around the geomagnetic equator, and powerful transmitters for high-frequency broadcasting stations can induce ionospheric heating phenomena due to changes in the local temperature and density of plasma components. Finally, tropospheric electromagnetic emission due to lightning and whistlers can generate characteristic electromagnetic phenomena in the top side of the ionosphere. In these circumstances, the data cannot be used for statistical analysis.

The measurement of high-energy charged particle fluxes has been obtained on board various spacecraft, including the Mir orbital station, METEOR-3 and GAMMA by means of different instruments. Such fluxes have been processed and analyzed in order to search for temporal and spatial correlation between particle bursts and strong earthquakes. In the analyses, sharp short-term increases of particle count rates, from tens of seconds to a few

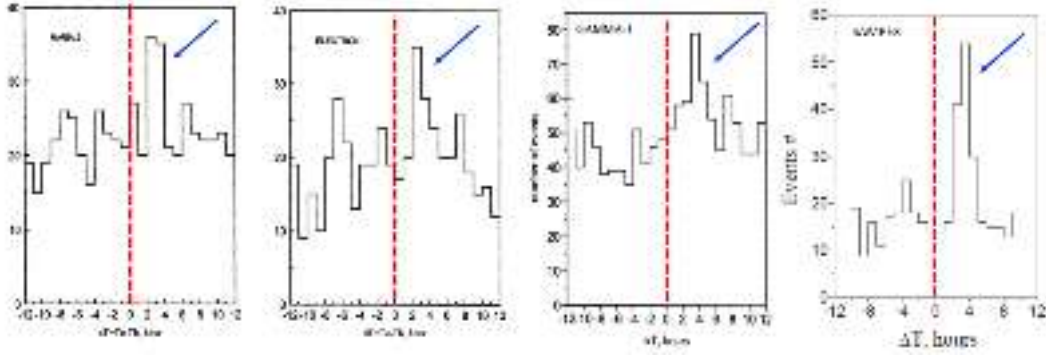


FIGURE 2.3: Histograms of the time difference ΔT between the time of selected earthquakes and that of particle bursts obtained by the MARIA, ELECTRON, GAMMA-1 and SAMPEX space missions. A positive value of the peak suggests that particle bursts precede earthquakes in time. (Aleksandrin et al. (2003))

minutes, were identified as particle bursts if their probability exceeded a given threshold cut with respect to the average value of the background.

In particular, Aleksandrin et al. (2003) performed a multi-instrument data analysis. Fig. 2.3 shows the temporal correlation between particle bursts and a set of earthquakes with magnitude $M > 4$ after selection of satellite positions at an L-shell < 2 and exclusion of the SAA region.

The value of ΔT was defined as

$$\Delta T = T_{EQ} - T_{PB} \quad (2.1)$$

where T_{EQ} and T_{PB} are the times of occurrence of the earthquake and particle burst, respectively. The positive value of all peaks (2-5 hr) means that the particle bursts could play the role of short-term earthquake precursors. In the analysis, sharp short-term increases of particle count rates, from tens of seconds to a few minutes, were selected as particle bursts whenever the count rate exceeded the average value of the background by four standard deviations. Aleksandrin et al. (2003) also investigated the spatial correlation between bursts and earthquakes by monitoring the variation of temporal distributions using

$$\Delta L = L_{EQ} - L_{PB} \quad (2.2)$$

as an additional parameter. Here L_{EQ} is the L-shell of the earthquake (i.e., the L-coordinate of the point at a certain altitude above the epicenter, which coincides with the altitude of the region by which the electromagnetic emission of seismic origin is captured in the geomagnetic field lines) and

L_{PB} is the L-shell of the satellite corresponding to the particle burst. The analysis shows that ΔT distributions present no peaks for $\Delta L > 0.5$; i.e. the L-shell of the earthquake significantly differs from that of the particle bursts, which is a result in support of a correlation between particle precipitation and earthquakes. Moreover, recent studies of low-energy electrons collected by the NOAA POES over 13 yr (R. Battiston and V. Vitale, 2013) found a statistical temporal correlation between the occurrence of pairs of particle bursts and earthquakes of magnitude $M > 5$.

Some CSES payloads has also been designed to investigate correlations between particle bursts and seismic activity. Indeed, the HEPD device has been conceived to detect electrons and protons in the energy range of interest, with wide angular acceptance (about 1 sr over the full energy range) and large geometry factors up to $300 \text{ cm}^2 \text{ sr}$ at the peak, that is, at least 100 times larger than the geometric acceptance of DEMETER and at least 1000 times larger than the one of NOAA POES. The HEPD will also be able to investigate the existence of bursts of protons and light nuclei possibly correlated with major earthquakes.

Although low-frequency seismo-associated electromagnetic emissions have been observed on the ground close to earthquake epicenters and in space by several satellites before strong earthquakes, their pre-seismic nature and postulated role in the lithosphere-ionosphere coupling mechanism is far from experimentally confirmed. Further studies on this topic are needed in order to understand the physical mechanism of the above-mentioned correlations; an earthquake forecast is not possible at the present.

2.2.3 Solar physics

CSES mission is able to monitor the solar impulsive activity and cosmic ray solar modulation, by detecting proton and electron fluxes from hundreds of keV to hundreds of MeV. The measurements will provide an extension up to very low energy of the range of the particle spectra that are monitored, in the past 24th solar cycle, by PAMELA and AMS experiments. During maximum activity, SEPs become more frequent, and a wide variety of data can be accumulated and compared, grouping different events according to some of their features (duration, spectral index, rollover energy, intensity, region of occurrence). Expected to be a 5-years mission, CSES could hopefully register a large number of solar events in a range of energy that lies between the

insitu observations by instruments like ACE, STEREO, GOES (Lario et al., 2013) and the high-energy data from neutron monitors on the ground.

The long period of data-taking permits the collection of information about different categories of solar events, for example, giving an answer to the question of whether GLE (Ground Level Enhancement) and non-GLE events are just a different manifestation of the same mechanism with different energy or two completely separate classes of events.

The study of the relation between the spectral index and rollover energy of a solar event could also shed light on the acceleration process that took place. Indeed, whether the Sun accelerates particles at low altitudes through magnetic reconnection or at higher regions of the corona through CME-driven shocks is still a matter of study, given the complexity of the modifications induced by propagation phenomena across interplanetary space.

Concerning electrons, they are accelerated and released during large, gradual SEP events, reaching energies of tens of MeV. Medium-term transients, such as Forbush decreases which are caused by a CME hitting Earth and shielding galactic particles that come from outside the magnetosphere, is another possible topic of interest. Large CMEs heavily affect the geomagnetic cutoff, shrinking the portion of the magnetosphere that faces the Sun and allowing more particles to precipitate at lower latitudes. The HEPD energy range is well suited to follow the evolution of such decreases, giving information about magnitude of the decrease itself and recovery time of the galactic particles to normal conditions.

CSES mission fits in a period when the issues concerning space weather are being recognized as urgent, thus earning a chance to serve as a space monitor of the vicinity of the Earth and help develop further counteractions against possible dangerous solar phenomena.

2.2.4 Space weather

Enhanced solar wind and solar radiation energy into near-Earth space result, for example, in strong electric currents flowing in the magnetosphere and ionosphere and in significant plasma density structuring or alterations of neutral composition, density and winds in the upper atmosphere (B. T. Tsurutani et al., 1997).

Such periods of enhanced activity (magnetic storms) cause rapid variations of the geomagnetic field up to several hundreds of nT in a few minutes. These strong variations in the strength and direction of the geomagnetic field

can disturb navigation activities that are based on precise magnetic maps or satellite-based navigation, i.e. GPS or GNSS; such irregularities result in navigational errors that are not included in ionospheric correction models implemented in commercial GPS receivers and may lead to signal outage and radio wave scintillations (S. Basu et al., 2002).

Observations from the CSES mission have large value for near-Earth space research; the satellite carries simultaneous measurements of the magnetic, electric, plasma and neutral environment in near-Earth space.

2.3 The satellite

The CSES mission is a 3-axis attitude stabilized satellite, based on the Chinese CAST2000 platform of the DFH Satellite Co. Ltd. (Beijing, China). CAST2000 offers a standard multi-mission platform. Technically, the platform architecture is generic, and adaptations are limited to relatively minor changes in several electrical interfaces and software modules.

In the case of CSES, the platform includes the data transmission subsystem, the structure and mechanism subsystem, a thermal control subsystem, Attitude and Orbital Control subsystem (AOC), the power supply subsystem, telemetry and tele-command subsystems, the On-Board Data Handling subsystem (OBDH) and the scientific payloads.

For the satellite structure construction the dual-layer cabin design was used, consisting in the payload layer cabin and the platform layer cabin. In orbit, satellite flies in the direction of X axis (see Fig. 2.4) and Z axis is pointing nadir. A solar panel is located on the +Y side of satellite with an offset angle of 12° and could rotate around satellite Y axis.

Housekeeping data exchange onboard CSES uses CAN (Controller Area Network) bus, OBDH center computer is used as a host and all equipment are guests. Onboard telemetry use the telemetry package to communicate. Satellite AOC subsystem uses an earth oriented 3-axis stabilization. Three star trackers, two groups of gyros and one digital sun sensor are used to measure the attitude. Reaction wheel and magnetic torque are used to maintain the zero-momentum control. A propulsion system is used for attitude complementary control and orbit maintenance. A S-band telecommunication system assisted by GPS positioning is used for telemetry-telecommand subsystem. Power supply subsystem is composed of 80Ah Li-ion battery and a GaInP2/GaAs/Ge solar cell panel.



FIGURE 2.4: Several views of the CSES layout with the 4 telescopic booms of the EFD probes stowed. The search-coil magnetometer boom is folded at the edge between the XZ and the XY planes.

Scientific data are transmitted in X-band at 120 Mbps. The satellite has an orbit period of 97 minutes and a revisiting period of 5 days (X. Shen et al., 2011; X. Shen et al., 2018).

The scientific payloads include a search-coil magnetometer, an electric field detector, a high precision magnetometer, a Global Navigation Satellite System (GNSS) occultation receiver, a plasma analyzer, a Langmuir probe, an energetic particle detector and a three-frequency transmitter. To assure the accuracy of science data for all the payloads and avoid electromagnetic interferences and plasma contamination, the solar panel rotation and AOC adjustments (magnetic torque, reaction wheel) are suspended while payloads are working (Ambrosi G. et al., 2018; Cao J. B. et al., 2018).

There are two different orbital working zones: the payload operating zone, and the platform adjustment zone. The payload instruments collect measurements in the geographic latitude range of $\pm 65^\circ$. At higher latitudes (in the platform adjustment regions), all detectors are planned to be switched off, in order to perform the activities of the satellite attitude and orbit control system. In payload operation regions, some instruments collect data in two

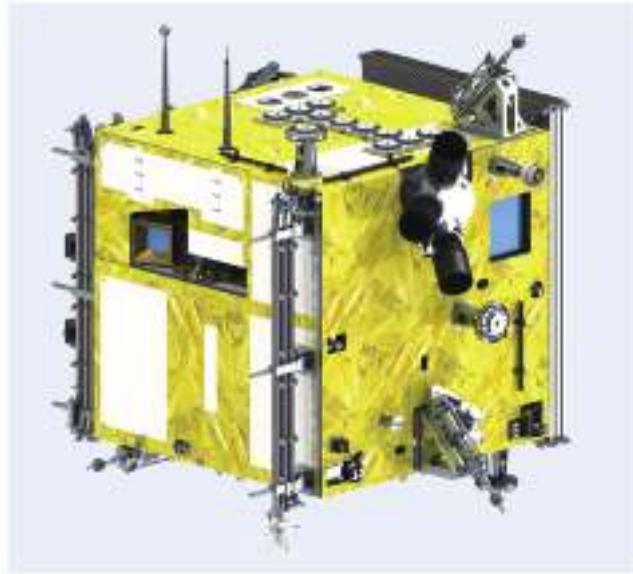


FIGURE 2.5: Rendering of the CSES satellite.

operating modes: "burst mode" and "survey mode". The burst mode is usually activated when the satellite passes over the whole China territory and the regions with a strong seismic activity; the survey mode is planned for the other areas of Earth. Payloads with two operation modes work in burst mode for 2 h and in survey mode for 15.6 h in a day while the working time of payloads with single mode is 17.6 h in a day.

The ground segment of CSES consists of science and application center, satellite ground networks, field verification bases and comparison system for satellite-ground measurement. The science and application center, which is in charge of mission operation and control, data management and service, as well as earthquake science application, is situated at the China Earthquake Administration.

The tasks of ground segment are: to receive and process data from CSES receiving stations; to make observational schedules; to execute and control data application system operations; to store and manage data; to verify and evaluate data; to provide a data sharing service.

The data products of CSES are classified into raw data, scientific data and seismic event data. The data collected on ground are as follows: multi-band waveform and spectrum of electromagnetic field; in-situ plasma parameters including electron and ion density and temperature; electron density profiles and tomography; energetic particle flux and energy spectra; seismic event data; geomagnetic field and ionosphere models and other related scientific research products.

There are totally 5 levels of data, which are described as follows:

- Level-0: the raw data of payloads generated after a series of process including frame synchronization, de-randomization, decoding and de-formatting. All redundant data are removed in this level;
- Level-1: the data obtained after general error rejection, format conversion and calibration of Level-0 data;
- Level-2: Physical quantity data with satellite orbit information after coordination system transformation and necessary data inversion of Level-1 data;
- Level-3: Time sequential data in frame of satellite orbits generated after resampling, necessary spectral analysis based on Level-2 data;
- Level-4: Global or regional dynamic observation data retrieved from Level-2 and Level-3 data, in terms of variation between recursive orbits and disturbance observed according to background field.

2.4 The payloads

The payloads onboard CSES consist in a Search-Coil Magnetometer (SCM) and a High Precision Magnetometer (HPM) to measure respectively the components and the total intensity of the magnetic field; an Electric Field Detector (EFD) to measure the electric field; a plasma analyzer and a Langmuir probe to measure the disturbance of plasma in ionosphere; a GNSS occultation receiver and a tri-band beacon to measure the electron density; a High Energy Particle Package (HEPP) and a High Energy Particle Detector (HEPD) to measure the particles flux and their energy spectrum.

The SCM (Fig. 2.6) measures magnetic field component fluctuations in ionosphere. It has a band between 10 Hz and 20 kHz and can detect magnitude from $5 \cdot 10^{-4}$ to 50 nT with a sensitivity of $1 \text{ nT} / \sqrt{\text{Hz}}$ at 2 kHz.

The HPM includes a dual sensor FluxGate Magnetometer (FGM), developed by the National Space Science Center of the Chinese Academy of Sciences, for measurements of the vector components of the magnetic field, and a scalar magnetometer (Coupled Dark State Magnetometer, CDSM), developed by the Space Research Institute of Experimental Physics of the Austrian Graz University of Technology, for high accuracy measurement of the magnetic field intensity. A scalar magnetometer is required in order to regularly



FIGURE 2.6: The search coil magnetometer.

recalibrate in flight measurements executed by the FGM, that are typically affected by offset and gain uncertainties due to the intensity of the geomagnetic field in low Earth orbit satellite missions. The CDSM is an optically pumped absolute scalar magnetometer, which is based on two-photon spectroscopy of free alkali atoms. In a special laser-based excitation mode, three different magnetic field dependent resonances arise in the presence of an external magnetic field. They reach their maximal strengths at different angles between the magnetic field direction and the reference axis of the sensor, which is defined by the optical path of the laser excitation field. Depending on this angle, the strongest resonance is selected for the actual measurement, which enables an omni-directional scalar magnetometer. The FGM has a DC frequency of 15 Hz, a linearity better than 0.005%, a range reaching 70000 nT, a noise lower than 0.025 nT and a stability better than 0.25 nT in 15 h; the CDSM has a linearity better than 0.004%, a range reaching 100 μ T and a noise better than 0.05 nT/ $\sqrt{\text{Hz}}$ at 1 Hz.

The EFD (Fig. 2.7) measures the variation of the ionosphere electric field due to perturbations from solar, seismic and anthropic phenomena. It consists of four independent identical sensors installed at the tips of four booms (about four meters long) and it has been designed in collaboration between the Lanzhou Institute of Physics and the INFN division of Roma Tor Vergata. Two different engineering models have been designed and tested in Faraday cage at the INFN division of Roma Tor Vergata, and in a plasma chamber at the IAPS-INAF institute in Roma Tor Vergata. The EFD flight model, assembled by the Lanzhou Institute of Physics, has been optimized taking into



FIGURE 2.7: The four independent sensors composing EFD.

account the performance of the two instruments. The EFD has a DC band of 3.5 MHz, resolution of $1\mu\text{V}/\text{m}$ in DC-16 Hz and sensitivity of $0.05\mu\text{V}\text{m}^{-1}\sqrt{\text{Hz}}$ in the range 10-20 kHz.

The plasma analyzer measures the plasma parameters, including ion density, ion temperature, ion drift velocity, ion composition and ion density fluctuation, for searching the coupling between ionosphere and seismic activity and the ionospheric physics. Its main performances are ion density range from $5\cdot 10^2$ to $1\cdot 10^7\text{ cm}^3$, ion temperature between 5000 and 10000 K with accuracy of 10%, ion drift velocity between -3 and 3 km/s, sensitivity of ion density fluctuation of about 10^{-2} .

The Langmuir probe (Fig. 2.8), realized by the Center for Space Science and Applied Research of the Chinese Academy of Science, allows to monitor the global parameters of the ionosphere in situ and to study the coupling between lithosphere and ionosphere before, during and after earthquakes. It consists of a pair of spherical Langmuir probes with diameters respectively of 5 cm and 1 cm, installed at the tip of booms 50 cm long. The Langmuir probe has been tested in an electronics test facility for calibration and in the INAF-IAPS plasma chamber.

The GNSS occultation receiver is used for ionosphere vertical sounding. In particular, it allows to measure the total electron content and to obtain vertical electron density. It has a sample rate in the range 20-100 Hz with system tomography accuracy of 10%.

The Tri-Band Beacon is a three-frequency radio beacon developed to provide transmission at VHF/UHF and L-band (150/400/1067 MHz). The primary objective of the Tri-Band Beacon is to study the electron density in the



FIGURE 2.8: The two spherical Langmuir probes.

ionosphere and to produce two-dimensional maps or one-dimensional profiles. The secondary objective is to measure the influence of ionospheric irregularities on VHF, UHF and L-band transmissions from space to ground.

The HEPP (Fig. 2.9), realized by the Institute of High Energy Physics of the Chinese Academy of Science, consists of a high-energy detector (HEPP-H), a low-energy detector (HEPP-L) and a solar X-ray monitor (HEPP-X). HEPP technical specifications are reported in Fig. 2.1. There is an overlap in the energy ranges of the two detectors, which can be used to calibrate each other. At the same time, the incident directions of particles can be detected, yielding information of pitch angle distribution. HEPP-H and HEPP-L are mainly used to study processes related to abnormalities in spatial distributions, scattering of pitch angles and acceleration of energetic charged particles caused by electromagnetic waves, magnetic storms, solar flares, CMEs and other solar activities. HEPP-X is an auxiliary payload which can effectively monitor solar X-ray flare activities. The observations of HEPP-X combined with those of other solar detection satellites can provide reference data for eliminating the influence of solar activity on space particle detections (X. Q. Li et al., 2018).

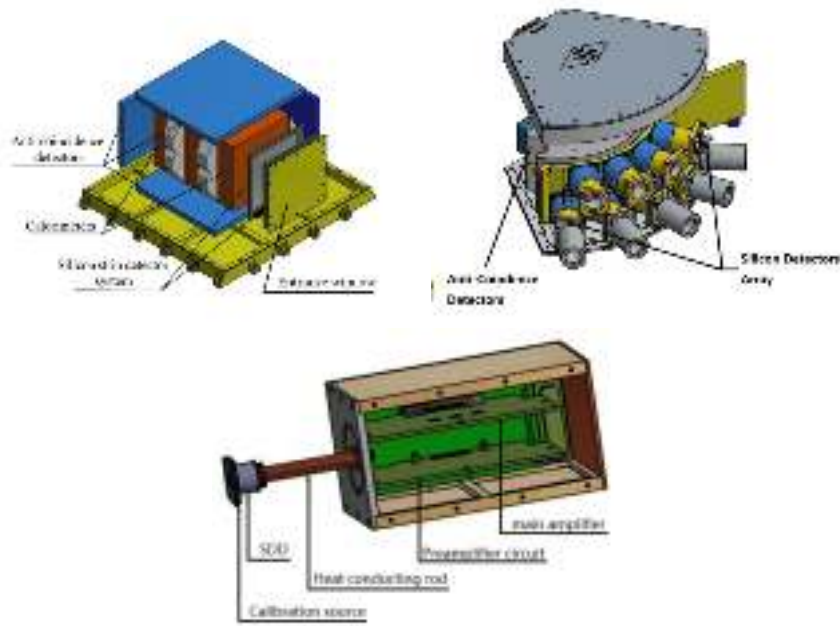


FIGURE 2.9: Structural diagram of the three detectors composing HEPP: HEPP-H (on the left), HEPP-L (at the center) and HEPP-X (on the right).

Item	Particle	HEPP-H	HEPP-L	HEPP-X
En. range	Electron	1.5-50 MeV	0.1-3 MeV	-
	Proton	15-200 MeV	2-20 MeV	-
	X-ray	-	-	0.9-35 keV
Ang. resolution	Electron	3.2° 20 MeV	5°	-
	Proton	2.94° 20 MeV	5°	-
En. resolution	Electron	$\leq 8.3\% \geq 10$ MeV	$\leq 8.9\%$ 1 MeV	-
	Proton	$\leq 10\%$ 15-200 MeV	$\leq 7\%$ 2-20 MeV	-
	X-ray	-	-	175 eV 5.9 keV
Id. efficiency	Electron	>98.9%	>96.68%	-
	Proton	>99.9%	>92.98%	-

TABLE 2.1: The main performance parameters of HEPP.

The HEPD, developed by the Italian Collaboration, detects electrons, protons and light nuclei. The main objective is to measure the increase of the electron and proton fluxes due to short-time perturbations of the radiation belts caused by solar, terrestrial and anthropic phenomena. The instrument consists of several sub-detectors; the power supply and electronics are inserted in a box placed at one side of the detector. An extensive description of the HEPD will be given in the following chapter.

Chapter 3

The High Energy Particle Detector

The High Energy Particle Detector (HEPD) is a particle detector installed on CSES to identify the particle type, measure the direction of the incoming particle and detect its energy. The high-inclination orbit allows the instrument to detect particles of different nature during its revolution: galactic cosmic rays, SEPs, particles trapped in the Earth magnetosphere.

HEPD was designed to provide good angular and energy resolution for electrons in the energy range 3-100 MeV, protons in the energy range 30-200 MeV and light nuclei. With a mass of about 45 kg and a power consumption of about 30 W (depending on HEPD status), the allowed operative temperature is between -10° and 45° . All the sensitive sub-detectors are housed in an aluminium box with dimensions roughly $20 \times 20 \times 40 \text{ cm}^3$. HEPD is positioned on the satellite in order to always point at Zenith.

The scientific goals of the HEPD experiment are fully shared with the mission objectives, which have been listed in 2nd chapter of this work. In particular, the relevant scientific objectives, for which HEPD experiment was specially designed, are summarized in the following: 1. to investigate energy spectrum and composition of CR, with particular reference to particles trapped in the Van Allen belts; 2. to study space weather phenomena, such as strong electric currents flowing in the magnetosphere and ionosphere; 3. to search for spatial and temporal stability of the inner Van Allen belts, investigating possible precipitation of trapped particles induced by electromagnetic emissions, as well as by seismo-electromagnetic disturbances (Aleksandrin S. Yu et al., 2003; P. Picozza et al., 2019).

The chapter describes the instrument sub-detectors in dimensions, purposes and materials; two sections follows, respectively about in-flight operation modes and beam tests conducted on ground.

3.1 Detector instruments

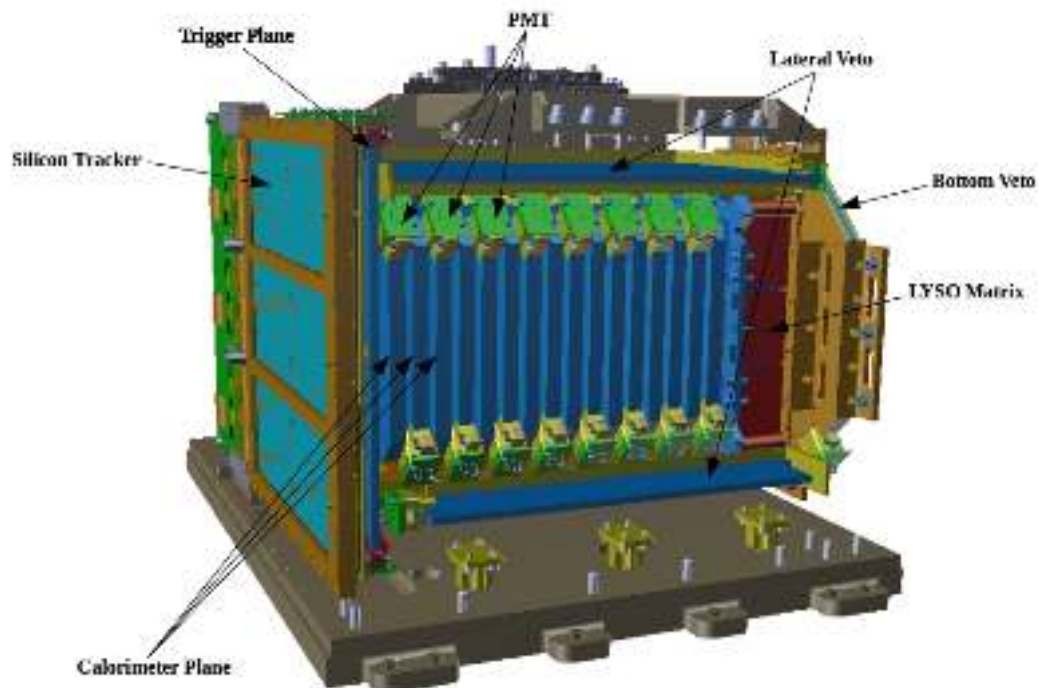


FIGURE 3.1: HEPD structural design. One lateral veto plane was removed to show the internal calorimeter structure.

The HEPD instrument consists of several sub-detectors, listed as follows:

- two planes of double-sided silicon microstrip detectors to provide the direction of the incident particle;
- one thin layer of a plastic scintillator segmented in 6 counters for the event trigger ($15 \times 15 \times 0.5 \text{ cm}^3$);
- a calorimeter composed by a tower of 16 layers of a plastic scintillating material ($15 \times 15 \times 1 \text{ cm}^3$) and a 3×3 matrix of LYSO crystals (an inorganic scintillator, for a resulting plane of dimension $15 \times 15 \times 4 \text{ cm}^3$);
- 5 mm thick planes of plastic scintillator as veto, that surround the calorimeter.

The detector design is shown in fig 3.1.

The HEPD detector is contained in an aluminium box with dimensions $40.4 \times 53 \times 38.2 \text{ cm}^3$. The walls and base-plate are made of milled aluminium panels, with the outside surface covered by a black anodized coating in order to assure good thermal insulation. The detector, together with the power

supply and electronic boxes, is bolted to the satellite cabin space, which provides the contact surface for heat dissipation.

The HEPD comprises the following subsystems:

- detector subsystem;
- electronics subsystem;
- power supply subsystem;
- mechanics subsystem;

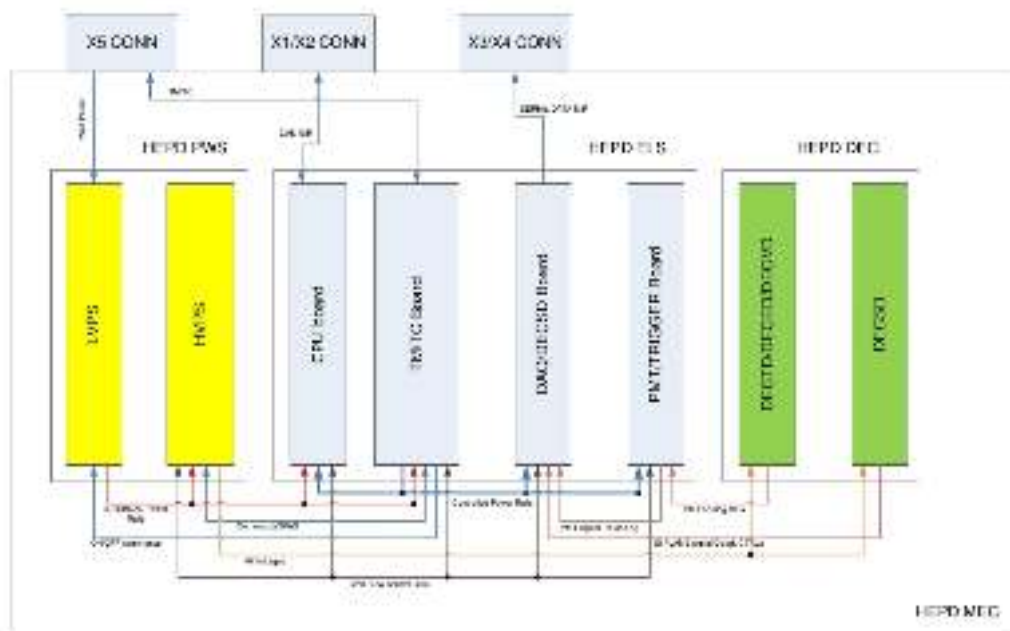


FIGURE 3.2: HEPD connections. The abbreviations stand for: mechanics (MEC), power supply (PWS), electronic (ELS) and detector (DEC) subsystems; low voltage (LVPS) and high voltage (HVPS) power supplies.

The detector subsystem consists of the silicon tracker, the trigger detector, the energy detector (made by plastic and inorganic scintillators), and the veto detector. The electronics subsystem is composed by all front-end electronics and four boards (fig. 3.2):

- DAQ board;
- PMT/Trigger board (or EASIROC board);
- CPU board;

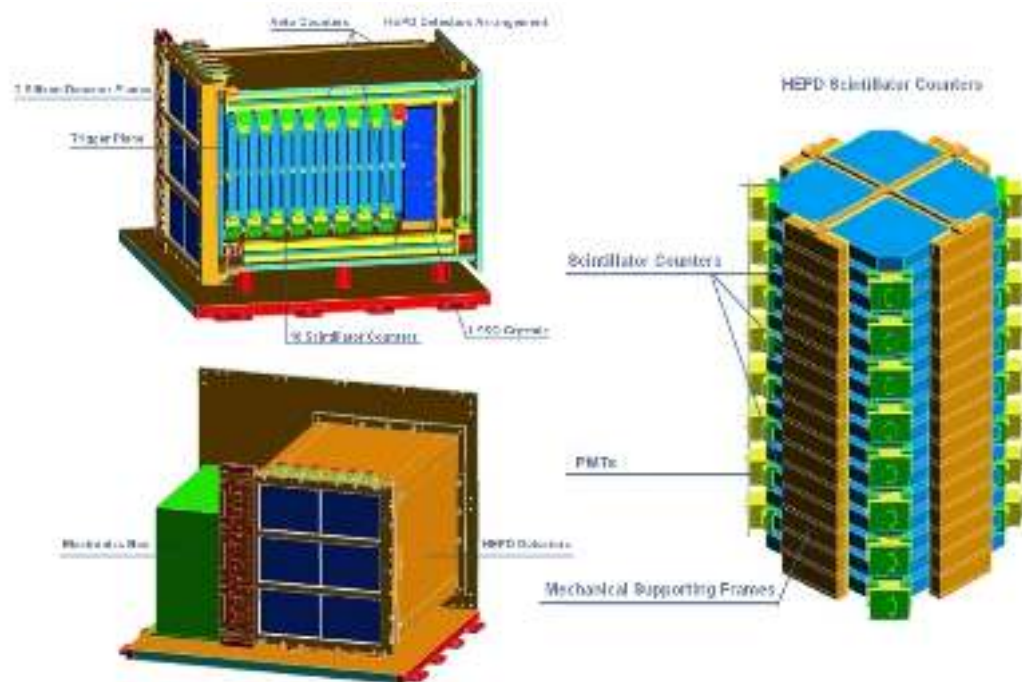


FIGURE 3.3: Lateral (top left) and back (bottom left) view of HEPD detectors and lateral view (right) of the scintillator counters stacked one on top of the other.

- power control board (or TM/TC board).

The power supply subsystem is composed by low voltage and high voltage power supplies, each of them providing power to different parts of the detector.

The mechanics subsystem comprises all mechanical and structural supports required for the good stability of the detector during launch and flight operations.

3.1.1 The detectors

The HEPD detector structure consists of the silicon detector, the trigger detector, the energy detector (made by plastic and inorganic scintillators), and the veto detector. In the description that follows, all dimensions are reported excluding mechanics supports (P. Picozza et al., 2019).

Silicon detector

The tracking system consists of 2 planes of double-sided microstrip detectors ($\simeq 213 \times 215 \text{ mm}^2$) at distance of 10 mm. The signal is collected on both sides of the silicon wafer, with the implanted strips of one side orthogonal to those of the other, in order to provide a measurement of the X- and Y-coordinates of the incident ionizing particle.

Each plane consists of 3 identical independent sections, called ladders, each one composed by 2 silicon modules ($\simeq 71.6 \times 106.6 \times 0.3 \text{ mm}^2$ of active area).

The p^+ side contains 767 implantation strips with a $182 \mu\text{m}$ pitch. The ohmic side contains 1151 n^+ implant strips, alternated with p^+ blocking strips to minimize the effect of the surface charge present on the ohmic side.

Modules are wire-bonded to each other on p^+ strips, each of them read out with a dedicated channel. To save readout channels, n^+ strips are grouped in three for readout, with a degeneracy solved exploiting the information from the trigger plane. The readout strips are directly connected with the readout electronics by means of AC pads.

Each module is read out by $6 + 6 \text{ VA}(y,x)$. The total number of VA is $72(36 \times 2)$ and the total number of readout channels is $\simeq 72 \times 64 = 4608$.

Trigger detector

The trigger detector consists of one thin plane of plastic scintillating material of dimensions $200 \times 180 \times 5 \text{ mm}^3$, segmented in 6 paddles (dimensions $200 \times 30 \times 5 \text{ mm}^3$); each counter is covered by a reflective coating and read out by 2 PMTs, one on each side. The total number of channels for the trigger detector is 12. The HEPD trigger is provided by the signal of the segmented trigger

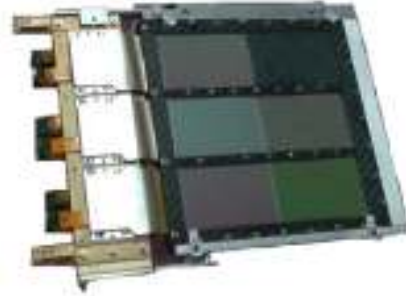


FIGURE 3.4: A HEPD silicon plane during integration. The 3 ladders are visible.



FIGURE 3.5: The scintillator trigger plane during integration. The plane is segmented in 6 paddles.

layer, eventually combined in AND

logic with the signal of other calorimeter components; for example, after the first months of flight, the condition requested for the trigger generation is the AND composition of the signal of one of the paddles, of the 1st plane and of the 2nd plane.

The plane is located below the tracker system and performs a fast trigger-signal generation to start and synchronize data acquisition for the whole apparatus; moreover, it offers the resolution of the ambiguity of the 2nd-coordinate position of the tracking system and the possible rejection of events characterized by more than one paddle hit (multiparticle events).

Calorimeter



FIGURE 3.6: The tower of 16 planes during integration. The LYSO matrix, on the bottom of the instrument, is not visible.

The energy detector is a calorimeter consisting of 16 planes of plastic scintillator and of a 3×3 matrix of inorganic scintillator blocks, the cerium-doped lutetium yttrium orthosilicate (LYSO) on the bottom of the tower. This is a high-density material ($d = 7.1 \text{ g/cm}^3$) that, combined with its 4 cm thickness, allows to increase the operational energy range of the energy detector; these crystals offer the advantage of a high light output, quick decay time and excellent energy resolution. The peak of the emission spectrum is at 428 nm; this makes possible the use of the same PMT type adopted for the plastic scintillator planes as readout devices (for more information about

the scintillating materials, see the dedicated section further in the chapter).

Each plastic scintillator plane is covered by a reflective coating and measures $150 \times 150 \times 10 \text{ mm}^3$. It is read out by 2 PMTs, located at opposite corners. The four corners of every scintillator plane in the calorimeter have been cut in order to create room to place the PMTs. The external walls of the planes, with the exception of the entrance window of the PMT, are optically insulated by means of a thick mylar foil with about a 98% reflectivity index. This

foil reflects back the fraction of scintillation light that escapes the plane, thus increasing energy resolution.

The LYSO scintillator plane measures $150 \times 150 \times 40 \text{ mm}^3$; each block, of dimensions $48 \times 48 \times 40 \text{ mm}^3$ is covered by a reflective coating and read out by 1 PMT located on the bottom face.

The total number of channels is 41 (32 from the plastic scintillator planes and 9 from the LYSO blocks).

The mechanical stability of the system is assured by a support structure that holds the detector in place and prevents any damage during the launch phase. The scintillator counters are arranged in a vertical stack and positioned by means of a carbon-fiber frame, each one mounted on top of another, in such a way as to form a rigid tower where each counter is separated by the adjacent ones. Layers of relatively soft-cell poron, placed between the counters and the carbon fiber, prevent any stress and shock possibly transferred to the counters themselves, so as to avoid damage. The high rigidity of the system provides a great safety margin against stresses and vibration shocks.



FIGURE 3.7: The matrix of 3×3 LYSO blocks during integration.

Veto detector

The veto detector consists of 5 plastic scintillator planes (4 lateral and 1 at the bottom of the instrument), each one covered by reflective coating and read out by 2 PMTs located at about opposite corners. The total number of channels is 10. Detailed dimensions for the counters are in the following:

- lateral 1st view counter: dimensions $200 \times 5 \times 322 \text{ mm}^3$;
- lateral 2nd view counter: dimensions $5 \times 170 \times 322 \text{ mm}^3$;
- bottom counter: dimensions $150 \times 150 \times 5 \text{ mm}^3$.

A poron thickness placed all around the scintillators prevents any stress and shock possibly transferred to the counters.

Properties	EJ-200
Light output	64 % anthracene
Efficiency	10 photons/1 MeV e ⁻
λ of maximum emission	425 nm
Light attenuation length	380 cm
Rise time	0.9 ns
Decay time	2.1 ns
Density	1.023 g cm ⁻³
Temperature range	-20 ÷ 60°C

TABLE 3.1: Some properties of the EJ-200 plastic scintillator.

The system is designed for: identification and rejection of particles that do not cross the two tracking planes but generate a trigger signal; the rejection of secondary particles produced inside the calorimeter and of upgoing particles; the identification of not fully contained events.

In the following some details about the plastic and the inorganic scintillating materials used for the HEPD calorimeter are given.

Plastic scintillator The scintillating material selected for all of the plastic planes (trigger, calorimeter and veto systems) is the EJ-200 by Eljen Technology, which presents a long optical attenuation length and a fast timing as well.

It consists of an organic polymer (poly-vinyltoluene, refractive index 1.58), which is luminescent when irradiated by ionizing particles. Some properties of the EJ-200 are reported in table 3.1, while fig. 3.8 shows its emission spectrum, reported in the Eljen datasheet of the material.

The four corners of every scintillator plane in the calorimeter have been cut in order to create room to place the PMTs. The external walls of the planes, with the exception of the entrance window of the PMT, are optically insulated by means of a thick mylar foil with about a 98% reflectivity index. This foil reflects back the fraction of scintillation light that escapes the plane, thus increasing energy resolution.

Inorganic scintillator The inorganic scintillator used for the cubes matrix at the bottom of the instrument consists in a Cerium-doped Lutetium based scintillation crystal, that offers several benefits such as high density (7.1 g/cm³), fast exponential decay time and is non-hygroscopic.

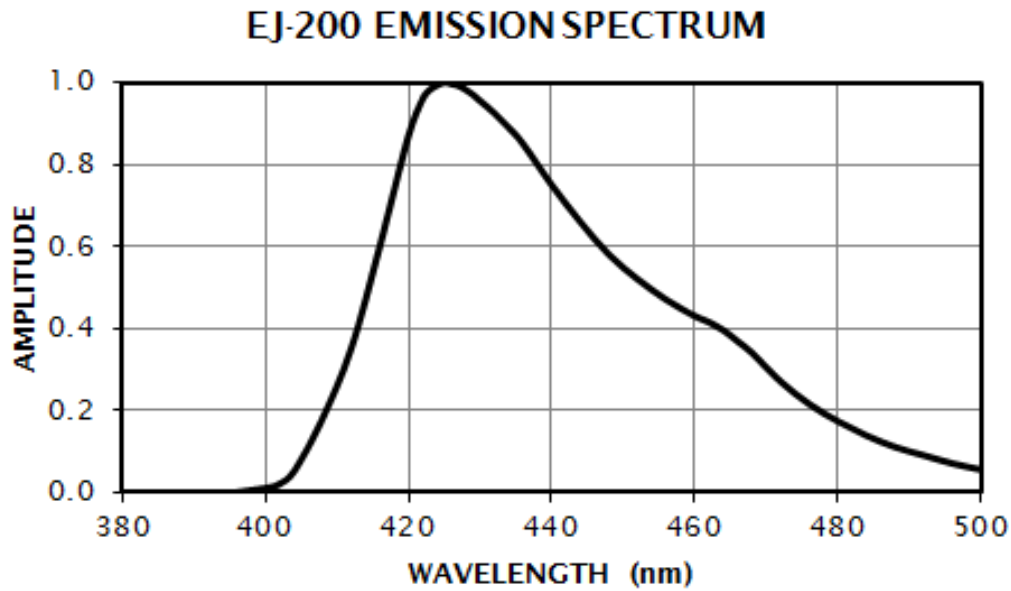


FIGURE 3.8: Emission spectrum of the EJ-200 plastic scintillator.

Properties	LYSO
Density	7.1 g/cm ³
Attenuation length for 511 keV	1.2 cm
Energy resolution	8% 662 keV
Wavelength of emission max	420 nm
Refractive index emission max	1.81
Decay time	36 ns
Light yield	32000 photons/MeV
Average temperature coefficient from 25 to 50°C	-0.28%/ 1°C

TABLE 3.2: Some properties of the LYSO Saint-Gobain scintillator.

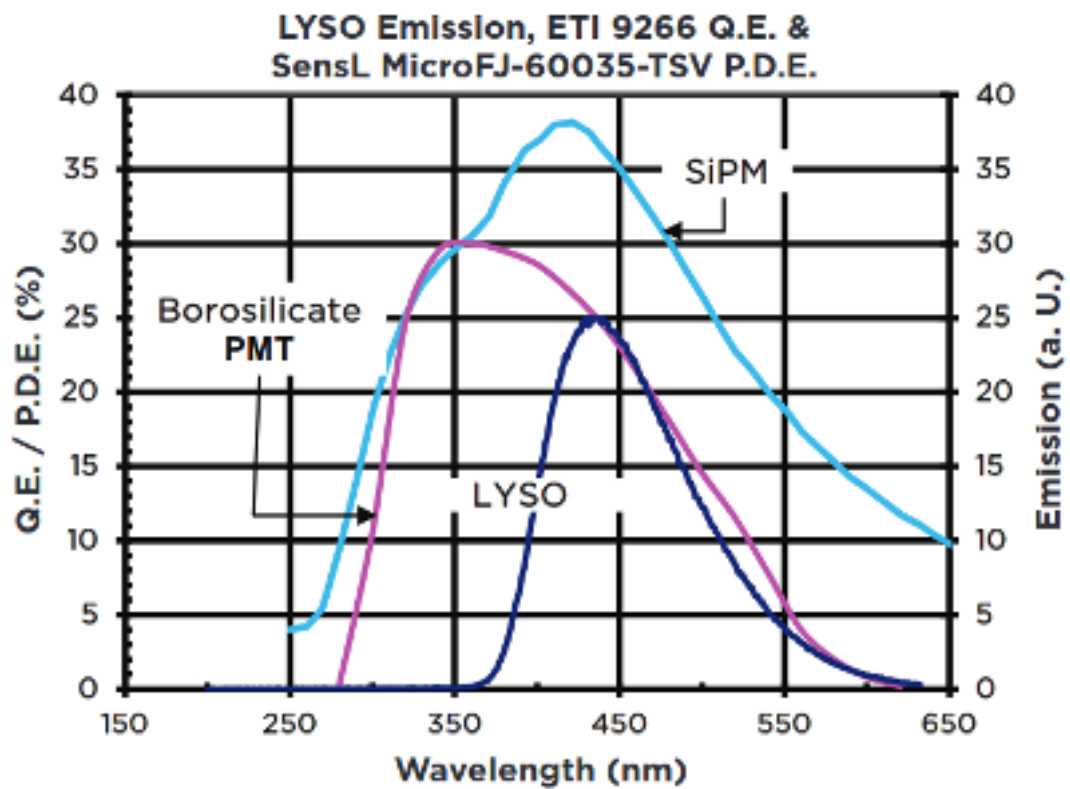


FIGURE 3.9: Emission spectrum of the LYSO scintillator (blue), compared with the q.e. of a SiPM (cyan) and of a Borosilicate PMT (violet).

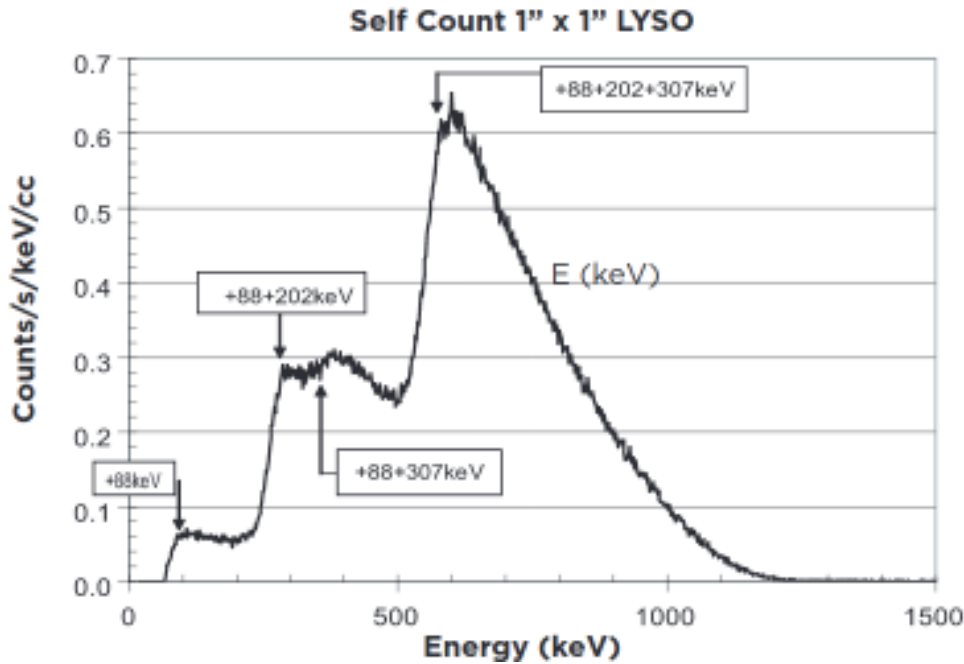


FIGURE 3.10: Absorption spectrum of a ^{176}Lu radioactive event in a $1'' \times 1''$ LYSO cube. The distribution is practically null at 1.2 MeV.

It consists of an inorganic chemical compound with chemical formula $\text{Lu}_{2(1-x)}\text{Y}_{2x}\text{SiO}_5$. Some properties of the Saint-Gobain engineered version, selected for the HEPD, are reported in table 3.2, while fig. 3.9 shows the emission spectrum, compared with the quantum efficiency of the most common Photo Multiplier Tubes.

LYSO is a Lutetium-based scintillator which contains a naturally occurring radioactive isotope, ^{176}Lu , a β emitter. The decay results in a 3 gamma ray cascade of 307, 202 and 88 keV, where self-absorption of these photons results in the spectra in fig. 3.10 in a $1'' \times 1''$ cube. Total rate for this activity is 39 cps/g. Monte Carlo simulations have verified that intrinsic radioactivity is not an issue either for the energy reconstruction of the event or for eventual fake triggers, within a probability of 0.1‰.

The external walls of the cubes, with the exception of the entrance window of the PMT, are optically insulated by means of the same mylar foil used for plastic scintillators (98% reflectivity index).

Photo Multiplier Tubes

The PMT model chosen to read out all scintillator counters is the R9880-210, manufactured by Hamamatsu. As can be seen in fig. 3.11, the quantum efficiency spectrum (i.e., the ratio between the number of output electrons and

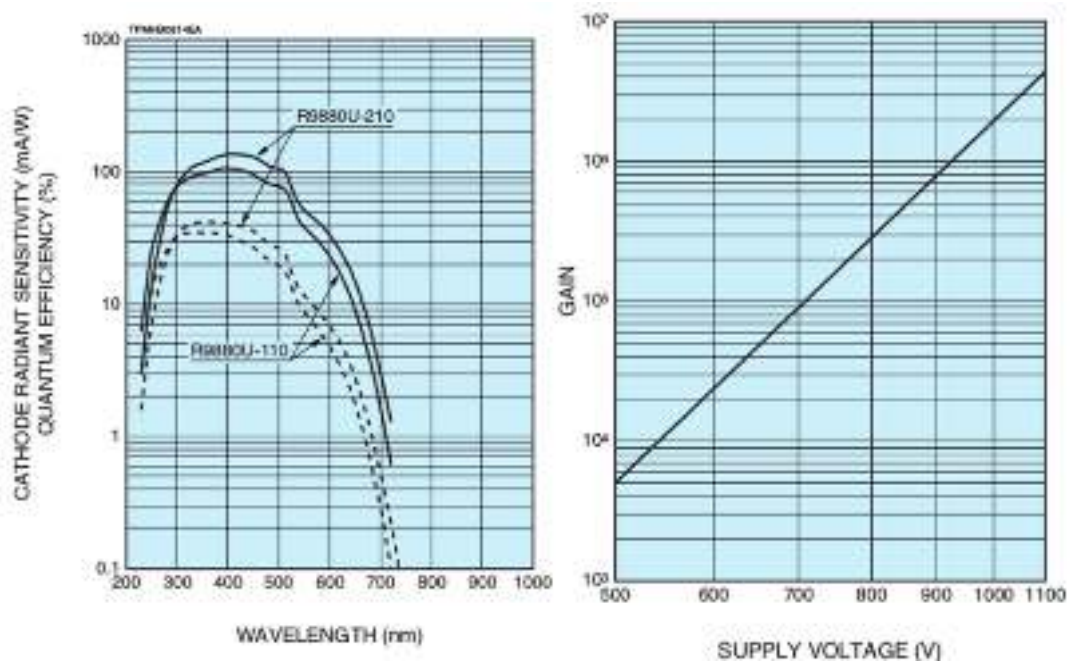


FIGURE 3.11: (Left) Quantum efficiency and (right) gain from Hamamatsu PMT datasheet.

incident photons) matches the light emission band characteristic of the scintillator EJ-200 with a peak at 425 nm. Furthermore, the R9880-210 is a small device (cylindrical shape and a 8 mm diameter of effective area for the entrance window) with a small weight and an operating temperature in the range $[-80^{\circ}\text{C}; 50^{\circ}\text{C}]$, all important parameters to be taken into account for a spaceborne apparatus.

Considering the supply voltage (between 750 and 900 V) provided by the HEPD power supply system, the gain obtained by the R9880-210 is of the order of 10^5 - 10^6 . The interface between any PMT and scintillator is obtained through a soft optical pad.

Each PMT is characterized by its own pedestal, the electronic noise peak, which corresponds to the ADC signal registered when zero photoelectrons are acquired.

3.1.2 The power supply

The power supply system provides the low voltages (main power supply unit - LVPS) to the detector electronics and the high bias voltages for the PMTs and silicon modules (secondary power supply unit - HVPS). A schematic diagram of voltages distribution is shown in fig. 3.12.

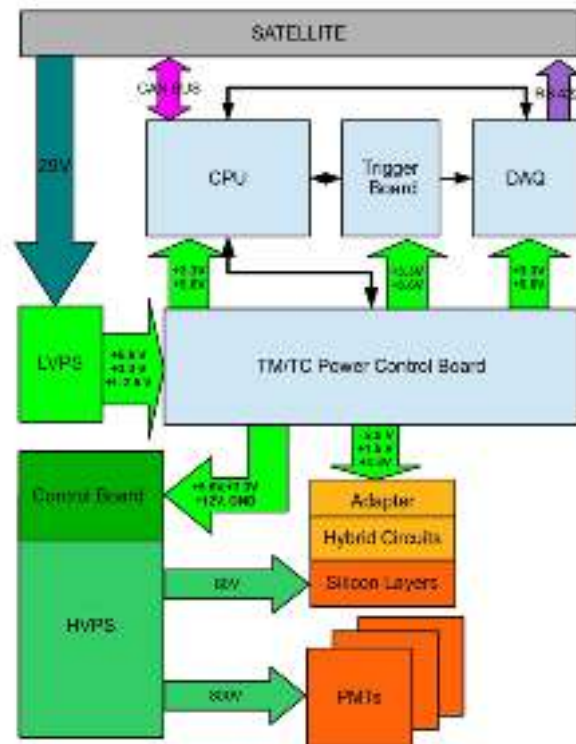


FIGURE 3.12: Electronics block diagram: LV and HV bias.

The LVPS houses 2 identical and independent switching-type DC/DC converters on a single PCB; each DC/DC converter provides 29.5 to 3.6 V 4A, 29.5 to 5.6 V 2A and 29.5 to ± 2.5 V 1A isolated output voltages, when receiving a 26.5 V - 32.5 V input voltage.

A number of signals allows the board's control. The output current is Pulse-By-Pulse controlled, in order to protect the circuit from overload and short circuit. The board is provided with protection devices which keep the operating parameters within safety limit.

The HVPS is composed by the following subsystems: metallic enclosure; step-up modules (type A and type B); HV protection board and HVPS control board. The design of step-up modules allows them to be used to generate the HV needed by the PMTs (type "A" - V_{OUT} up to 1200 V) and by the silicon planes (type "B" - V_{OUT} up to 150.8 V).

Each board is duplicated (named HOT and COLD side) in order to take advantage of redundancy. 20 HV modules of type A (10 HOT and 10 COLD) provide the bias voltage to the detector PMTs, 4 HV modules of type B (2 HOT and 2 COLD) provide the bias voltage to the silicon detector planes (one for each silicon plane). The high voltage input values can be set and

monitored through the high-voltage power supply control board.

3.1.3 The electronics

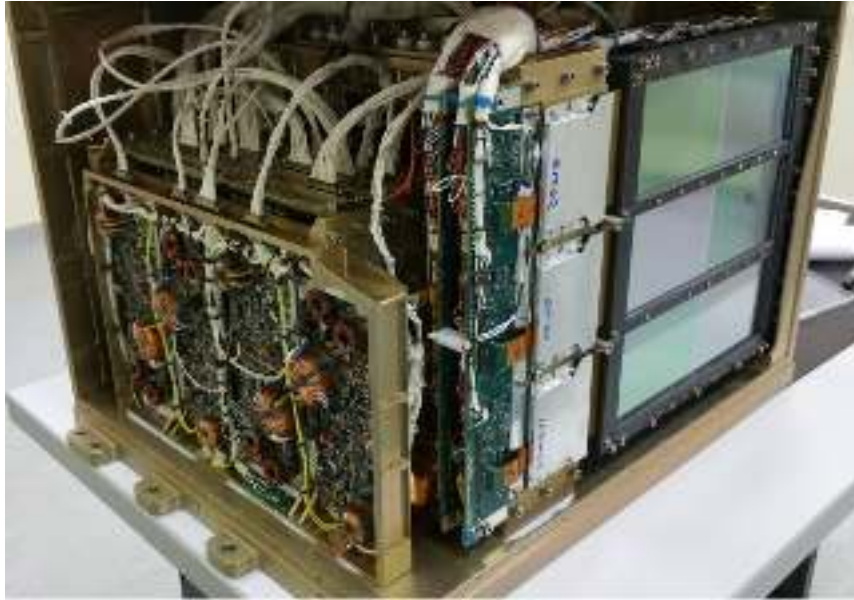


FIGURE 3.13: The electronics box and the silicon detector of the HEPD.

The electronic subsystem is composed by all front-end electronics and 4 boards:

- CPU board;
- Power Control board (TM/TC board);
- PMT/Trigger board;
- DAQ board.

All electronics boards are realized in 2 identical copies (main and spare side, or identically hot and cold side); in this configuration, the spare side is available in case of failure of the main side. Hot and cold sides are completely independent of each other and cannot be powered at the same time. A second level of redundancy has also been applied to some important components for each board (Sotgiu, 2018).

CPU board

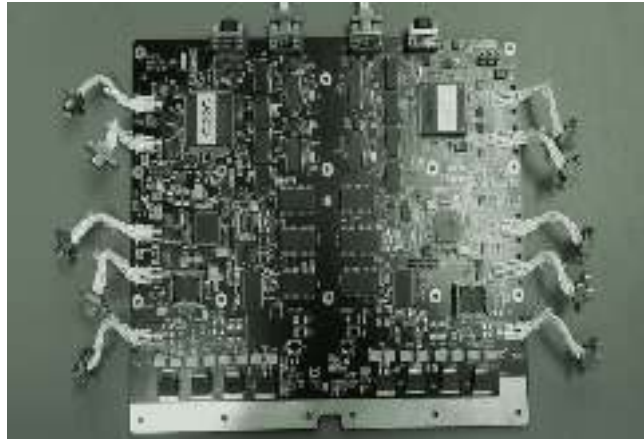


FIGURE 3.14: The CPU board of HEPD. The 2 sides HOT and COLD are visible.

The main CPU board is the digital subsystem that controls the detector status and communicates with the platform of the satellite via CAN BUS interface.

Among the main functionalities, the board manages the communication with satellite OBDH (On-Board Data Handling) computer, the storing of non volatile information, the management of system configuration and control, DAQ board, PMT/Trigger board, Power control board and HVPS board.

The main components of the board are an FPGA (Actel ProAsic3) for safe boot management and implementation of the slow control link; a digital signal processor ADSP; 2 CAN bus transceiver and 2 CAN bus controllers; a read-only EEPROM and a read-write FRAM used to store the application code for the digital signal processor.

TM/TC Power Control board

The TM/TC (TeleMetry/TeleCommand) Power Control board is responsible of the management of LVPS that provides bias to the electronics subsystem and of the physical local telemetry and telecommand signals.

The main functionalities of the TM/TC Power Control board are the management of direct TC, local TM, secure procedure in case of system or CPU failures and management and control of LVPS.

PMT/Trigger board

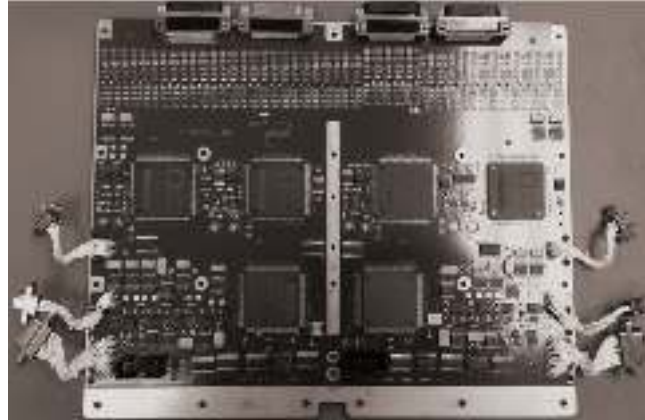


FIGURE 3.15: The PMT/Trigger board for HEPD. The 2 sides HOT and COLD are visible.

The PMT/Trigger board is responsible of the trigger subsystem and of PMT data acquisition. Its main functionalities are the acquisition of the 63 PMTs by means of the EASIROC ASICs, the analog-to-digital conversion of the PMT signals and the transfer to the data acquisition board (DAQ), the management of the trigger configurations.

To provide all these features, each side (HOT/COLD) of the board relies on an FPGA (Field Programmable Gate Array) Actel ProASIC, 2 EASIROC chips for the PMT read out and the implementation of the trigger patterns and 4 12-bit ADCs.

DAQ board

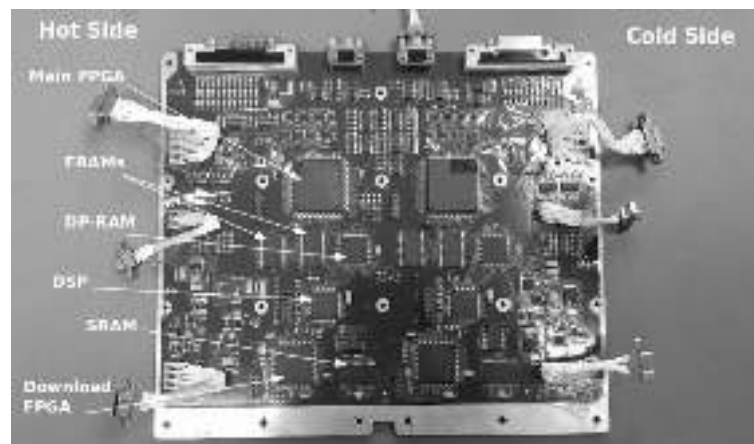


FIGURE 3.16: The DAQ board of HEPD. The 2 sides HOT and COLD are visible.

The DAQ board is the digital subsystem responsible of silicon data read-out and processing, acquisition and management of the scientific data format and transmission via RS422.

The main functionalities of the DAQ board are the configuration of the silicon detector and of acquisition modes, the interface with the front-end electronics of the silicon planes, the management of trigger signal from the PMT/Trigger board, the acquisition of silicon plane data and relative signal processing.

The operating frequency of the board was set at 48 MHz, as the best compromise between the requirements of fast operations and not-too-high power consumption.

3.2 Operation modes and in-flight calibration

The HEPD foresees different operation modes:

- **SAFE mode:** used at first power on for a period of a few hours. It is defined as all boards powered on and sets the PMT and Si HVPS to a zero safe value; during safe mode, only FAKE RUN is possible (a FAKE RUN is a special acquisition mode, that foresees the trigger board set in calibration mode to generate fake triggers and the DAQ in normal acquisition mode);
- **STAND-BY mode:** used at polar latitudes ($65^\circ < |\text{lat}| < 90^\circ$); during stand-by, powered boards are: LVPS, TM/TC power control board, HV control board and HVPS for Silicon detectors, CPU; the power consumption in stand-by mode is around 8 W.
- **NOMINAL mode:** when HEPD is in nominal operation mode, all boards are powered on and PMTs and Silicon planes are biased at operative HV values. The HEPD foresees the following main operational modes:
 - calibration modes: the PMT/Trigger board generates and sends to DAQ a false trigger for the calibration of both scintillator detectors and Silicon detector;
 - run modes: depending on the Silicon detector data processing, the run modes are: Virgin Raw (data are not processed); Zero-Suppressed (data are zero-suppressed, so that only useful signal information is stored and transmitted to Earth, and pedestals are subtracted).

In order to correctly calibrate the detector and drastically reduce the possibility of having real events in the random trigger, the calibration procedure is performed at the proximity of the Equator and outside the SAA region (standard calibration, performed every two orbits at the equator region).

For what concern the silicon detector, the ADC raw data of each strip is sent to the DSP of the DAQ board for processing. The silicon detector calibration algorithm is a 4-step procedure:

1. 1024 random events are taken and used to calculate the pedestal ped_i as:

$$ped_i = \frac{1}{N_1} \sum_{j=1}^{N_1} ADC_{ij}$$

where $N_1 = 1024$ and ADC_{ij} is the signal registered on the i -th channel for the j -th event.

2. 1024 random events are taken and used to calculate the RMS σ_i^{RAW} as:

$$\sigma_i^{RAW} = \sqrt{\frac{1}{N_2} \sum_{j=1}^{N_2} (ped_i - ADC_{ij})^2}$$

where $N_2 = 1024$, ped_i is the previously calculated pedestal for i -th channel and ADC_{ij} us the signal registered on the i -th channel for the j -th event.

3. 1024 random events are taken and used to calculate the pedestal without Common Noise (the jumping of the readout baseline common to all channels from event to event). For each ASIC, the common mode noise for j -th event is calculated as:

$$CN_j = \frac{1}{N_j} \sum_{i=1}^{N_j} (ADC_{ij} - ped_i)$$

where N_j is the number of the good strips within the ASIC (noisy or dead strips need to be excluded); the RMS without common noise is calculated as:

$$\sigma_i^{PED} = \sqrt{\frac{1}{N_3} \sum_{j=1}^{N_3} (ADC_{ij} - ped_i - CN_j)^2}$$

where $N_3 = 1024$.

4. 1024 random events are used to identify those strips that do not have a Gaussian distribution of the S/N in empty events.

The scintillator detectors calibration algorithm is equivalent to the first two steps of the silicon detector calibration algorithm.

3.3 Trigger configurations and orbit settings

The trigger configuration of HEPD detector foresees 9 predefined trigger masks, among which one is a configurable generic mask. Each of these predefined trigger masks can be used with different veto settings: without veto, with lateral veto, with bottom veto, with the whole veto (lateral and bottom). The trigger mask configuration is passed to the CPU board through a multi-frame TC.

The predefined trigger configuration masks implemented on the firmware for the PMT/Trigger board are:

1. T
2. T & P1
3. T & (P1 || P2)
4. (T3 || T4) & (P1 || P2)
5. T & P1 & P2
6. T & P1 & P2 & P3
7. T & (P1 || P2) & (P15 || P16)
8. T & (P1 || P2) & L
9. Generic trigger mask

where: T means the OR of the 12 PMTs of the segmented trigger plane; T3 and T4 means the OR of the 2 PMTs of the 3rd and 4th counter of the segmented trigger plane (the central paddles); P1, P2, ..., P16 means the OR of the 2 PMTs of the 1st, 2nd, ..., 16th plastic scintillator planes; L is the OR of the 9 PMTs of the LYSO crystals. The thresholds set in the trigger software to generate a signal were chosen in order to get a trigger for MIP (Minimum Ionizing Particles) events.

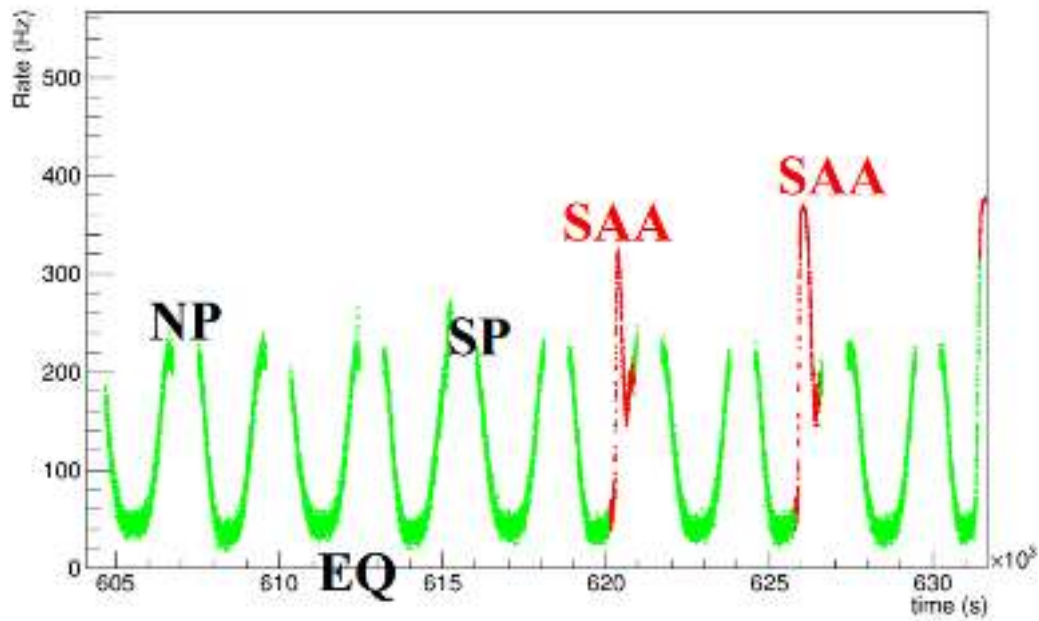


FIGURE 3.17: HEPD trigger rate as function of on-board time for a few orbits. Different regions are marked (P. Picozza et al., 2019).

The trigger mask is chosen to take into account the orbital zone and the corresponding expected rate, the maximum rate acceptable by electronics and the type of particle and range of interest. After a period of commissioning, completed in August 2018, the trigger configuration of HEPD has been set to T & P1 & P2.

Depending on the zone along the orbit, different trigger masks can be applied in order to limit the detector acceptance; moreover, as the data rate depends on the orbital zone, the run duration can be configured in each zone. Different orbital zones were defined in HEPD software in order to change automatically these configuration along the orbit: equatorial, South polar, North polar, SAA and default (when no orbit information is available). Fig. 3.17 shows HEPD trigger rate as function of the on-board time for a few orbits.

The CPU monitors the orbital position (from broadcast information) and send the information to the DAQ board. If the broadcast information is not available or orbit position is unknown, the default configuration is used.

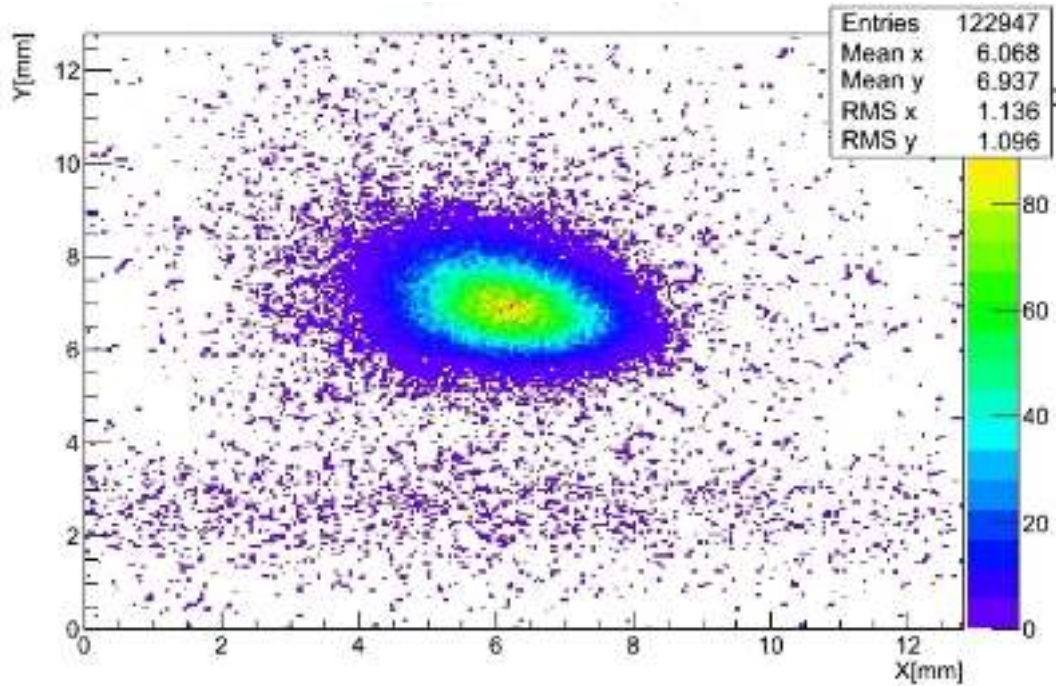


FIGURE 3.18: The beam spot for a run of 3500 bunches (25 electrons per bunch) with energy 450 MeV detected with a Medipix.

3.4 Beam test

In order to study the detector functionality and characterize the detection performances for different particles, several beam tests were performed on the flight model of the HEPD after the integration campaign.

Electron tests took place in October 2016 at the Beam Test Facility of Laboratori Nazionali di Frascati (INFN-LNF). The parameters of the BTF were optimized to obtain beam bunches of low multiplicity (0, 1, >1 electrons, according to a Poisson distribution) for different energies: 30, 45, 60, 90 and 120 MeV. A calorimeter was used for beam spectra and multiplicity monitor and a Medipix (read-out chip for particle imaging and detection) for beam spot monitor. The beam spot radius was $4.9 \times 5.3 \text{ mm}^2$ at 30 MeV; fig. 3.18 shows the beam profile for a run with energy 450 MeV. Air distance between beam exit point and HEPD window was about 140 cm.

The HEPD was placed in front of the beam on a movable platform and operated as in space. Data collected were transmitted to the EGSE (Electrical Ground Support Equipment), that is a module that emulates the satellite and manages the main power; it was controlled remotely from the control room.

The detector was performed at different incident beam angles and positions, with different trigger masks, veto settings and PMT thresholds. In

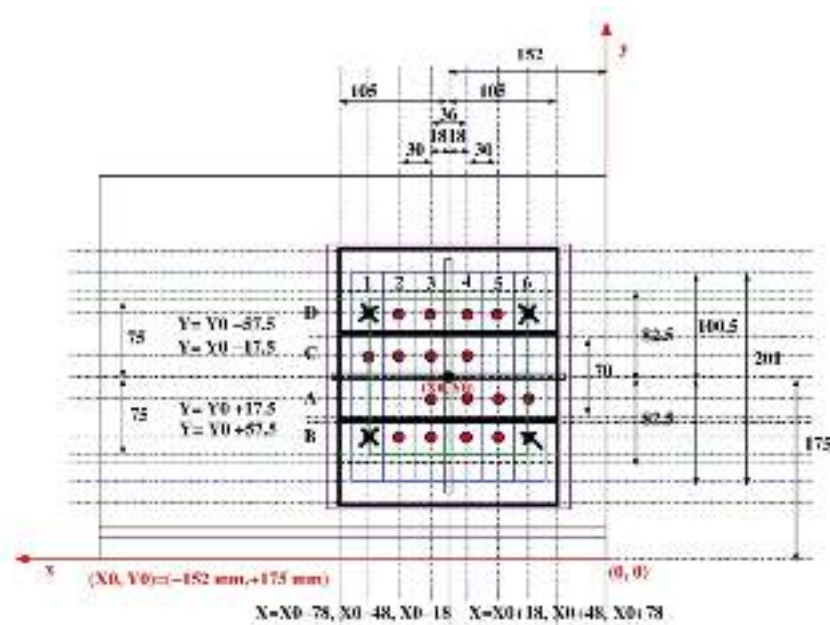


FIGURE 3.19: HEPD window (violet) with the three ladders of silicon (black) and the six trigger paddles (blue) superimposed. The red points represent the beam positions during electron beam test; points coordinates correspond to the set coordinates of the movable platform (numbers in red).

particular, runs in position 4A (see fig. 3.19) were executed for all beam energies.

The proton test was performed in November 2016 at the Proton Therapy Center in Trento (Italy), where a cyclotron produces protons at energies ranging between 70 and 230 MeV. Energies below 70 MeV were obtained by using degraders along the beam line, consisting in 2 thicknesses of Solid Water (RW3). An auxiliary scintillator read out by Micro Channel Plate was placed on a side of the HEPD to check beam rate and energy.

The isocenter of the beam (the point through which the central beam of radiation passes) was positioned at 1.25 m from beam exit point; the spot size at the isocenter changed from 3 to 7 mm, depending the beam energy (see table 3.3). Air distance between beam exit point and HEPD window was 1.86 m. The detector was irradiated with protons at different energies between 37 and 228 MeV (Picozza, P. et al., 2017).

Also in this case, the detector was performed at different incident angles and positions, with different trigger masks, veto settings and PMT thresholds. In particular, runs in position 3C (see fig. 3.19) were executed for all beam energies.

Finally, after these tests, several acquisitions of atmospheric cosmic ray

Energy (MeV)	σ_X (mm)	σ_Y (mm)	$\bar{\sigma}$ (mm)
37*	-	-	-
51*	-	-	-
70	6.87	6.91	6.89
100	5.81	5.86	5.84
125	5.21	5.23	5.22
154	4.36	4.34	4.35
174	3.83	3.87	3.85
202	3.39	3.39	3.39
228	2.92	2.90	2.91

TABLE 3.3: The proton beam energies used for tests are reported, together with beam spot size at isocenter. The energies marked with (*) were obtained positioning a RW3 degrader in front of the 70 MeV beam, respectively 25 and 16 mm thick.

data were conducted in the INFN Roma2 clean rooms in October and November 2016. The analysis of these runs was mainly focused on the optimization of the in-flight data handling software, and afterwards on the sub-detector digitization analysis.

The electron, proton and muon tests allowed to characterize all the sub-detectors hit by the triggering events in the whole dynamic operational range.

After the launch of HEPD, a beam test with light nuclei was performed on the Qualification Model of the detector (a second prototype of the instrument not destined to the flight), held in June 2018 at Laboratori Nazionali del Sud of Istituto Nazionale di Fisica Nucleare in Catania (Sicily, Italia).

Chapter 4

Monte Carlo software and energy reconstruction

The analysis for the energy reconstruction of the event makes an important use of the ADC signals of calorimeter and is realized with the support of the MC software.

The chapter opens with the description of the Monte Carlo software in all its configuration (protons, electrons, light nuclei beam tests, muon acquisition simulation, flight conditions); the simulated performance of the detector are studied. The second section of the chapter deals with the development of the procedure followed to digitize the light collected at PMTs in ADC signal, in order to obtain an output as similar as possible to the real detector.

The other sections are dedicated to the energy reconstruction of the event. The first calibration method described in the chapter consists in exploiting the beam test analysis, using electrons, protons and muons runs. The relevant quantity for the energy determination of the event is the ADC signals sum of the PMTs in the whole calorimeter.

A second method exploits the sampling geometry of the 16-planes calorimeter. As this is a completely MC-based approach, its results were successively verified by beam test analysis. Depending on the plane where the particle stopped, its original energy can be retrieved with a certain error which is function of the plane thickness. This method can only be applied to proton events in a specific energy range.

The last section hints at the development of a neural network trained on a sample of the digitized MC and tested on an independent sample and on beam tests runs. The output of the neural network includes particle type, direction and energy of the event.

4.1 Monte Carlo software

The performance of the HEPD using different particles and energies was studied with a Monte Carlo (MC) software based on the Geant4 package.

Volume material	Elements	Density (g/cm ³)
Tracking sensor	Si	2.33
Plastic scintillator EJ200	H, C	1.032
Crystal scintillator LYSO	Lu, Y, Si, O, Ce	7.1
Carbon fiber cross	C	1.58
Poron cross	H, C, N, O	0.32
Mechanical grid	Al	2.7
Window panel mylar	H, C, O	1.4
Window panel kapton	H, C, O	1.42
Window panel copper	Cu	8.96

TABLE 4.1: List of materials and relative density in the way they are parameterised in the MC software.

Geant4 is a toolkit for the simulation of the passage of particles through matter; its areas of application are in high energy, nuclear and accelerator physics and studies in medical and space science (Allison, J. et al., 2006; Allison, J. et al., 2016).

This simulation toolkit includes a complete range of functionality comprising tracking, geometry, physics models and hits. The proposed physics processes cover a comprehensive range, among which electromagnetic, hadronic and optical processes, a large set of long-lived particles, materials and elements, over a wide energy range starting, in some cases, from 250 eV and extending in others to the TeV energy range. It has been designed and constructed to expose the physics models utilised, to handle complex geometries, and to enable its easy adaptation for optimal use in different sets of applications. The toolkit is the result of a worldwide collaboration of physicists and software engineers. It has been created exploiting software engineering and object-oriented technology and implemented in the C++ programming language (Agostinelli, S. et al., 2003).

4.1.1 Code structure

The simulation software is organized in several parts, each of which takes into account the possibility to change some of its parameters (e.g. primary generator, materials or stepping actions). The three main parts in which the HEPD MC software is divided are the geometry, the output data information and the simulation itself.

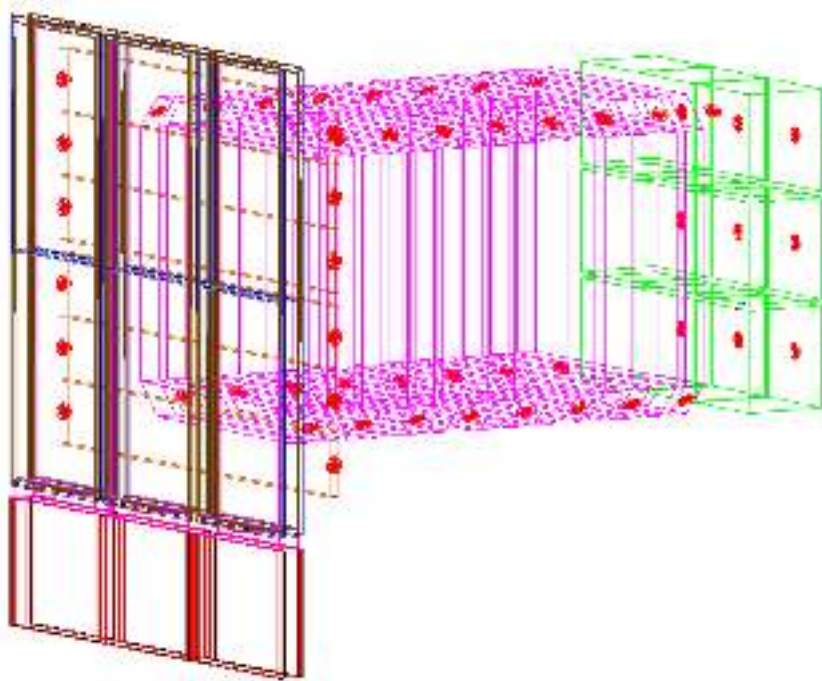


FIGURE 4.1: The graphic visualization of the HEPD MC software. Silicon tracker is highlighted in blue and brown, with the electronic boards in red; trigger scintillator bars are colored in orange, tower scintillators in pink, LYSO crystals in green; the PMTs of the scintillators are visible in red. Veto planes, HEPD box, satellite wall and passive materials are not shown.

The geometry of the software is very detailed (see fig. 4.1). It includes the sub-detectors described in last chapter and the support mechanic materials (carbon fiber, poron, aluminium). Each volume is implemented with the corresponding material and its relative density; a list of the main materials and densities of HEPD is shown in table 4.1.

The output data of the simulation is readable with the ROOT data analysis software, a modular scientific toolkit (Antcheva, I. et al., 2009) able to provide most of functionalities needed to deal with big data processing, statistical analysis, visualization and storage. The format is structured in hit collections, one for the track informations, one for the interactions eventually occurred during the route in the detector and one for each sub-detector. The format includes also methods used to obtain physical information and quantities.

The simulation itself comprises sensitive detector implementation (tracker and scintillators, but also PMT volumes), primary generation details (particle type, position and direction, energy) and physics lists to be uploaded. Several physics lists are available in the software; the lists used for the great part of studies realized in HEPD experiment were chosen depending on the energy range and the physical phenomena of interest for HEPD; they are the electromagnetic standard ("option4"), the hadron and ion elastic and the hadron and ion inelastic physics ("Shielding").

4.1.2 Configurations

The HEPD MC software is able to work in several configurations, depending on the kind of event that must be simulated. Three beam test configurations (electrons, protons and light nuclei) have been implemented, each one having certain parameters (presence of a degrader or a collimator, air distance, beam spot simulation) set as in the corresponding real test.

A configuration for muon runs is available, simulating atmospheric muon behaviour at Earth surface with a well studied angular and energy distribution (Cecchini, 2012), and one for flight conditions (generation from a sphere surrounding the detector and with energy power-law spectrum).

A special geometry configuration was developed for the behaviour of optical photons in the scintillators. For this configuration, optical physics list is activated, including the scintillator emission spectra, the transport and absorption effects inside the scintillator, the reflectivity phenomena and relative parameter. Moreover, this configuration comprises the presence of cylindrical shape volumes simulating PMTs, positioned in the same positions of the real

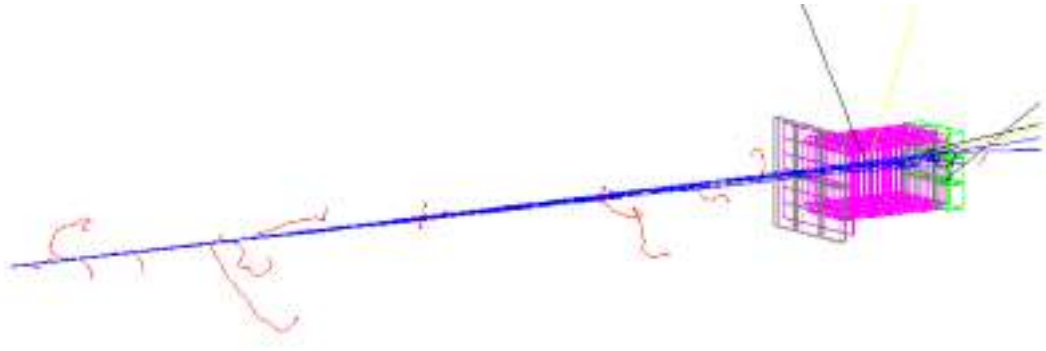


FIGURE 4.2: 10 events of 202 MeV protons in the beam test proton configuration. A distance in air of 186 cm was set between generation point and HEPD window.

ones (at the ends of each trigger bar, at the two corners of a plane, etc.; see fig. 4.1).

In the real case, not every photon reaching the PMT surface is automatically acquired (i.e., becomes a photoelectron): a PMT quantum efficiency is expected, due to probability photoemission of electrons from the photocathode; this efficiency depends on the photon's energy (fig. 3.11). To implement this effect in the simulation, each time a photon with energy E reaches the volume of a PMT, a random number in $[0,1]$ is generated and evaluated whether greater or lower than the quantum efficiency value at energy E ; if lower, the photon is considered acquired and the photoelectrons counter for this PMT is incremented by 1; the quantum efficiency is considered the same for all the PMTs and is set according to the datasheet value. This procedure is implemented for all PMTs, included veto ones. Fig. 4.3 shows the general chain of optical photons implementation: because of an energy deposit, a certain number of photons is generated in the scintillator planes; depending on its geometry, its absorption spectrum, the boundary reflectivity properties and the PMTs geometry, only a fraction of the generated photons reaches the PMT cylinder; finally, after the quantum efficiency filter, a further fraction is registered as photoelectrons.

4.1.3 HEPD simulated performances

A simulation was carried out to study the detector performances. The simulated data set consisted in 1 million of electrons and 1 million of protons with uniform energy spectra, between 1 and 100 MeV and 1 and 300 MeV

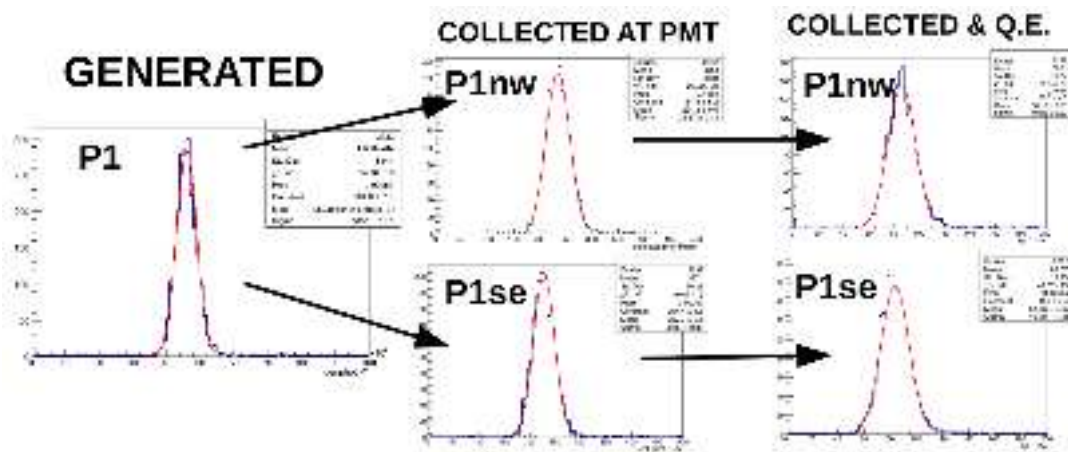


FIGURE 4.3: Optical photons implementation chain: a bunch of photons is generated in the plane, some of them arrives at the PMT volumes, and a further fraction of them passes the q.e. and is registered as photoelectrons. The distributions in figure shows the number of photons for each step (P1se and P1nw are the names of the 1st plane PMTs.)

respectively; angular spectrum is uniform in $\cos^2\theta$ in both cases, to simulate an isotropic flux.

Fig. 4.4 shows the minimum and maximum energy range detectable by the instrument, where minimum means the energy thresholds for trigger and maximum means the maximum energy at which the event is fully contained in the calorimeter. In all the four plots in fig. 4.4, on X-axis the kinetic energy of the primary in MeV is reported. In the two plots on the left, Y-axis reports the number of events (electrons on the top and protons on the bottom) passing some trigger conditions divided by the total number of events; in the two plots on the right, Y-axis reports the number of events (electrons on the top and protons on the bottom) contained in the calorimeter divided by the total number of events.

Not every particle crossing the instrument is effectively registered by the trigger or, despite registered, used in data analysis. In fact, some particles enter in or exit from the detector via veto panels: in the first case, the particle doesn't trigger the detector and signals are not acquired; in the second case, the event hits one or more veto panels: for this kind of event, it is not true that the energy is fully deposited inside the detector, and it is discarded. All these particle behaviours are described by the notion of geometrical factor and by its dependence on energy.

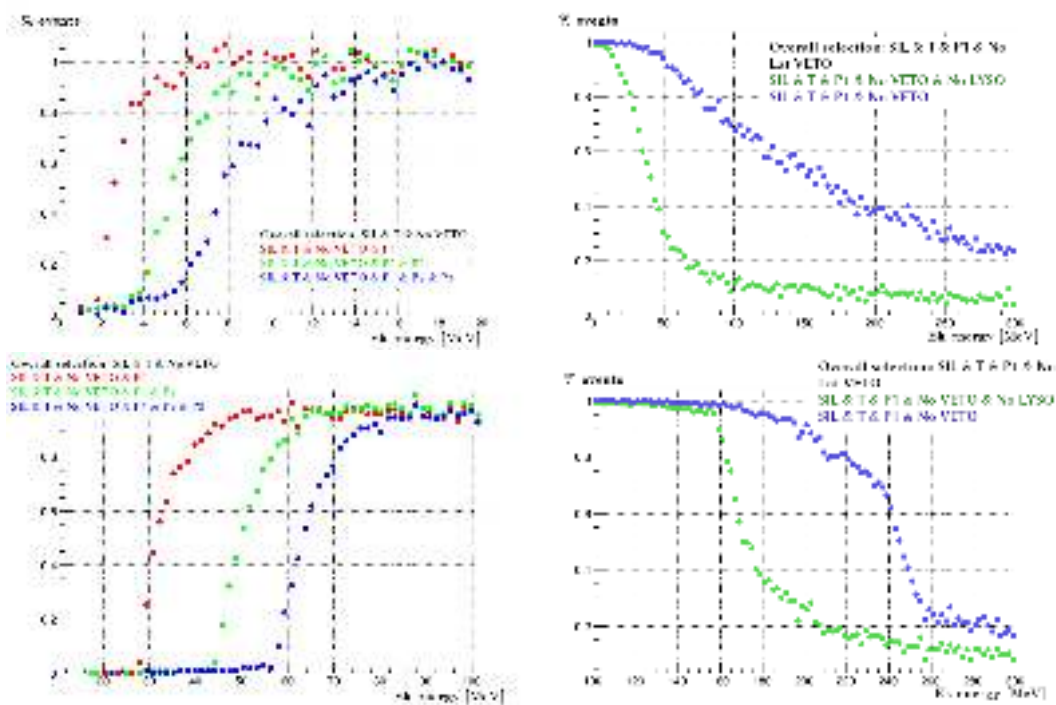


FIGURE 4.4: Left: Fraction (top) of electrons and (bottom) of protons passing some trigger conditions as a function of primary energy. Right: Fraction (left) of electrons and (right) of protons contained in the tower and in the calorimeter as a function of primary energy.

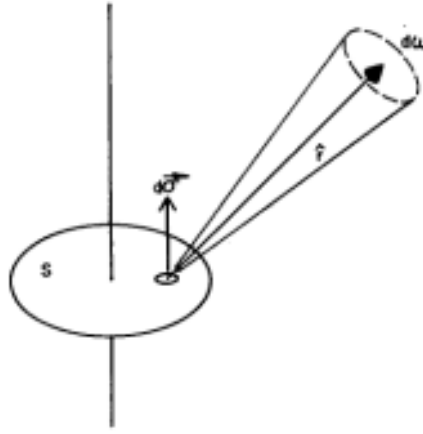


FIGURE 4.5: A telescope with a single plane detector viewing one hemisphere.

The geometrical factor of a detector is defined as:

$$GF = \int_{\Omega} d\omega \int_S d\sigma \cdot \hat{r} \quad (4.1)$$

where $d\omega$ is the infinitesimal solid angle, Ω is the domain of $d\omega$, $d\sigma$ is the element of surface area of the last sensor telescope to be penetrated, \hat{r} is the unit vector in direction ω ; $d\sigma \cdot \hat{r}$ is the effective element of area looking into ω (fig. 4.5). In the case of a single plane detector, the geometrical factor is evaluated as:

$$\begin{aligned} GF &= \int_{\Omega} d\omega \int_S d\sigma \cdot \hat{r} = \int_{\Omega} \int_S \cos\theta \, d\sigma \, d\omega = \\ &= 2\pi A \int_0^1 \cos\theta \, d\cos\theta = \pi A \end{aligned} \quad (4.2)$$

where Ω is a full hemisphere (particles incident from one side of the detector) and $A = \int_S d\sigma$ is the surface area of the detector; if particles are incident from both sides, the area of the detector is doubled (Sullivan, 1971).

The geometrical factor of a detector can be calculated via MC as the ratio between the number of particles passing certain selections N_{SEL} and the total number of simulated particles N_{TOT} , normalized to the generation surface S :

$$GF = 2\pi S \times \frac{N_{SEL}}{N_{TOT}} \quad (4.3)$$

The geometrical factor is measured in $\text{cm}^2 \text{ sr}$. In fig. 4.6 the geometrical factor of HEPD, calculated using the simulation described above, is represented as a function of primary energy; it was obtained selecting events

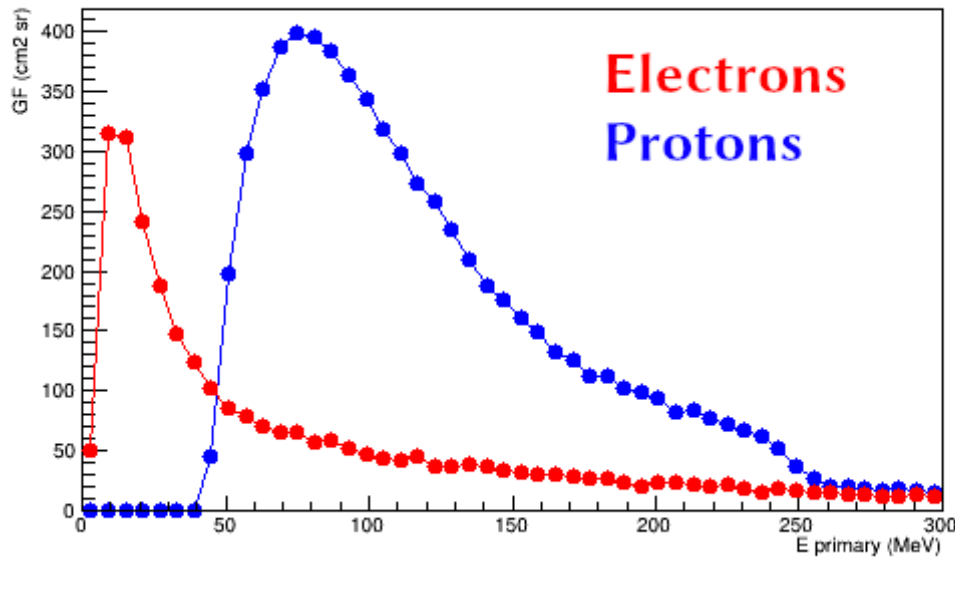


FIGURE 4.6: The geometrical factor as a function of primary energy calculated from simulation for electrons and protons. Selections applied are T&P1&P2 and veto containment.

passing the trigger condition T&P1&P2 and requesting no veto panel hit.

Another performance study conducted by MC is the particle discrimination between electrons and protons. One of the most used methods is the dE/dX vs E method. Due to the different ionization release of protons and electrons in a thin layer of material, these two types of particle can be distinguished. Fig. 4.7 shows the energy release in the 1st tracker plane as a function of the total deposited energy, for events contained in the instrument. The two populations clearly distinguishable are protons (following a Bethe function) and electrons (behaving like a minimum ionizing particle).

4.2 Digitization procedure

In order to make the MC output as similar as possible to the HEPD data format, maintaining meantime the MC truth informations, a digitization procedure was developed on the MC software. The digitization of MC data consists in the conversion of a physical quantity (often associated with the detector response) in voltage/current values or digit counts. In the case of the HEPD MC, the physics quantity to be converted is the light collected by each PMT; the output quantity to be produced must be an ADC counts signal.

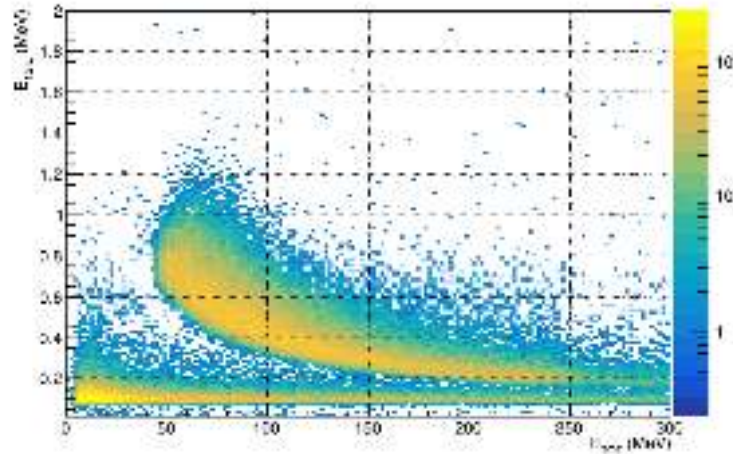


FIGURE 4.7: Energy release in the 1st tracker plane as a function of the total deposited energy calculated from simulation for electrons and protons; the coloured axis shows the number of events. Selections applied are T&P1&P2 and veto containment.

Fig 4.8 reports the distributions of collected photoelectrons (from simulated beam tests) and ADC (from real beam tests) of a PMT of one calorimeter plane for protons, electrons and muons; the distributions are fitted with a Gaussian curve for protons and with a Landau curve for electrons and muons.

It was hypothesized that the relation between photoelectrons acquired by the PMT (from here on, PE) and ADC counts is an arctangent function of the form:

$$ADC = p_0 \cdot \arctan(p_1 \cdot PE + p_2) + p_3 \quad (4.4)$$

This was done to keep into account the effect of electronic amplifiers (the Taylor series around 0 is a 3rd degree polynomial) and of an eventual saturation trend (the asymptote of the arctangent). It should be noted here that the Birks effect could be visible in a relationship manifestly involving the energy deposit in the scintillator (deposited energy vs photoelectrons, for example), while it is not true in an ADC-PE relationship because it affects both ADC and PE quantities.

The 4 digitization parameters p_0 , p_1 , p_2 and p_3 are different for each PMT because of the different voltage at which each of them works. These parameters were calculated using the beam tests data, during which the most part of sub-detectors was characterized as a function of incident energy; for the photoelectrons collected during beam tests in each PMT, the MC software beam configurations were used to simulate the optical photons generation when

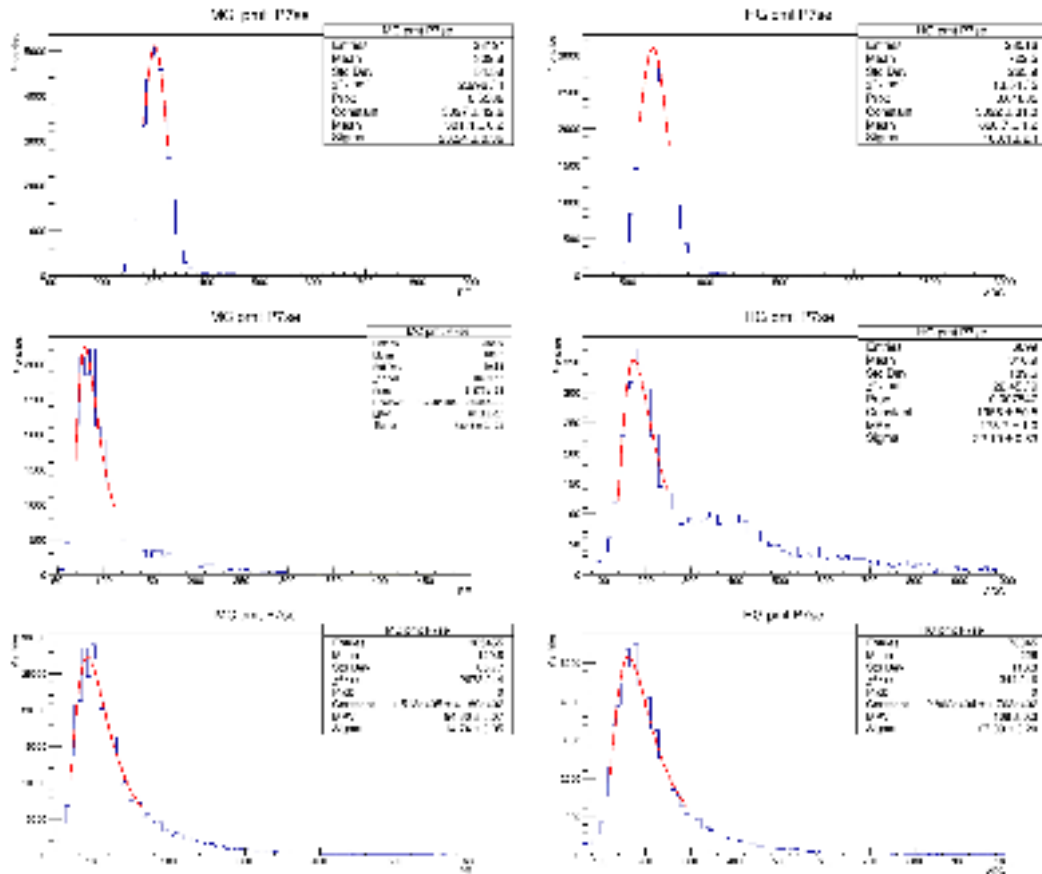


FIGURE 4.8: Distributions of collected photoelectrons (PE, left) and ADC (right) of a PMT of the 7th calorimeter plane for 154 MeV protons (top), 120 MeV electrons (center) and muons (bottom); PE distributions are from simulated beam test, ADC distributions from real beam test. All distributions are fitted (red line) with a Gaussian curve for protons and with a Landau curve for electrons and muons. Fit parameters are reported in the corresponding box.

the particle was launched with the same energy, from the same point and at the same distance from HEPD, as the real case.

A special effort was carried to make beam tests simulation as similar as possible to actual situation. The center position and the size of the beam spot were checked by means of the silicon detector signals and reproduced in the simulation. Fig. 4.9 reports the channel distributions of the one silicon ladder for five energies during the proton beam test; as expected, the width of the Gaussian shape (i.e. the beam spot size) decreases at increasing beam energy. Also this energy-dependent effect of beam spot size was taken into account in the simulation of beam tests.

The digitization procedure explained below was applied to PMTs of the trigger bars hit during beam tests, of the calorimeter planes and of the LYSO cubes; the digitization of veto PMTs was not possible because during the beam tests they presented no signal, except in the case of muons run, that alone is insufficient to derive digitization factors. Because of limited time at beam tests, it was not possible to develop runs with the beam centered on veto planes for their calibration and digitization; this is not a problem because veto planes are used as booleans to determine whether they are hit, and not for energy determination.

ADC distributions of PMTs for protons, electrons and muons test runs were selected using the following cuts:

- the most significant trigger paddle, which is the paddle with the highest ADC signal, hit and the 1st plane hit (all PMTs over 10 standard deviations); a standard deviation of an event for the i -th PMT is defined as:

$$SD = \frac{ADC - PED_i}{\sigma_i} \quad (4.5)$$

where ADC is the signal released by the event in the PMT, PED_i and σ_i are respectively the pedestal value and pedestal sigma of the i -th PMT;

- trigger multiplicity equal to 1 (all PMTs not belonging to the most significant paddle under 5 SD);
- no hit in any veto (both PMTs under 5 SD) for protons and electrons runs; no hit in any lateral veto (both PMTs under 5 SD) for muons runs.

PE distributions of PMTs for protons, electrons and muons simulated runs were selected using the following cuts:

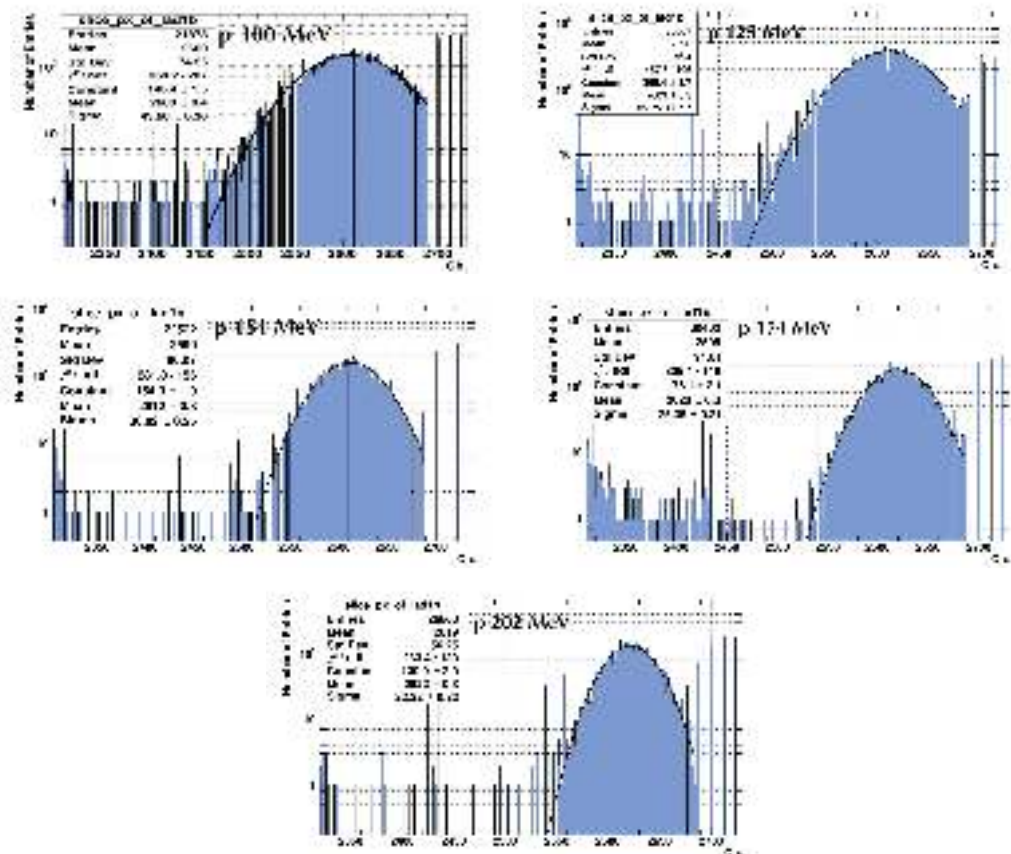


FIGURE 4.9: Channel distributions of the same silicon ladder for five energies of the proton beam test (respectively, from top left: 100, 125, 154, 174 and 202 MeV) and the corresponding Gaussian fit (black line). The width of the Gaussian shape (corresponding to the beam spot) clearly decreases at increasing beam energy.

- the most significant trigger paddle, which is the paddle with the highest photoelectrons detected number, hit and the 1st plane hit (all PMTs with at least 20 photoelectrons detected);
- trigger multiplicity equal to 1 (all PMTs not belonging to the most significant paddle with maximum 3 photoelectrons detected);
- no hit in any veto (all veto planes with a deposited energy lower than 0.2 MeV) for protons and electrons runs; no hit in any lateral veto (all lateral veto planes with a deposited energy lower than 0.2 MeV) for muons runs.

As was noted, the thresholds used for PE selection cuts are in photoelectron number: they were appropriately derived from thresholds of ADC selection cuts via energy release in the various sub-detectors (for example, a signal threshold of 5 SD in a calorimeter plane corresponds to an energy release of 0.4 MeV according to beam calibration, which corresponds in turn to a number of 20 photoelectrons collected by one of the two PMTs according to MC).

The values of the peak distributions obtained were then correlated in ADC-PE plots, one for each PMT, with vertical (horizontal) uncertainties corresponding to the sigma fit parameter of ADC distributions (PE distributions). The points were fitted with a function of the type of Eq. 4.4 to derive the digitization factors. Fig. 4.10 shows the peak of ADC pedestal-subtracted signal (data, on Y axis) as a function of light collected (MC, on X axis) from some PMTs of the trigger (high gain), upper calorimeter (high gain) and LYSO (low gain) using all proton, electron and muon runs.

To properly digitize a MC file, digitization parameters are applied to MC light distributions; then, the pedestal is added as a shift of the distribution. The shift value is evaluated for each event as a gaussian random number, with a peak and a sigma equals to the peak- and sigma-pedestal value measured in calibration runs during beam tests. Fig. 4.11 shows the comparison between distributions of real and reconstructed ADC signal for some PMTs of the trigger (high gain), upper calorimeter (high gain) and LYSO (low gain) during the 202 MeV proton test; the two distributions are normalized to the number of events.

Having a digitized MC, able to reproduce the same signal of the detector, is crucial for several steps in data analysis. To this purpose, some MC runs were produced and digitized. In particular, the digitization of a full-range MC run allowed the study of all those features that cannot be studied

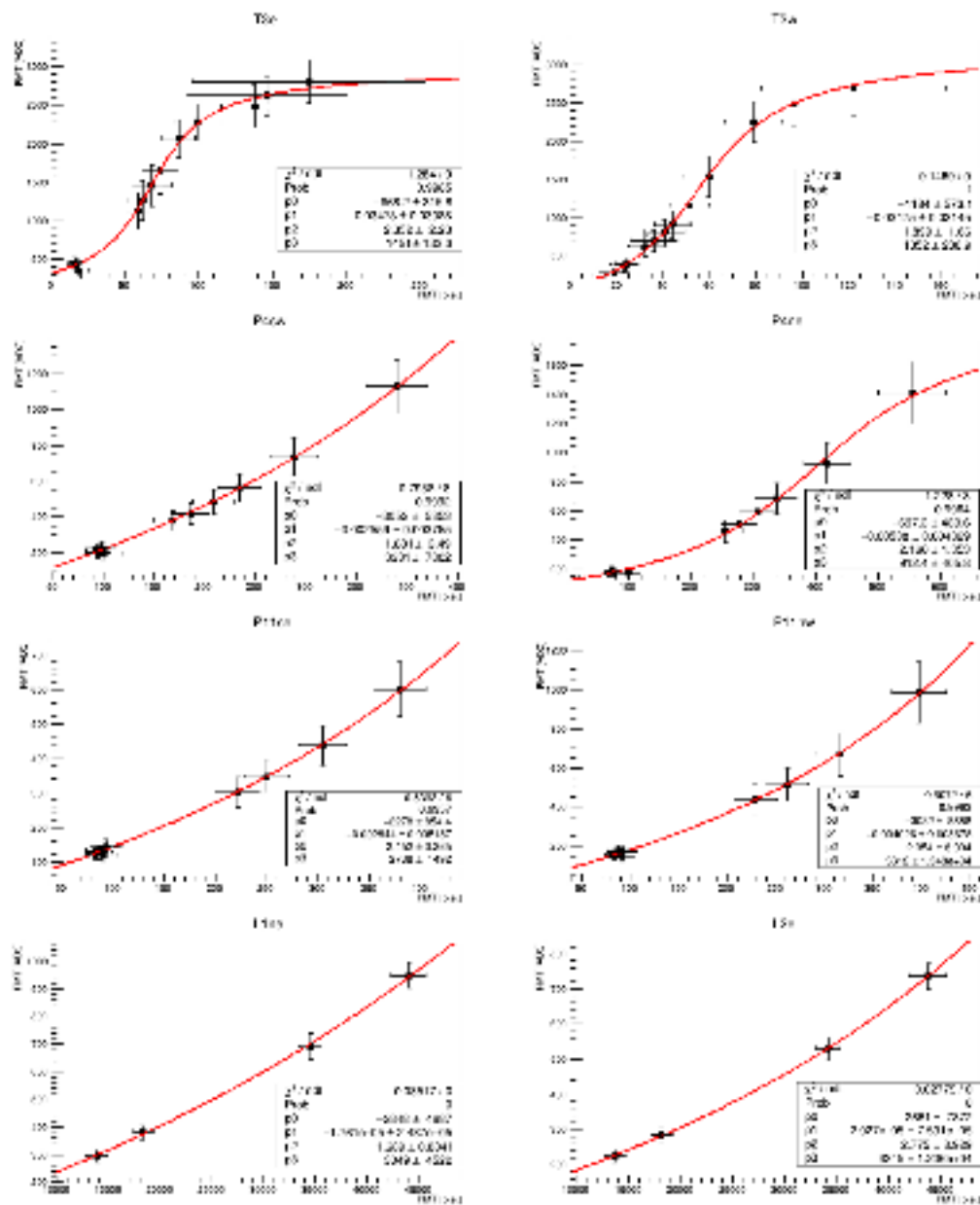


FIGURE 4.10: Peak of ADC pedestal-subtracted signal (data, on Y-axis) as a function of light collected (MC, on X-axis) from some PMTs of the trigger (high gain), upper calorimeter (high gain) and LYSO (low gain) during all proton, electron and muon runs. The vertical (horizontal) uncertainties correspond to the sigma fit parameter of each ADC (PE) distribution. The points are fitted with an arctangent function.

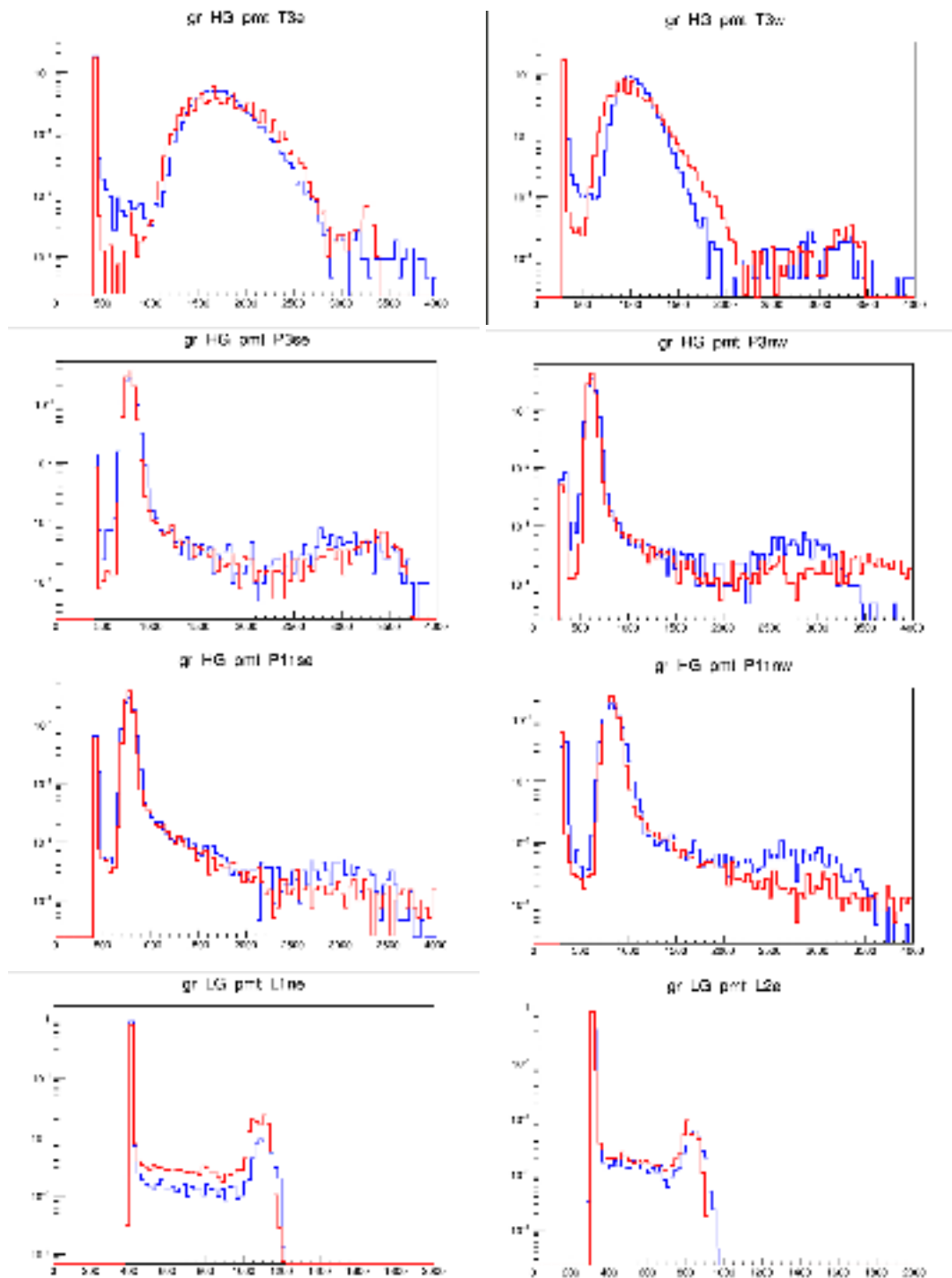


FIGURE 4.11: Comparison between distributions of real (blue) and reconstructed (red) ADC signal for some PMTs of the trigger (high gain), upper calorimeter (high gain) and LYSO (low gain) during 202 MeV proton test. The two distributions are normalized to the number of events.

in flight, such as the efficiencies of selection cuts. This MC consists in the simulation of 10 million protons with uniform energy spectrum, between 10 MeV and 1 GeV; angular spectrum is uniform in $\cos^2\theta$ and ϕ and generation surface is a $40 \times 40 \text{ cm}^2$ square on a plane 1 cm away from HEPD window volume.

For the HEPD detector does not have instrument redundance for the measurement of the same quantity (like energy), the only way to check the detector response is to use the MC. MC truth can provide a general description of performances, but it is no longer reliable when it comes to deal with detailed information: a higher precision is needed, that can only be obtained with digitization. Through digitization, the MC can be tuned with the real detector response, including electronic effects, like saturation, or physical effects, such as light collection efficiencies; another possibility for digitization is to study selections similar to those applied to flight data. In fact digitization is able to reproduce, using the optical photon information, the response of the two PMTs at the corners of planes, which is not present among MC truth informations.

With digitization, it is possible to study the geometrical factor selecting events with thresholds in ADC signal. In particular, the information of the two PMTs positioned on veto planes is examined, using selection with PMTs in AND or PMTs in OR.

Fig. 4.12 shows the proton geometrical factor calculated in three ways:

- with the MC truth: the events are selected using thresholds at MIP/4 on the deposit of energy;
- with MC digitization: veto PMTs in AND with threshold at MIP/4 on photoelectron number and all other selections with threshold at MIP/4 on ADC signal;
- with MC digitization: veto PMTs in OR with threshold at MIP/4 on photoelectron number and all other selections with threshold at MIP/4 on ADC signal.

where the selection with veto PMTs in AND means that the event is rejected if, for each veto plane, both PMTs have a signal over threshold, while the selection with veto PMTs in OR means that the event is rejected if, for each veto plane, at least one of the two PMTs has a signal over threshold. Also in the digitized MC the selections are based on the threshold of MIP/4, wherever possible on the value in ADC (the value in ADC generated by a MIP is

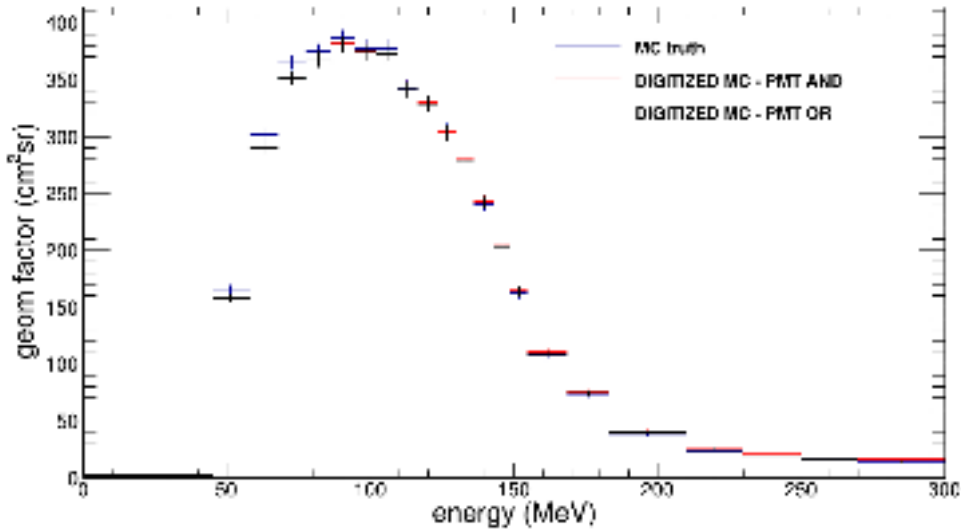


FIGURE 4.12: Geometrical factor for protons calculated with selections in energy deposit (blue; MIP/4 on energy deposit), with selections in ADC, requesting the AND of veto PMTs (red; MIP/4 on PE for veto selection and on ADC value for other selections) and with selections in ADC, requesting the OR of veto PMTs (black; MIP/4 on PE for veto selection and on ADC value for other selections).

estimated from a run of acquisition of atmospheric muon); for veto, where the digitized ADC value is missing, the threshold of MIP/4 is set on the photoelectron number (the number of photoelectrons generated by a MIP is estimated from a simulation of muons with optics).

It can be noted that in the simulation there is no difference between the two cases with digitized MC (PMTs in AND or PMTs in OR). The only visible difference is between digitized MC and MC truth: the agreement is good for high energies, but in the first bins the geometrical factor obtained from MC truth is overestimated. It may depend on the fact that digitization contains effects of scintillation efficiency, light propagation in scintillating volumes and PMT efficiency. On the contrary, the MC truth is only based on energy deposit: it does not consider the light transmission from generation to PMT and it may underestimate the energy threshold needed for the trigger.

4.3 Beam test calibration

For the energy calibration of the calorimeter, proton, electron and muon runs were used. For a correct calibration analysis, an equalization procedure was

developed for the detector PMTs and a preliminary beam test analysis was done to quantify efficiencies of different cuts applied to the samples.

4.3.1 Equalization

This procedure was set up to equalize the PMT responses to Minimum Ionizing Particles (MIPs); as a MIP is expected to release the same energy in each plane, atmospheric muons data allowed to equalize PMT signals correcting for different PMT gains, optical-couplings to planes and scintillator and collection efficiencies.

In order to equalize PMT response of both sides of HEPD electronics (HOT and COLD), cosmic muon data were collected in the two configurations. After subtracting the pedestal from the raw ADC signal of each channel, vertical muon events passing through all the apparatus were selected. Selection applied to muon sample consists in:

- one of the two central trigger paddles (T3 or T4) hit (both PMTs over 5 standard deviations); a standard deviation is defined as in Eq. 4.5;
- the central LYSO crystal (L5) hit (PMT signal over 5 standard deviations);
- LYSO multiplicity equal to 1 (no signal on the other LYSO crystals);
- the bottom veto plane hit (PMT signals over 5 standard deviations);
- no hit in any lateral veto.

The MIP signal distribution for each PMT was fitted with a Landau function. The equalization coefficient K_i^{EQ} of the i -th PMT was obtained by scaling the peak to the arbitrary value of 200 ADC counts: $K_i^{EQ} = 200/MPV_i$, where MPV_i is the Most Probable Value as obtained from the Landau fit of the ADC signal distribution of the i -th PMT. Once estimated the equalization factor for each PMT, the raw ADC signals were equalized on event-by-event basis, according to the following formula: $S_i^{EQ} = K_i^{EQ} S_i^{RAW}$, where S_i^{RAW} is the raw signal measured for the i -th PMT and S_i^{EQ} is the equalized signal (Ambrosi, G. et al., 2019).

4.3.2 Calorimeter energy calibration

The light collected by the two PMTs placed at the corners of each scintillator plane is slightly dependent on the position of the incident beam (fig. 4.13).

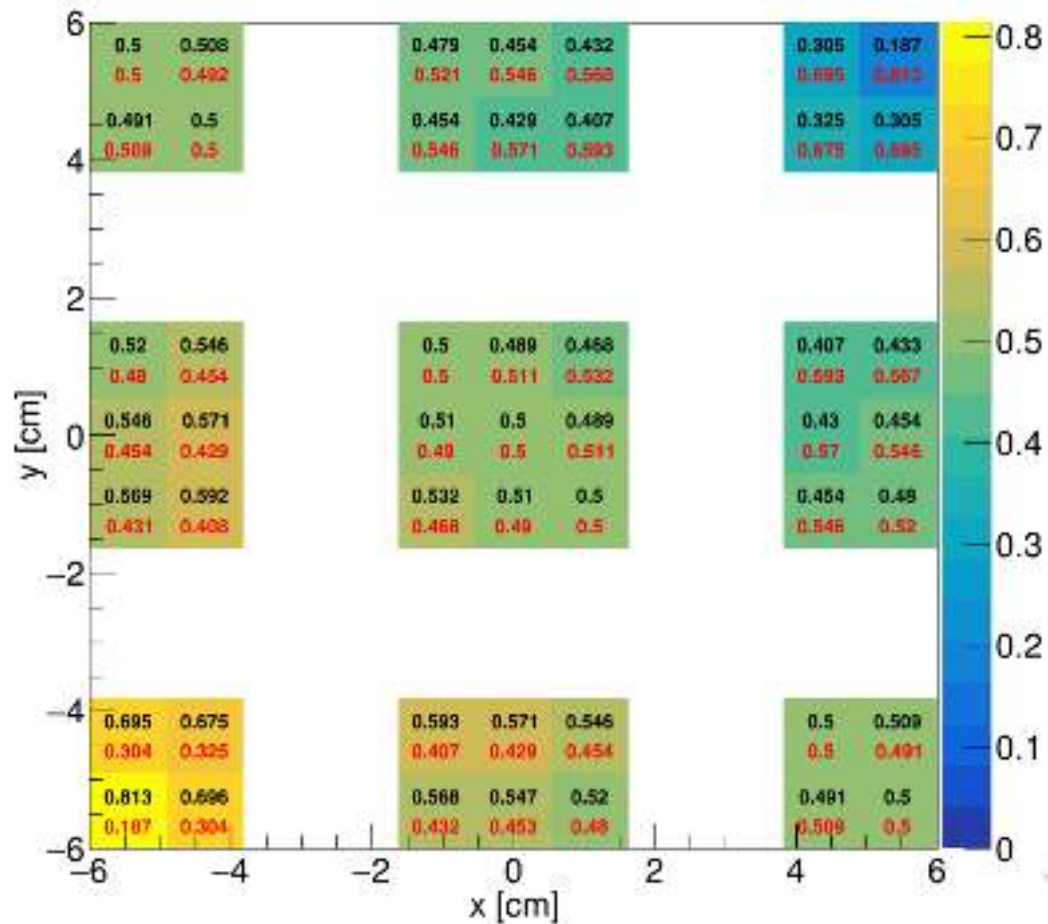


FIGURE 4.13: 2-D representation of a calorimeter plane surface for a simulated 50 MeV perpendicular electron. Number of photons arrived at the PMT placed at the top-right corner (in red) and at the bottom-left corner (in black), normalized to the sum of them. The colored palette is referred to black numbers.

Nevertheless, beam data analysis and MC simulations in beam test configuration showed that the collected light is position-independent in a very large central region of the scintillator plane. Regarding the tower calorimeter, data acquired in central positions have been used for energy calibration.

Once the PMT signals have been pedestal-subtracted and equalized, an offline event selection is applied:

- the most significant trigger paddle hit and the 1st and 2nd planes hit (all PMTs over 10 standard deviations); a standard deviation is defined as in Eq. 4.5;
- trigger multiplicity equal to 1 (all PMTs not belonging to the most significant paddle under 5 standard deviations);
- no hit in any veto (both PMTs under 5 standard deviations);
- plane multiplicity equal to the number of planes hit (a plane is hit if both PMTs have a signal over 10 standard deviations).

This selection removes multiple particles events, asks for the lateral containment of the particle in order to avoid energy leakage and requires a minimum number of "hit planes" to reject events with anomalous low energy loss (large scattering for electrons or nuclear interaction for protons).

For each "hit plane" the signal of the plane is calculated as the sum of the 2 PMT signals, and finally the total signal released in the tower calorimeter is the sum of the signals released in the "hit planes". For each energy beam, the ADC distribution of the tower calorimeter total signal is then fitted with a Gaussian function providing a mean ADC value and sigma.

MC simulations are used to evaluate the expected energy deposition in the tower calorimeter. The events are selected with the following cuts:

- the most significant trigger paddle hit (deposited energy higher than 0.2 MeV) and the 1st and 2nd planes hit (deposited energy higher than 0.4 MeV);
- trigger multiplicity equal to 1 (deposited energy in the other five paddles lower than 0.2 MeV);
- no hit in any veto (deposited energy in veto plane lower than 0.2 MeV);
- plane multiplicity equal to the number of planes hit (a plane is hit if the deposited energy is higher than 0.4 MeV).

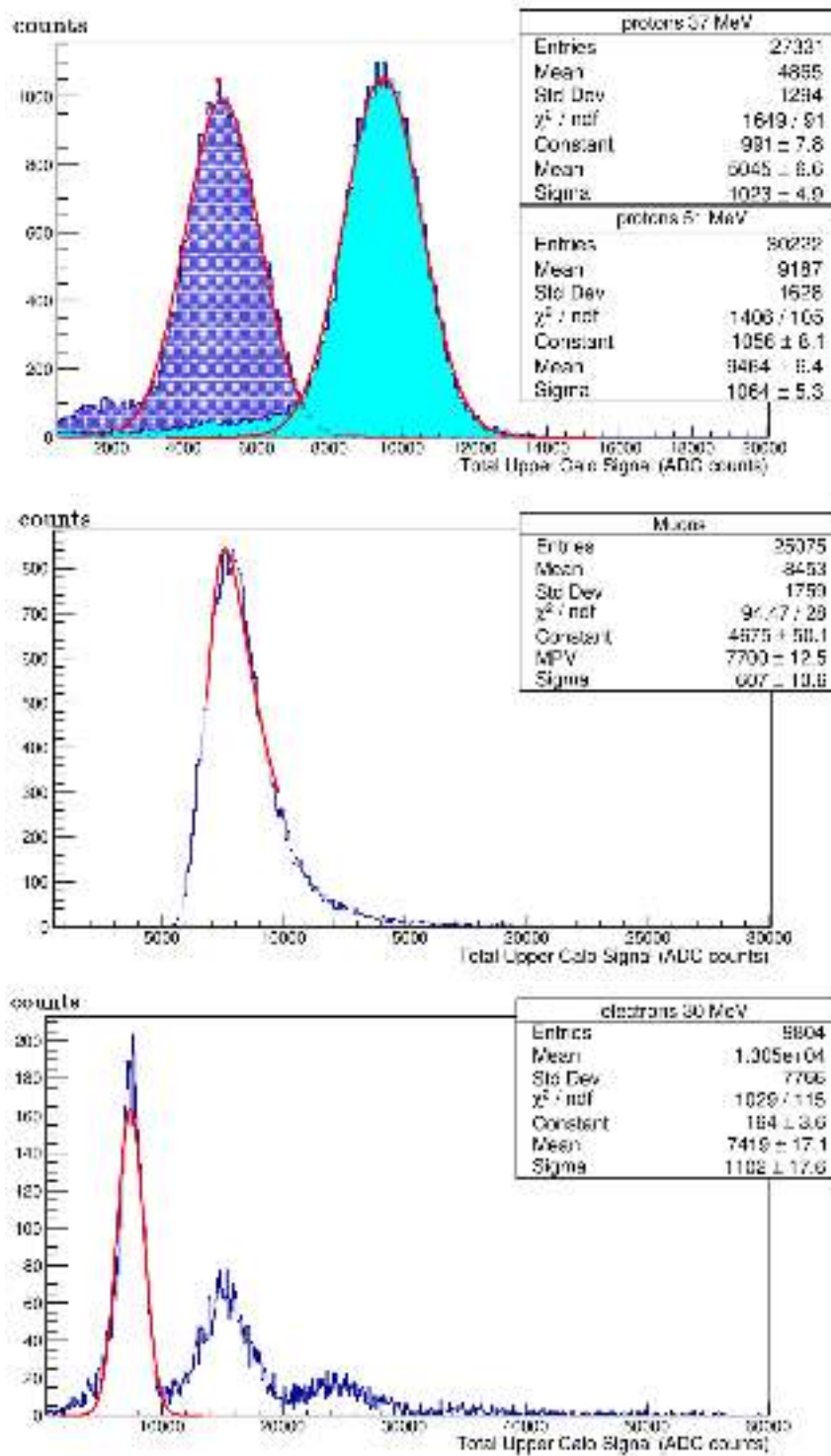


FIGURE 4.14: Tower calorimeter total signal distribution for HOT side in: (top) 37 and 51 MeV proton beams (blue-cyan); (center) atmospheric muons; (bottom) 30 MeV electron beam.

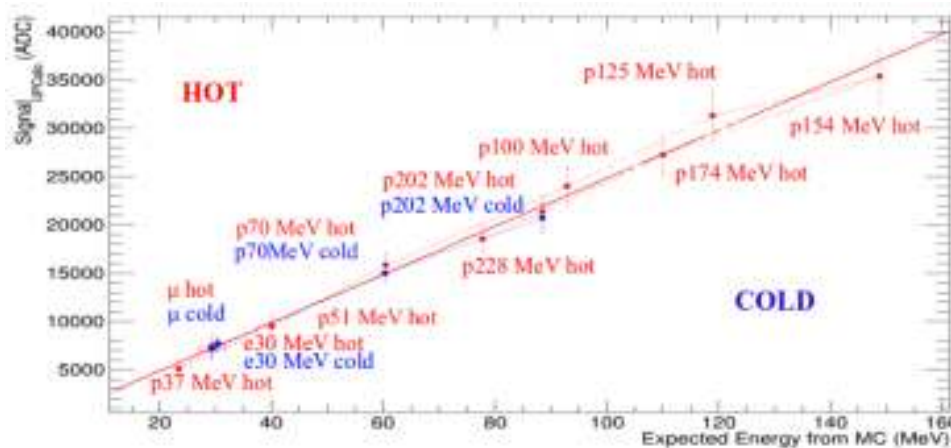


FIGURE 4.15: ADC signal peak to expected energy deposition (in MeV) obtained with MC simulation, providing the ADC/MeV conversion factor for tower calorimeter. Red/blue points refer to data acquired with the HOT/COLD side of the HEPD electronics. For energies of 174, 202 and 228 MeV protons are not contained in the tower calorimeter (they are stopped in the LYSO plane), and the deposited energy is smaller.

The values of 0.2 and 0.4 MeV reported in the cuts correspond to the deposited energy of 1/4 of a MIP in a trigger paddle and in a calorimeter plane respectively. The distributions of energy deposit in each calorimeter plane obtained with these selections are then fitted with a Gauss curve.

Fig. 4.14 shows the ADC signal distribution for proton beams of energy 37 and 51 MeV, atmospheric muons and 30 MeV electron beam. For electrons, the three peaks corresponding to beam bunches with 1, 2 and 3 electron multiplicity are visible; only multiplicity equal to 1 is considered in the analysis.

The conversion factor ADC/MeV, that is the energy response function of the tower calorimeter, is finally obtained fitting the ADC signal peak to the expected energy deposition (in MeV) obtained with MC simulation. The obtained calibration curve, used for the energy reconstruction deposited in the HEPD tower calorimeter is shown in fig. 4.15; red/blue points refer to data acquired with the HOT/COLD side of the HEPD electronics. It must be remarked here that, after the equalization procedure, the ADC signals from HOT and COLD side coincide.

To calibrate LYSO calorimeter, the beam energies higher than 150 MeV for protons and 45 MeV for electrons were used, in order to have signal on the LYSO crystals. As for the tower calorimeter, once the PMT signals have been pedestal-subtracted and equalized, an offline event selection is applied on the basis of each PMT signal-to-noise ratio; the same offline event selection was applied with the additional request that the number of hit planes is 16 as

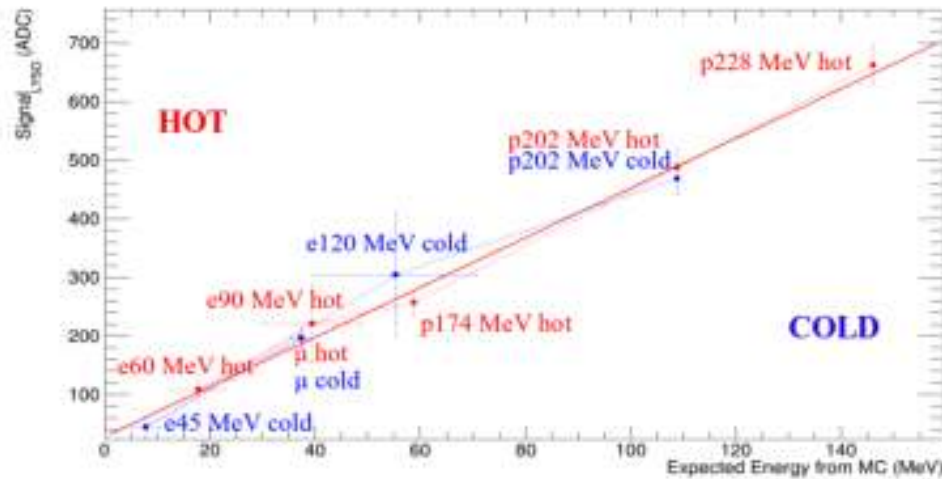


FIGURE 4.16: ADC signal peak to expected energy deposition (in MeV) obtained with MC simulation, providing the ADC/MeV conversion factor for LYSO calorimeter. Red/blue points refer to data acquired with the HOT/COLD side of the HEPD electronics.

the particle must cross the entire tower calorimeter to reach the LYSO plane.

The LYSO plane signal was then calculated as the sum of all LYSO crystals with PMT over threshold. The obtained ADC distribution of the LYSO plane total signal is then fitted with a Gaussian function providing a mean ADC value and sigma, to be compared with the expected energy deposition in the LYSO plane obtained with MC simulation. As for the tower calorimeter, the LYSO energy response function is finally obtained fitting the ADC signal peak to the expected energy deposition (in MeV) obtained with MC simulation. The obtained calibration curve is shown in fig. 4.16; red/blue points refer to data acquired with the HOT/COLD side of the HEPD electronics (Ambrosi, G. et al., 2019).

4.4 Range energy reconstruction

A method for a cross-check of the energy reconstruction exploits the calorimeter granularity; it is based on the range information of the particle, obtained by considering the segmented structure of the calorimeter and using the information of the deeper plane with a signal higher than a threshold.

A MC simulation was appositely set up to determine the energy mean value and the variability associated to events stopping in each plane. 1 million of protons and 1 million of electrons were generated with uniform energy spectra, between 1 and 100 MeV and 1 and 300 MeV respectively, and

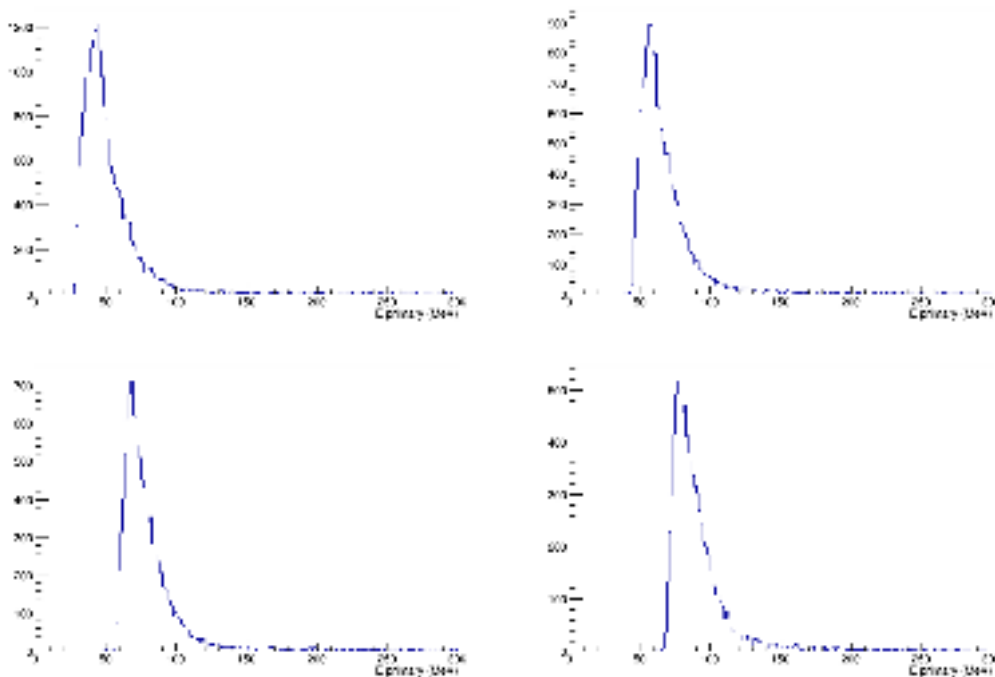


FIGURE 4.17: Distributions of the primary energy of events that stopped in the first (top left), second (top right), third (bottom left) and fourth (bottom right) plane of the tower calorimeter.

angular distribution uniform in $\cos^2\theta$ and ϕ in both cases; the events were generated from a rectangular plane surface of $22 \times 24 \text{ cm}^2$. The last plane hit by the event was defined as the deepest plane with a signal higher than a threshold (0.4 MeV, corresponding to 1/4 of the MIP release in a plane) and with a progressive plane number equal to the plane multiplicity of the event to reject energies with anomalous energy loss (nuclear interactions).

Fig. 4.17 shows the distributions of the primary energy of events stopped in the first planes of the tower calorimeter, estimated by the MC simulation.

The mean energy value and the relative error were then calculated plane by plane. The mean energy value was estimated as the maximum of the distribution. The uncertainty on energy was calculated as the absolute value of the difference between the above-mentioned mean value and the value of the first (left error) or the last (right error) bin over a threshold; the threshold was chosen to be the bin content of the maximum bin in the distribution, divided by 2. Fig. 4.18 shows the mean value of the primary energy for protons stopped in the i -th plane as a function of the stopping plane; for example, the plot shows that vertical protons with energy of 100 MeV stops on average in the 6th and 7th plane of the calorimeter.

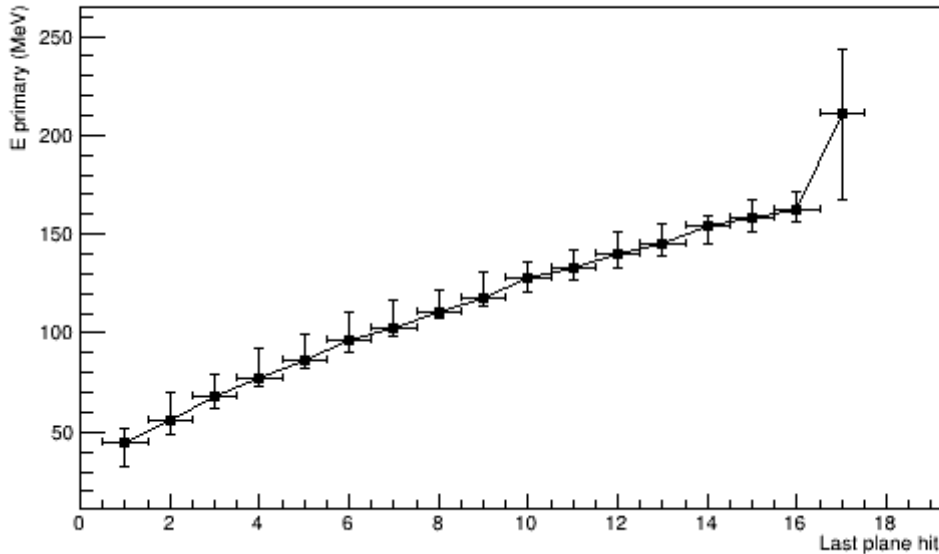


FIGURE 4.18: Curve of the primary energy as a function of the last plane hit by a proton; the plane thickness is 1 cm. The 17th plane represents the LYSO plane: its higher uncertainty is related to its higher thickness.

The last point of the plot, corresponding to a last plane value of 17, represents the plane of LYSO matrix. The reason of the discontinuity of the curve is due to the discontinuity of the materials (from the plastic scintillator of tower planes to the LYSO crystal of the matrix). The higher uncertainty of this point is related to the higher thickness of LYSO cubes.

Due to the large thickness of the scintillator planes (1 cm) it is clear that this method alone cannot be a solid basis for the energy determination of the event; the resolution of the measurement, depending on the single-plane thickness, is in general higher than that obtained with standard calibration.

The method has other restrictions. First of all, it can only be applied to protons; because of the different physics that handles electromagnetic processes, monoenergetic electrons don't have a single stopping plane (see Fig. 4.19 for an example). Moreover, the method can handle only events contained in the tower calorimeter; an event reaching LYSO plane cannot be treated in this way because of the further indivisibility along vertical axis of this sub-detector. For these reasons, the technique was mainly used as a cross-check for the protons energy reconstruction.

A cross-check study with beam test was performed. Fig. 4.20 shows the result of the comparison of this method with the effectively last plane hit by events in beam test: for example, in the 125 MeV protons beam test events

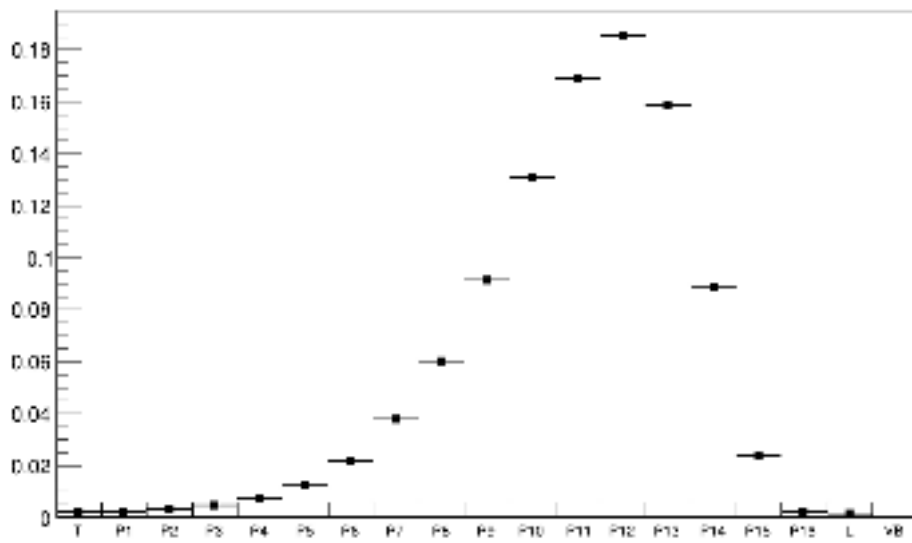


FIGURE 4.19: Percentage of events stopping in a plane as function of plane number for simulated 30 MeV electrons.

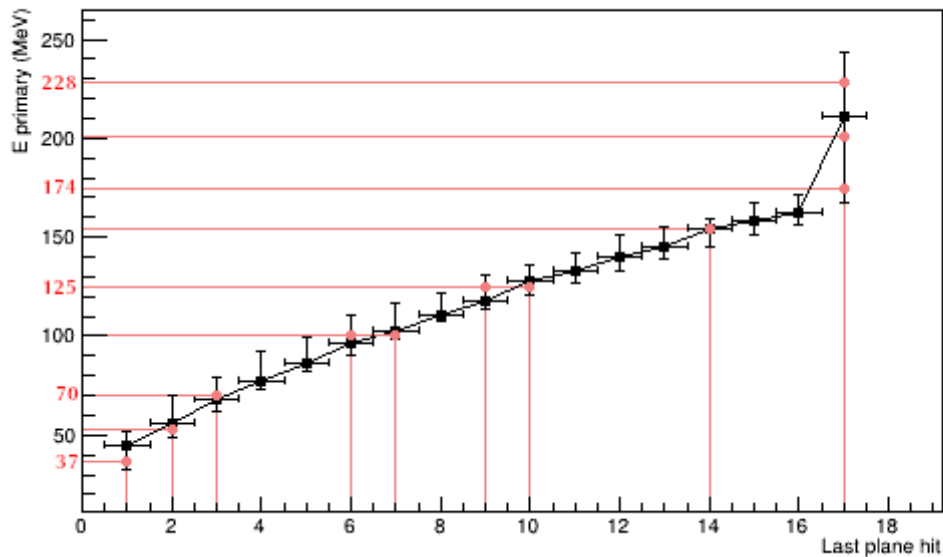


FIGURE 4.20: Real stopping planes for all proton test beam energies (red), compared with the range curve (black). The energies with two points indicates that a considerable percentage of events stopped in one or the other plane.

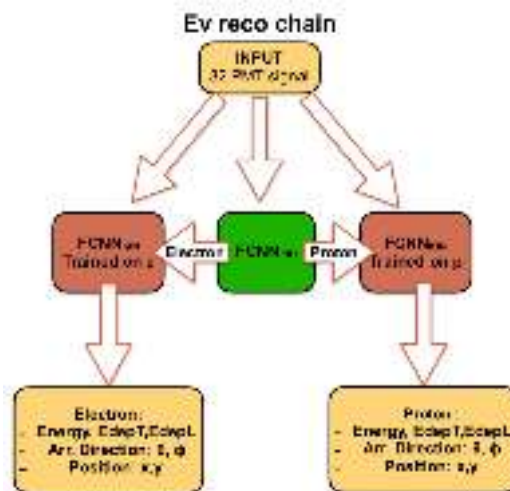


FIGURE 4.21: The HEPD Neural Network general scheme. After the particle identification, the event reconstruction chain uses the corresponding FCNN for energy and angle evaluation.

stop in the 9th and 10th plane, which behaviour is confirmed by the curve in Fig. 4.20.

4.5 Machine learning reconstruction

The reconstruction of the energy associated to the event was also based on a neural network appositely built up for the HEPD experiment and actually under development.

A Neural Network (NN, or Artificial Neural Network, ANN) is a computing system able to learn to perform tasks by considering examples, generally without being programmed with task-specific rules (the "model-free" learning). A NN is based on a collection of connected units, or nodes; each connection can transmit a signal to other connections. Connections typically have a weight that adjusts as learning processes: the value of the weight is updated at each step. The approach of these systems is of the type "trial & error": the algorithm learns and at the same time converges towards the best solutions. The so-called supervised learning doesn't require a model to be followed in the organization of data, but a training set is needed by the NN to learn which output is associated to some specific input.

In particular, the network used for our purpose is composed by two neural networks of the type Fully-Connected (FCNN), one trained on electrons and the other on protons (Fig. 4.21). It takes in input the ADC signal of the

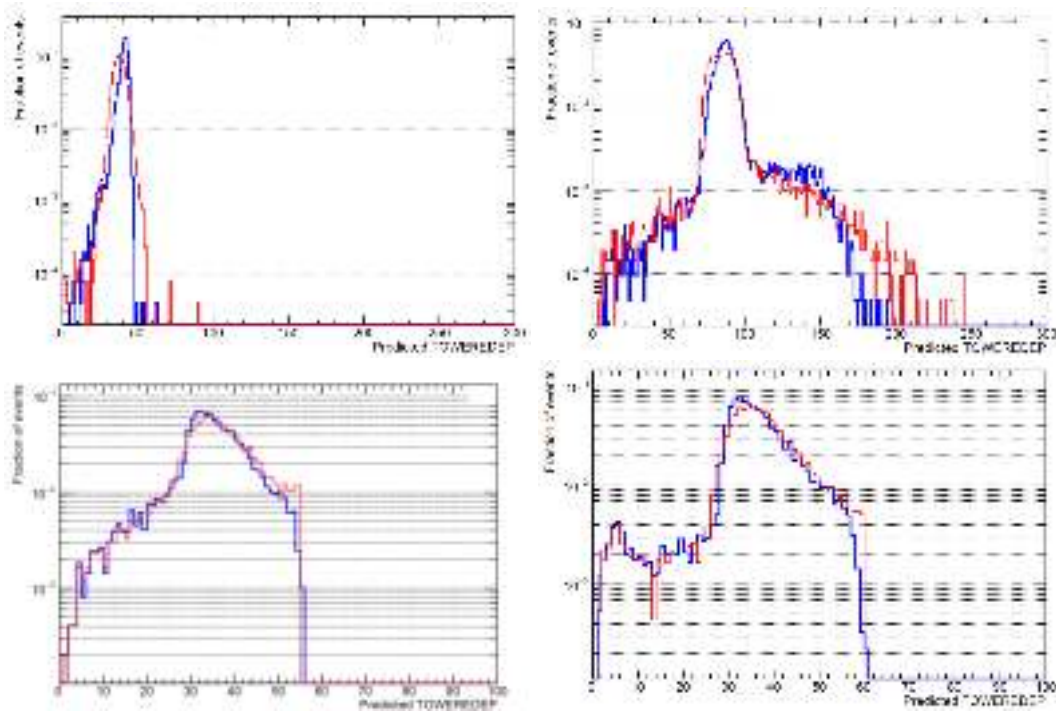


FIGURE 4.22: Distributions of energy deposited (in MeV) in the tower calorimeter, reconstructed with standard calibration (red) and neural network (blue), in simulated beam test of 51 MeV protons (top left), 202 MeV protons (top right), 45 MeV electrons (bottom left), 90 MeV electrons (bottom right).

PMTs of the tower and LYSO calorimeter and retrieves the primary energy of the event, its deposited energy, particle type and direction. The neural network was trained on a sample of digitized MC of electrons and protons and tested on an independent sample and on beam test runs. Fig. 4.22 shows the distributions of energy deposited in the tower calorimeter, obtained with the standard calibration and the network reconstruction, in several simulated beam test. The peak and width of proton distributions are well reproduced, even if in some cases (for events with a very large release), the agreement is still not excellent. In the case of electrons, the agreement is very good; 90 MeV electron distributions are not centered at 90 MeV because these events are not contained in the tower and release some energy also in the LYSO plane.

Further studies are being developed for comparison with energy value reconstructed from calibration and with particle identification from dE/dX vs E .

Chapter 5

Flux measurement

As described in chapter 3, one of the scientific goals of HEPD is the measurement of the particle fluxes for different cosmic ray populations. In this chapter the calculation of galactic proton flux will be discussed in detail.

Galactic particles (or GCR, Galactic Cosmic Rays) are high-energy charged particles originating outside the solar system. They are composed of protons, electrons and fully ionized nuclei. The flux of GCR ions is continuous and isotropic. Although the flux is a few particles per cm^2s^{-1} , GCRs include energetic heavy ions which can deposit significant amount of energy in sensitive volumes and so cause problems to spacecrafts electronics and humans in space. As for solar particles, the Earth's magnetic field provides a varying degree of geomagnetic shielding of near-Earth location from these particles. The flux of GCR becomes modulated in anti-correlation with solar activity due to solar wind.

Several models predict fluxes for electrons, protons and $Z=2$ to 92 nuclei in the near-Earth space beyond the Earth's magnetosphere. Some of the most important theoretical and experiment-driven trends are ISO-15390 model, CREME models, Nymmik (R.A. Nymmik et al., 1996), HelMod (Boschini M.J. et al., 2019).

The chapter explains in detail the calculation chain of galactic proton flux in three half-yearly periods during HEPD lifetime. Each section describes a step required to the flux calculation: event selection, efficiency, unfolding, galactic selection, live time; a particular importance was given to the selection of proton identification and its efficiency evaluated by MC analysis.

5.1 Event selections

Galactic proton flux Φ as function of kinetic energy E is evaluated using the following formula:

$$\Phi(E) = \frac{N(E)}{\epsilon(E) \times GF(E) \times LT \times \Delta E} \quad (5.1)$$

where $N(E)$ is the unfolded count distribution, $\epsilon(E)$ the energy efficiencies (planes and veto efficiency and particle identification), $GF(E)$ the geometrical factor (discussed in par. 4.1.3), LT the live time and ΔE the width of energy interval.

For flux calculation, a clean sample of particles must be selected, starting from the set of all events triggered by the detector. In fact, not all triggered events are good for the analysis: several types of events that could contaminate the sample are studied in order to find a cut and exclude them from the sample.

Among the events rejected in the analysis, a particular group is composed by events escaping from the calorimeter without releasing all their energy inside it. In this case, the event necessarily hits one veto plane or more: as explained in Chapter 3, the veto panels signal is necessary for a precise energy evaluation of the event.

Another set of events is made by those that produce secondary particles in the materials of the detector encountered by the primary before the trigger plane (the satellite wall, the honeycomb window and the silicon planes); in this case, the trigger paddles with a signal over threshold can be more than 1. In the signature of these events, the veto panels could or could not be hit depending on interaction point, type of particle and dynamic of the event (scattering angle and direction of secondaries); to reject these events in the analysis, a selection on trigger multiplicity is used (trigger multiplicity set to 1).

Other events produce secondary particles inside the calorimeter; some of these secondaries are not charged (photons or neutrons), can cross some scintillator planes and interact again in the detector. Then, the longitudinal profile for these events presents gaps (planes with no released signal). Fig. 5.1 shows two examples of these events. Also in this case, the veto panels could or could not be hit; they can be removed with the request of continuity in the calorimeter.

Considering the above-mentioned types of events, a good sample of events for flux calculation is selected using different cuts to exclude all undesired effects. The selection cuts for the proton sample are reported below:

- the same selection used by the trigger software is imposed; it corresponds, for the period considered, to signals over the threshold of $MIP/4$ in the trigger paddles and in the first two planes of the calorimeter; this selection is applied to have a more tighten cut with respect to the trigger online thresholds;

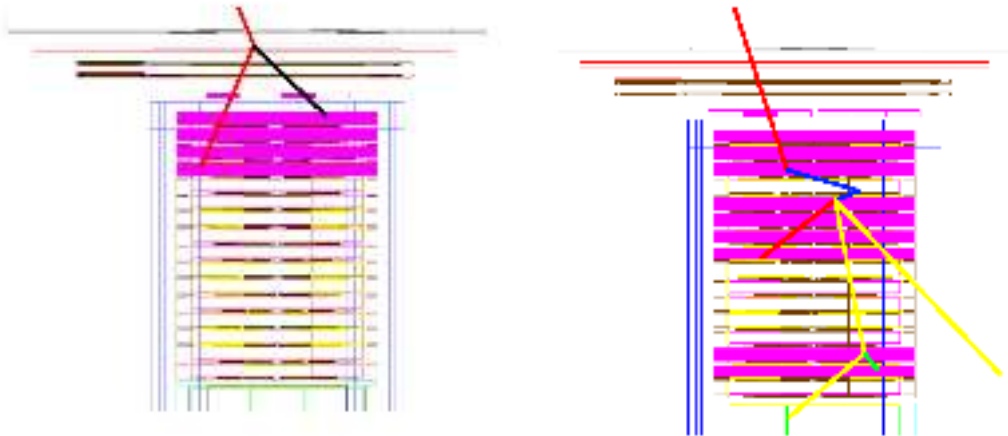


FIGURE 5.1: Two examples of events to be rejected from the analysis sample. Particle tracked are protons (red), neutrons (blue), photons (yellow), electrons (green) and He nuclei (black).

- only events with trigger multiplicity equal to 1 are selected (all PMTs not belonging to the most significant paddle under the threshold of $MIP/4$);
- only events with no signal on any veto plane (lateral and bottom) are selected (both PMTs under the threshold of $MIP/4$);
- the event signals in the calorimeter must have continuity through planes (i.e. the number of planes with a signal above threshold $MIP/4$ must be equal to the last plane number with a signal above threshold $MIP/4$).

5.1.1 Particle type selection

Protons and electrons can be discriminated in the detector by the dE/dX vs E method, by its longitudinal profile and by the NN reconstruction based on PMT signals.

The Bethe formula describes the mean energy loss per distance travelled by heavy charged particles (like protons) traversing matter. For lighter particles, like electrons, the energy loss is slightly different due to their small mass, their indistinguishability and the fact that they suffer much larger losses by Bremsstrahlung effect. In any case, the Bethe formula is largely known and used to correctly discriminate protons and electrons.

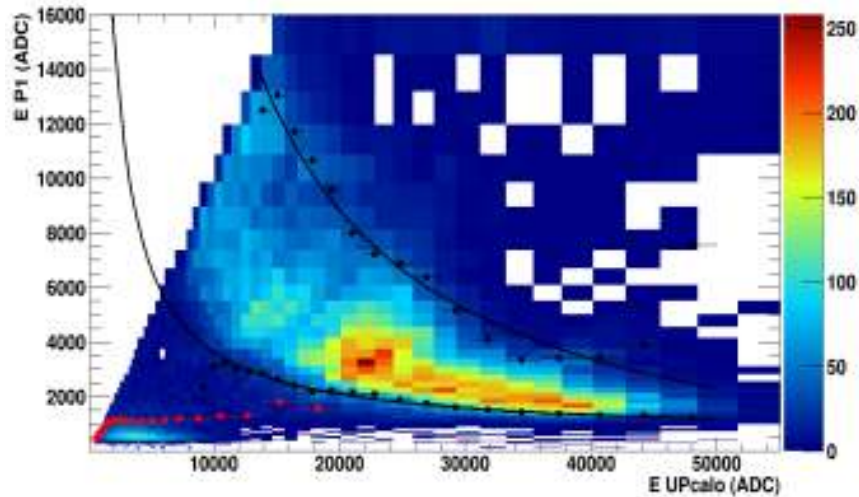


FIGURE 5.2: ADC signal sum of the 2 PMTs of the first plane as function of the ADC signal sum of all planes of calorimeter using a digitized MC simulation. Quantiles at 90% for electrons and at 5% and 95% for protons are also reported, respectively in red and black, with a $1/x$ function fit for proton ones.

The MC reconstruction gives the result already seen in last Chapter (fig. 4.7): the energy loss in the first plane of the tracker is function of the total energy deposit, selecting events in trigger (T&P1&P2) and veto-contained. The two populations are clearly distinguishable.

The digitized version of the same MC gives the result shown in fig. 5.2: the ADC signal sum of the 2 PMTs of the first calorimeter plane is function of the ADC signal sum of all planes of tower calorimeter. Selections applied to the sample are:

- offline trigger (one trigger paddle, P1 and P2 with standard deviation over 10, PMT in AND); standard deviation is defined as in Eq. 4.5;
- lateral and bottom veto (no plane with energy deposit higher than 0.2 MeV, corresponding to 1/4 of the MIP release in a veto plane);
- lyso veto (no crystal with energy deposit higher than 8 MeV, corresponding to 1/4 of the MIP release in a LYSO block);
- no plane discontinuity (last plane with standard deviation over 10 equal to plane multiplicity).

The regions where electrons and protons respectively are used to place themselves can be seen by beam test results; in fig. 5.3, the top panel shows the sum of ADC signals acquired by the two PMTs of first plane as function of the energy of the event; both bottom panels show where beam tests ADC

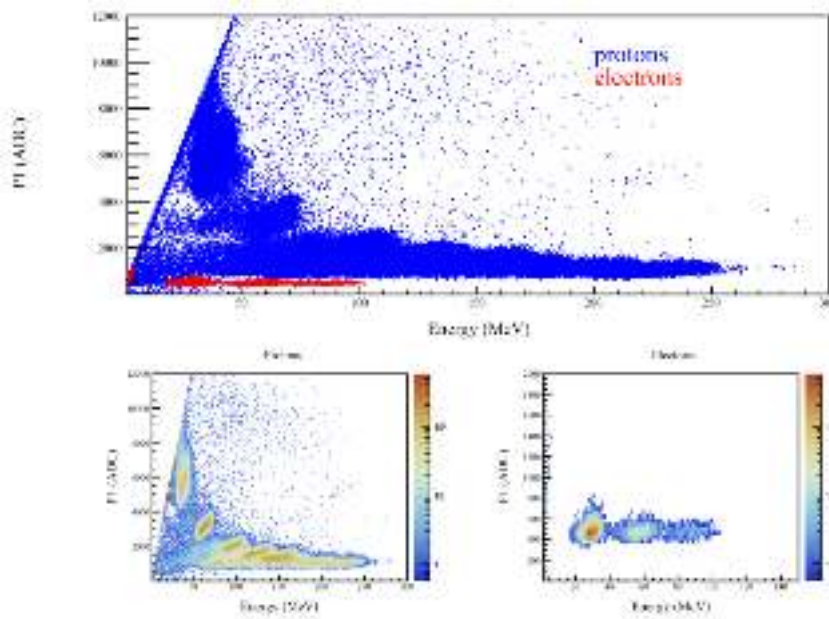


FIGURE 5.3: Signal deposited by protons (bottom left panel) and electrons (bottom right panel) beam tests in the first plane of tower calorimeter as a function of their total reconstructed energy. The two particle species populate different regions of the dE/dX vs E plane (top panel).

signal of protons and electrons lay as function of their estimated energy and the sum of ADC signals acquired by the two PMTs of the 1st plane of the scintillator tower, while top panel shows both populations in the same plot. Protons present the typical Bethe shape; electrons show a MIP release not dependent on total energy. The sub-populations visible in the two bottom panels are due to the various energies tested with proton and electron beams.

Protons and electrons have also different longitudinal profiles inside the calorimeter; the former present a typical rising shape followed by an abrupt decay of the signal (Bragg peak), while the latter show a uniform profile with no larger release in energy. This can be seen in fig. 5.4 and 5.5, where respectively two beam test events (a 125 MeV proton and a 30 MeV electron) are shown using an event-viewer software (Ambrosi, G. et al., 2019).

Particle discrimination was also studied using the neural network machine learning. Fig. 5.6 shows the distribution of the particle ID number assigned by the network for simulated protons and electrons. Based on the MC events, the network assigns a value of 0 for a perfect proton-like event and of 1 for a perfect electron-like event, intermediate values corresponding to non-perfectly associated events.

The distributions reveal also that a particle cut is possible using the NN

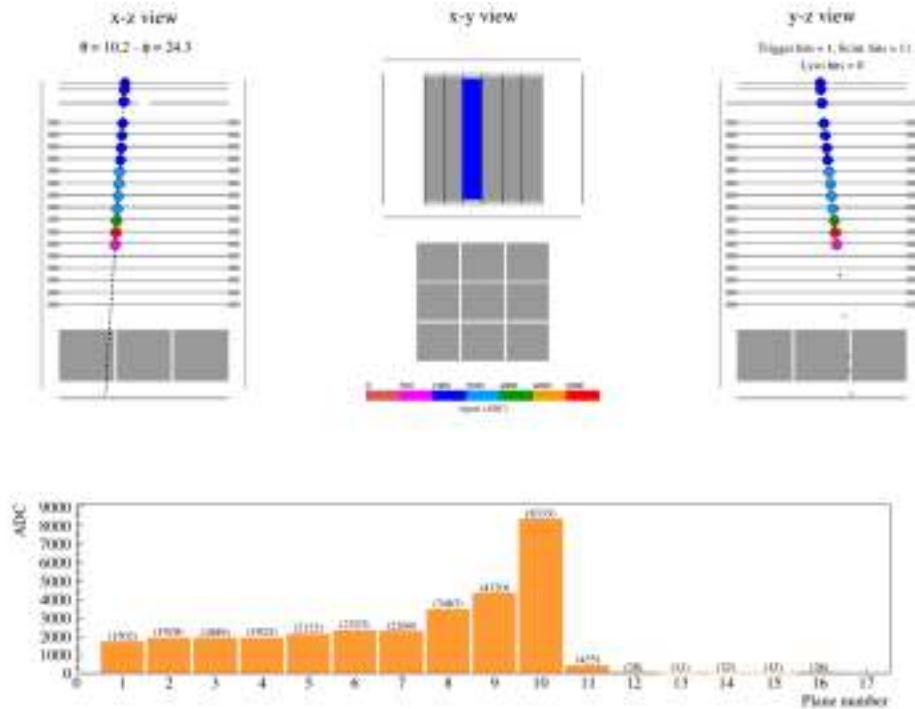


FIGURE 5.4: Longitudinal profile of a 125 MeV proton beam test event inside the scintillator tower. The Bragg peak is clearly visible at plane 10.

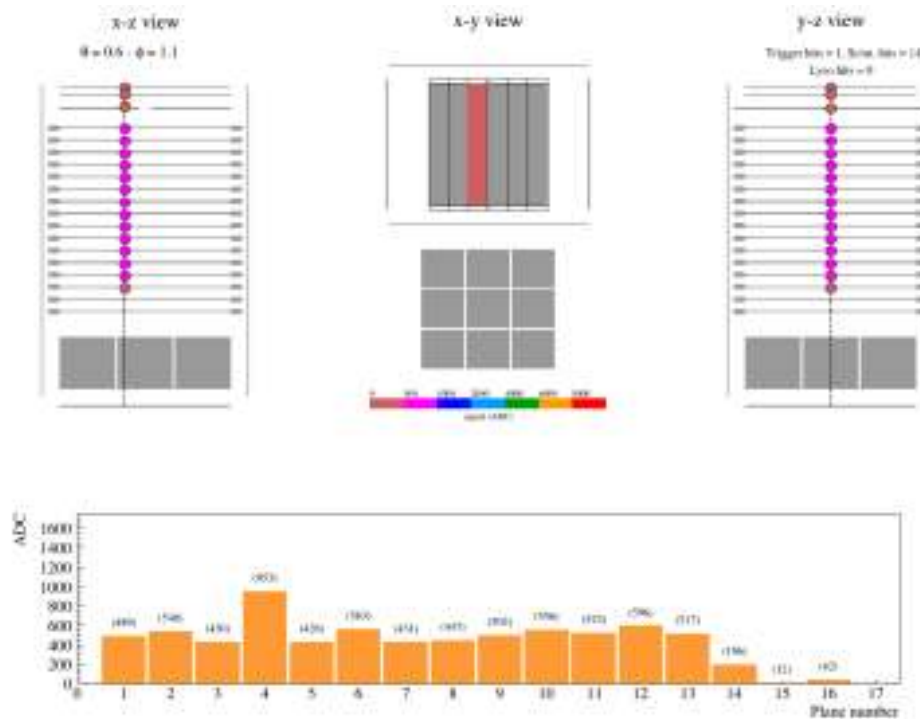


FIGURE 5.5: Longitudinal profile of a 30 MeV electron (beam test) inside the scintillator tower; the signal release is almost constant along the distance travelled by the particle.

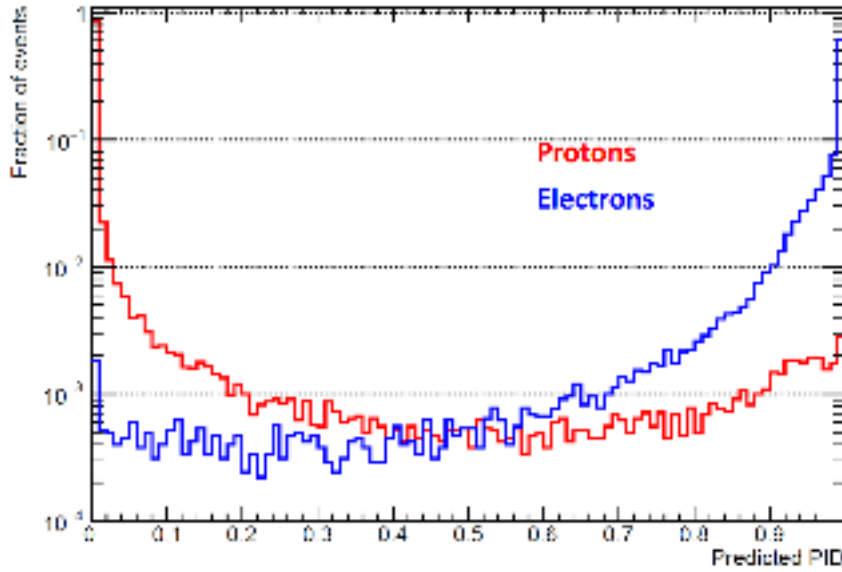


FIGURE 5.6: Particle ID number assigned by the neural network on a MC sample of electrons and protons. The NN assigns 0 to proton-like events and 1 to electron-like events.

parameter, given that the corresponding efficiency and contamination rate are calculated for the selection.

The discrimination between protons and electrons populations for the flux selection is realized using a double-curve selection (each curve has the form of $1/x$), required on the signal deposited on the first scintillator plane as function of the total deposited energy; these curves are estimated from a digitized MC like the plot in fig. 5.2. The band, delimited by the aforementioned curves (quantiles at 15% and 95% for lower and upper curves respectively), is large enough to collect $\simeq 80\%$ of the total proton population and to reject as many high-energy leptons as possible. The first plane signal distribution as function of the total energy lost in the calorimeter is shown in fig. 5.7; the red curve represents the 15% and 95% quantile threshold used to select the proton band.

5.2 Efficiencies

Two types of efficiencies are generally referred to when discussing radiation detection: the absolute efficiency and the intrinsic detection efficiency. The absolute or total efficiency ϵ_{tot} of a detector is defined as the fraction of events

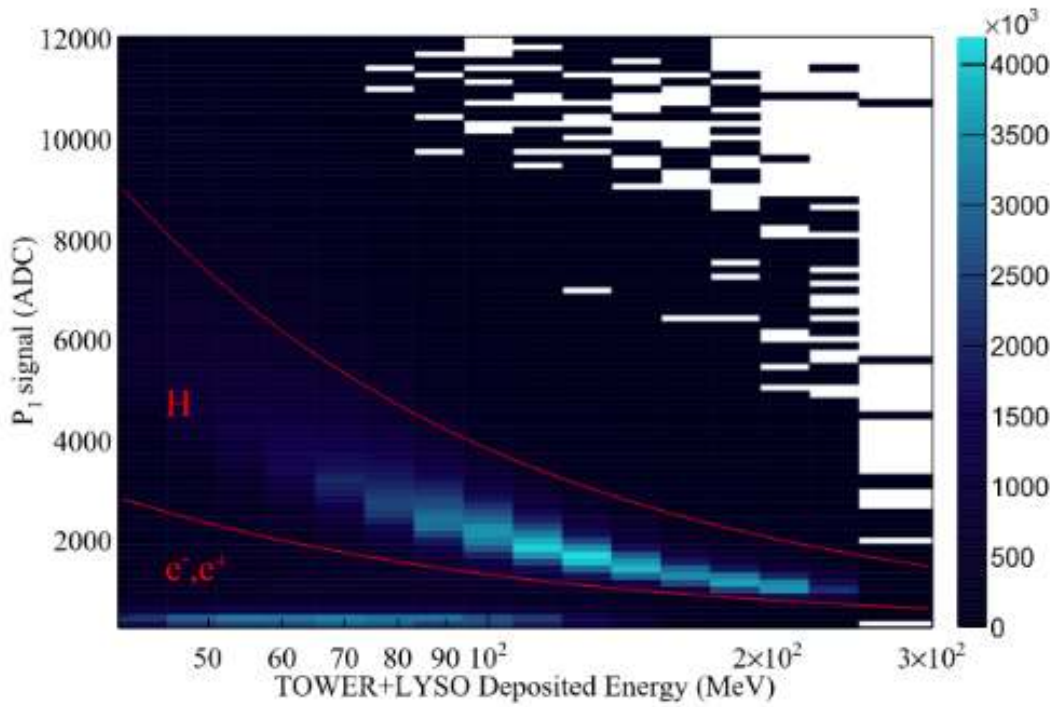


FIGURE 5.7: ADC signal sum of the 2 PMTs of the first plane as function of the total energy deposited inside the calorimeter for flight data. The red curves are $1/x$ function fits for quantiles at 15% and 95%.

emitted by the source which is actually registered by the detector:

$$\epsilon_{tot} = \frac{\text{events registered}}{\text{events emitted}} \quad (5.2)$$

This is a function of the detector geometry and the probability of an interaction in the detector; in most cases, the probability of interaction does not depend on geometry and the absolute efficiency can then be factored into two parts: the intrinsic efficiency ϵ_{int} and the geometrical efficiency or acceptance ϵ_{geom} . The absolute efficiency of the detector is then given by the product:

$$\epsilon_{tot} = \epsilon_{int} \cdot \epsilon_{geom} \quad (5.3)$$

The intrinsic efficiency is the fraction of events actually hitting the detector that are registered:

$$\epsilon_{int} = \frac{\text{events registered}}{\text{events impinging on detector}} \quad (5.4)$$

and the geometrical efficiency, in contrast, is the fraction of the source radiation which is geometrically intercepted by the detector:

$$\epsilon_{geom} = \frac{\text{events impinging on detector}}{\text{events emitted}} \quad (5.5)$$

In Eq. 5.1, the term $\epsilon(E)$ is intended to be the intrinsic efficiency of the detector; the geometrical efficiency is contained in the geometrical factor term, $GF(E)$, discussed in par. 4.1.3.

For each selection cut, an efficiency curve as function of the energy is required. The efficiency of a cut for a certain energy bin is defined as the ratio between the number of events passing the selection and the number of events in the bin. In table 5.1 the single plane efficiency is shown, estimated as:

$$\epsilon_{P_i} = \frac{T \& P_1 \& P_2 \& \dots \& P_{i-1} \& P_i \& P_{i+1} \& \dots \& P_{16} \& L}{T \& P_1 \& P_2 \& \dots \& P_{i-1} \& P_{i+1} \& \dots \& P_{16} \& L} \quad 1 \leq i \leq 16. \quad (5.6)$$

for a muon run acquisition; overall selection criteria consisted in single trigger multiplicity and lateral veto containment. The smaller value of P1 is related to a geometrical inefficiency due to the different surface extension of the trigger plane and the second calorimeter plane; a similar effect is present for P16 efficiency (different surface extension of P15 and LYSO plane).

The table clearly shows that the efficiency of a single plane in the HEPD calorimeter is approximately unitary, as expected by a typical scintillator slab. The calorimeter efficiency is defined as the product of the 16 single plane efficiencies.

Because of the lack of redundance in HEPD instruments, it is not possible to evaluate the proton efficiency with the experimental data. This makes the MC analysis, and in particular the digitization of MC events, of fundamental importance and widely used in efficiencies evaluation.

The efficiency for the proton identification was studied in detail applying the different cut types to a MC simulation; in this case, the efficiency is defined as the number of protons passing the identification selection divided by the number of protons per energy bin. The proton identification efficiency as function of the primary energy is obtained from the plot in fig. 5.2: for each bin in the plot, the number of protons with a P1 signal contained between the two black lines over the total number of protons is calculated; fig. 5.8 shows this fraction, after the conversion of each bin value from ADC signal to MeV using the standard calibration.

Plane	% efficiency
P1	90.497
P2	99.827
P3	99.961
P4	99.989
P5	99.986
P6	99.989
P7	99.989
P8	99.992
P9	99.984
P10	99.982
P11	99.969
P12	99.971
P13	99.955
P14	99.931
P15	99.914
P16	98.007

TABLE 5.1: Single plane efficiencies for the tower calorimeter for a muon run acquisition. The threshold for hit condition is MIP/4. Overall selection criteria are single trigger multiplicity and lateral veto containment.

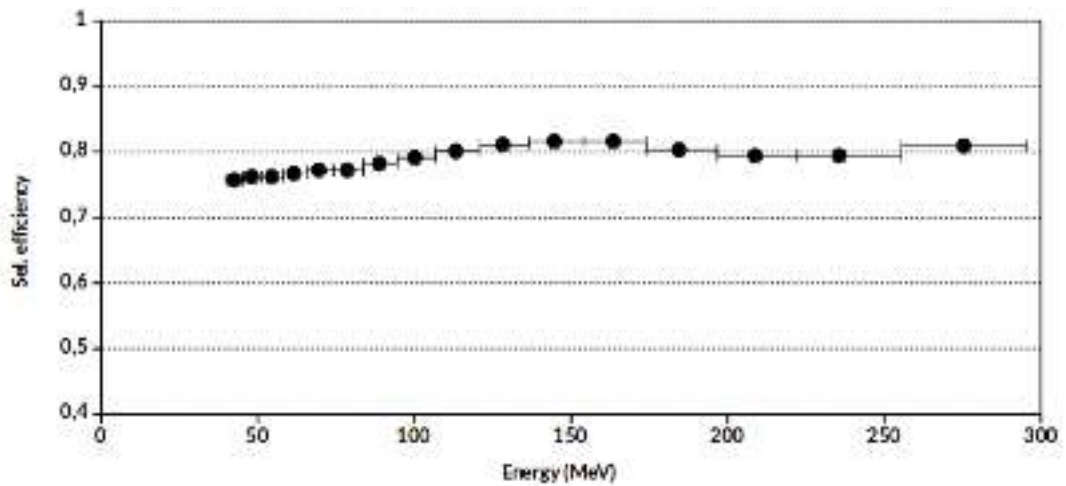


FIGURE 5.8: Proton identification efficiency as function of the primary energy obtained with a MC simulation.

5.3 Unfolding

The calorimeter reconstruct the energy that was deposited by the proton in the detector; in order to evaluate a proton flux, the goal is to reconstruct the energy of the primary, that is the energy of the particle before entering in the detector. A correction is needed for the proton energy spectrum measured in the whole calorimeter to take into account energy losses in tracker planes, trigger plane and passive materials, and to energy carried away by neutral secondaries. In particular, the correction was applied by means of an unfolding procedure, following the classical Bayesian approach proposed in (D'Agostini, 2010). The purpose of the unfolding is to find the "true" number of events in each energy bin, given the observed spectrum (i.e., the number of events measured in each energy bin) and assuming some knowledge about the physical laws which connect the cause with the effect (energy losses).

The Bayes' theorem is stated in terms of several independent cause (C_i , $i = 1, 2, \dots, n_C$), in our case the passage of particles of given energy, which can produce an observable response in the detector (measured energy) that is the effects (E_j , $j = 1, 2, \dots, n_E$). It is usually presented in the form:

$$P(C_i|E) = \frac{P(E_j|C_i)P_0(C_i)}{\sum_{l=1}^{n_C} P(E_j|C_l)P_0(C_l)} \quad (5.7)$$

The formula links the probability $P(C_i|E_j)$ that the single observed event E_j has been due to the cause C_i , to the probability $P(E_j|C_l)$ that the i -th cause produces the j -th effect, times the probability of the cause $P_0(C_i)$.

In the j -th energy bin, $n(E_j)$ events, the best estimate of the expected number of events assignable to each of the cause is

$$\hat{n}(C_i) = \frac{1}{\epsilon_i} \sum_{j=1}^{n_E} n(E_j)P(C_i|E_j), \epsilon_i \neq 0 \quad (5.8)$$

where ϵ_i is the efficiency of detecting the cause C_i in any of the observed effects and it is defined as:

$$\epsilon_i = \sum_{j=1}^{n_E} P(E_j|C_i) \quad (5.9)$$

Simulation suggests to use iteratively formula in eq. 5.8 in order to obtain the final $\hat{P}(C_i)$ as close as possible to the true one, being $\hat{P}(C_i) = n(C_i) / \sum_{i=1}^{n_C} \hat{n}(C_i)$.

The probabilities $P(E_j|C_i)$ can be estimated with Monte Carlo methods

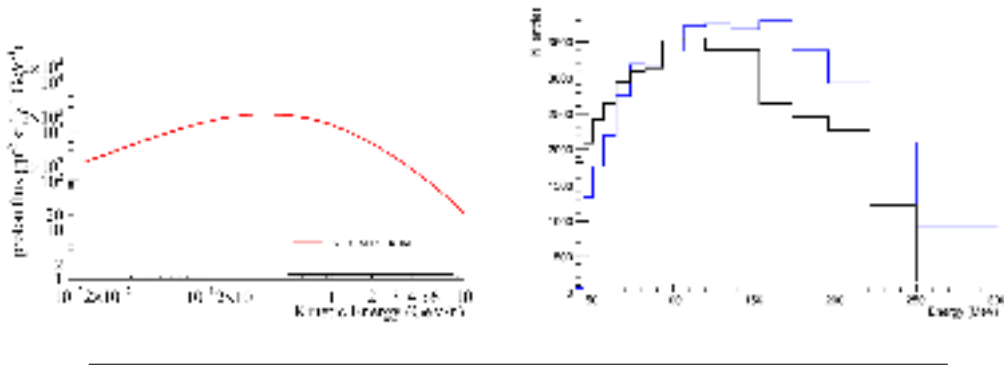


FIGURE 5.9: (Left) The input spectrum for unfolding test is a galactic cosmic proton HelMod spectrum; (right) unfolded distribution of deposited energy (blue) and folded distribution of true energy (black).

and constitute the elements of the smearing matrix, while an assumption has to be done about the initial probability $P_0(C)$. The iteration goes through the following steps:

1. choose the initial distribution $P_0(C)$ and evaluate the initial expected number of events $n_0(C_i) = P_0(C_i)N_{obs}$, where N_{obs} is the number of experimental observations;
2. calculate $\hat{n}(C)$ and $\hat{P}(C)$;
3. make a χ^2 comparison between $\hat{n}(C)$ and $n_0(C)$;
4. replace $P_0(C)$ by $\hat{P}(C)$ and $n_0(C)$ by $\hat{n}(C)$ and start again.

The iteration is stopped when the value of χ^2 is less than a fixed value.

In our case, Monte Carlo simulations were used to estimate the detector response and correctly reconstruct the energy spectrum; a dedicated algorithm was implemented to perform the unfolding and tested on a MC proton simulation with input energy spectrum from HelMod (fig 5.9).

Also, the unfolding procedure can correct the high-energy protons that hadronically interact in the detector. These events release a total signal very similar to the total signal released by an electron (approximately 1.4 times a typical MIP signal, while the electron behave like a MIP; see fig. 5.10); also the plane-by-plane signal of these events is very similar to that of electron events (fig. 5.12).

The MC simulation helped to explain this behaviour: these events represent a significant percentage of the total. The most part of them is classified to have interactions in the detector as elastic hit or proton, neutron and π inelastic interactions. It was also noted that a considerable fraction of events

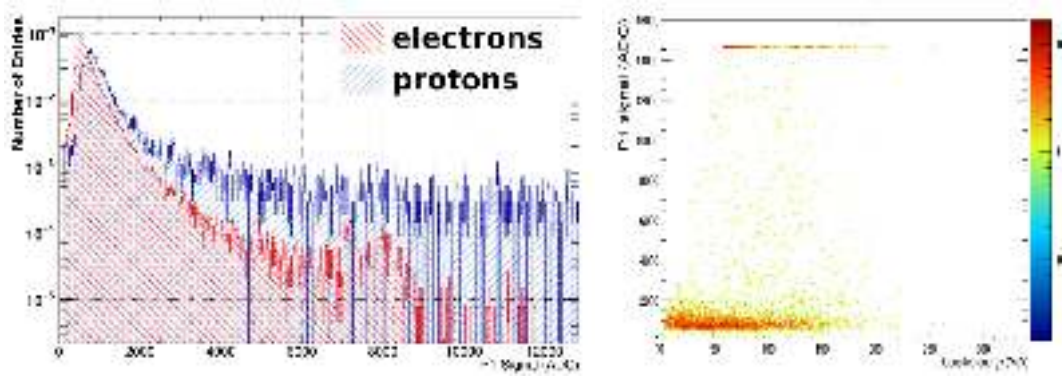


FIGURE 5.10: P1 signal distributions as single (left) and as function of total deposited signal (right) in a digitized MC for contained electrons and protons with a primary energy higher than 300 MeV; the peak values of P1 signals are respectively 529 and 744 ADC.

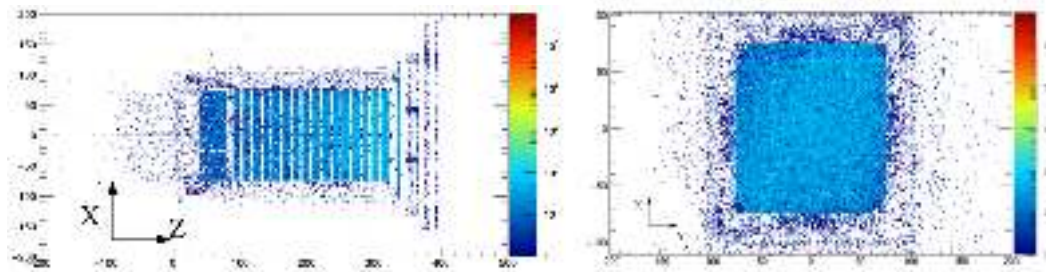


FIGURE 5.11: Lateral (left) and frontal view (right) of interaction point for simulated protons with a primary energy higher than 300 MeV. The colored z-axis contains the number of entries. Containment selection is required.

with primary energy higher than 300 MeV produce neutrons and photons as secondary particles and these carry out a significant fraction of the primary particle momentum, mimicking a low-energy proton. There is no preferred area for these interactions (fig. 5.11): a geometric cut would be useless to exclude these events.

The smearing matrix (fig. 5.13) was obtained from a dedicated MC proton simulation, with energies generated between 1 MeV and 10 GeV, with generation points randomly chosen in a square of $40 \times 40 \text{ cm}^2$ and at 1 cm from the satellite wall and angles randomized isotropically in $\cos^2\theta$ and ϕ . For the analysis, the same selections described in last paragraph were applied.

It should be stressed here that, on the contrary, the ML energy parameter does not need any unfolding correction, because the conversion is intrinsic in the neural network functioning. The network is trained to calculate both deposited and primary energy, so it already corrects the values with release of energy in passive structure, Bremsstrahlung and all the other possible effects

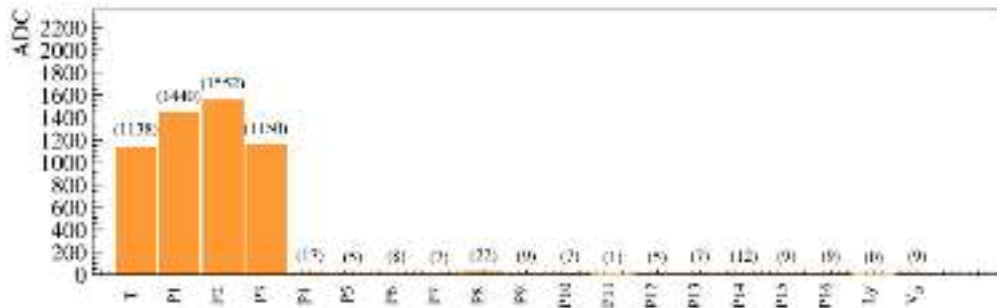


FIGURE 5.12: Longitudinal profile of an example of interacting proton from the 154 MeV beam test; the numbers in parenthesis are the ADC sum signals of the 2 plane PMTs. The typical Bragg shape is not present; the particle identification ML parameter of this event is 0.39.

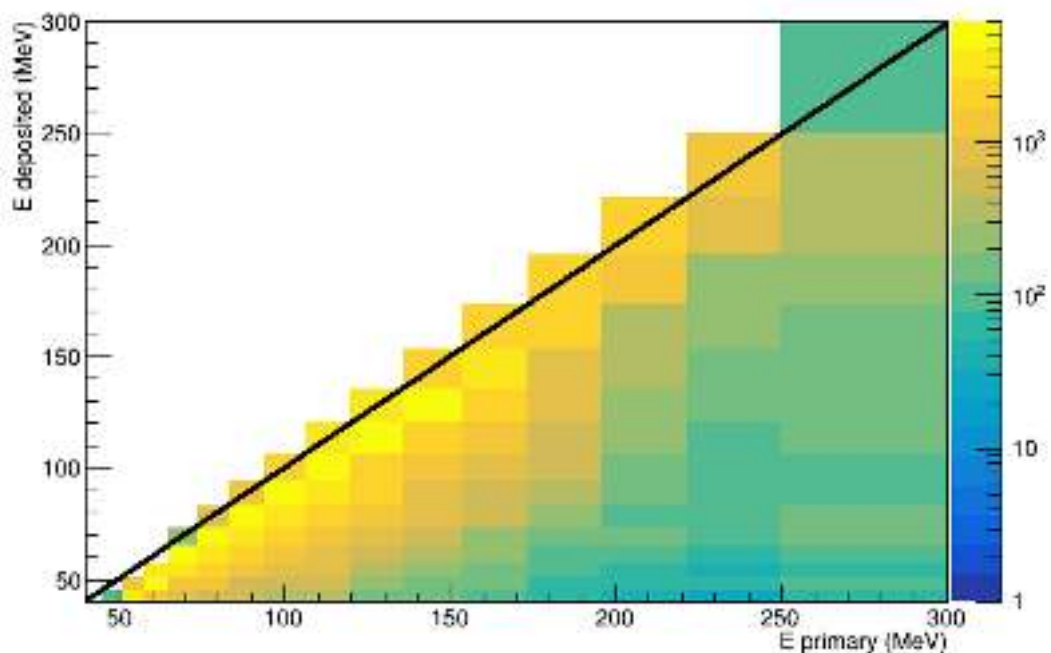


FIGURE 5.13: Scatter plot of deposited and primary energy for a sample of simulated protons in the range 1 MeV-10 GeV. The colored z-axis contains the number of entries. The black line represents the 1st and 3rd quadrants bisector $y = x$.

that lead to a loss of energy that is not measured.

5.4 Galactic selection

The ability of charged particles to penetrate into magnetosphere from outside is limited by the Earth's magnetic field. A particle's penetrating ability is determined uniquely by its rigidity (i.e. its momentum divided by its charge):

$$R = \frac{pc}{Ze} \quad (5.10)$$

For each point in the magnetosphere and for each direction of approach to that point, there exists a threshold value of rigidity, called the geomagnetic cutoff. Below this value, no charged particle can reach the specific point from the specific direction.

As the geomagnetic cutoff varies with the particle arrival direction, the geomagnetic cutoff is averaged over all arrival directions. For a given location and rigidity, the integrated solid angle from where particles with this rigidity can reach the location, divided by 4π , is called attenuation, or exposure, factor. For a given energy, the exposure time is defined as the total time that the orbit is in regions where the attenuation factor is non-zero.

Because of the highly inclination of the orbit of CSES, HEPD is able to trigger particles of various origin. To discriminate the primary (solar or galactic) component from the re-entrant albedo component, it is necessary to evaluate the local rigidity cutoff in each point of the satellite orbit. To this purpose, a combination of the IGRF model (E. Thèbault et al., 2015) and Tsyganenko89 model (N. A. Tsyganenko, 1989) is adopted for the magnetic field calculation to take into account both internal and external magnetic sources. A simulation in quite conditions on all possible arrival directions of protons has been carried out and, considering the HEPD field of view, a rigidity cutoff map in geographich coordinates has been realized (fig. 5.14).

In order to remove the majority of re-entrant protons, counts were selected in a geomagnetic cutoff slice between 0.26 and 0.35 GV. The conversion from rigidity to kinetic energy is performed via the following formula:

$$R = \frac{A}{Z} \sqrt{T^2 + 2TT_0} \quad (5.11)$$

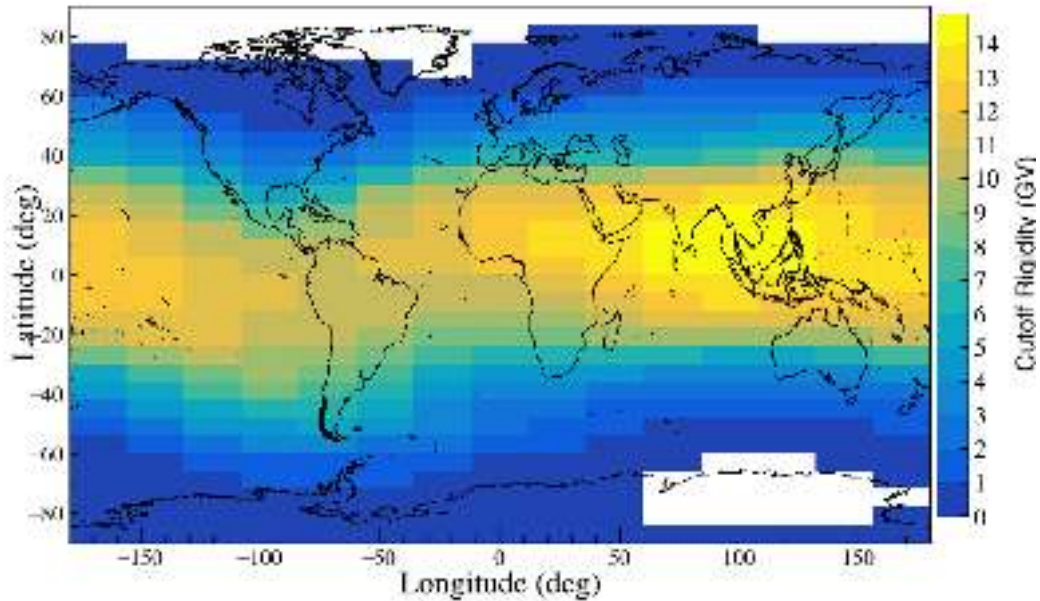


FIGURE 5.14: Cutoff map for HEPD field of view as function of geographic latitude and longitude point. The map is simulated using Tsyganenko89 model.

where R is the rigidity, A the mass number, Z the charge, T the kinetic energy per nucleon and T_0 the rest energy. The condition $R_{CO} > 0.26$ GV implies the exclusion of protons with energy lower than 40 MeV and of galactic electrons/positrons less energetic than 260 MeV from the sample of galactic events. It also assures all protons with energy higher than 40 MeV to be of galactic origin.

Another selection regards the exclusion from analysis of events detected in SAA region; in this analysis, the SAA region is defined as the area with a magnetic field value lower than 26000 nT.

5.5 Live time

The live time is the time during which the detector is capable to register a new trigger. It is in contrast with the dead time, i.e. the time required by the electronics of the apparatus to register and process each event. The total time of the event is the sum of live time and dead time.

Both instrumental live and dead time calculation are performed and managed by the trigger board; by means of counters for live and dead time are cross-checked with the on-board time of the CPU, measuring the acquisition time (sum of dead and live time), to remove possible systematic errors due to

the counting method. The related systematics is considered negligible with respect to the others.

Because of the rigidity cutoff discussed in par. 5.4, the detector is not capable to measure galactic particles during the whole live time window.

To be consistent with the geographical criteria introduced in last paragraph, the live time is accumulated only in regions where the rigidity cutoff is $0.26 \text{ GV} < R_{CO} < 0.35 \text{ GV}$.

5.6 Flux estimation

Summarizing, the different steps that lead to the flux estimation are in order:

- calculate, via Tsyganenko map, the corresponding rigidity cutoff value in the event lat-lon geographical point;
- exclude events triggered inside SAA region;
- exclude some types of events using selection cuts described in par. 5.1 (offline trigger, veto containment, trigger multiplicity, plane continuity);
- apply particle identification cut;
- select events in the geomagnetic cutoff slice defined in par. 5.4;
- using the smearing matrix, unfold the deposited-energy count distribution;
- accumulate live time in the corresponding lat-lon portion;
- divide the energy count distribution by geometrical factor, live time distribution and particle identification efficiency.

Sources of systematic uncertainties considered in the present estimation are to be searched in the deconvolution procedure, related to the intrinsic accuracy of the adopted unfolding technique, and in the comparison between data and Monte Carlo, i.e. the residual discrepancy between test beam and Monte Carlo data due to digitization procedure. The total systematics is the squared sum of the single evaluated systematics.

Three semiannual galactic proton spectra as function of energy between 40 and 250 MeV were obtained; the periods selected are between August 6th, 2018 and January 5, 2020. The HEPD fluxes are reported as black points in

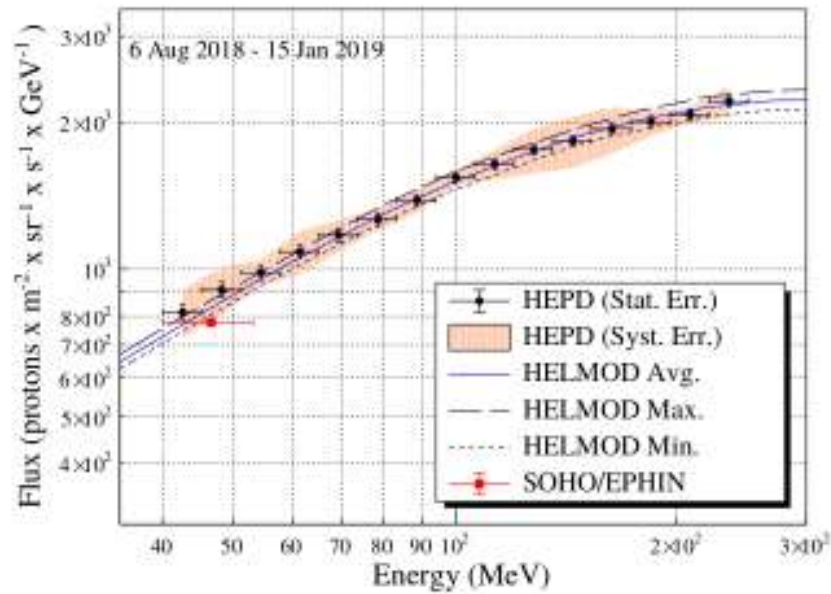


FIGURE 5.15: Galactic proton spectrum as function of energy in the period August 6, 2018 - January 15, 2019. Systematics uncertainties are present as a red shaded area. Also HelMod theoretical spectrum averaged over the corresponding period (blue line) and the SOHO/EPHIN experimental data (red point) are shown.

figs. 5.15, 5.16, 5.17; systematic uncertainties are shown as a red shaded area. Fig. 5.18 reports the galactic proton spectra in the three periods as function of energy.

Each measured energy spectrum is compared with the theoretical prediction from the HelMod model in the same period, reporting also its maximum and minimum uncertainties. HelMod is a 2D Monte Carlo model to simulate the solar modulation of galactic cosmic rays. The model is based on the Parker transport equation which contains diffusion, convection, particle drift and energy loss; the latest review on HelMod was published in 2019 (Boschini M.J. et al., 2019).

For further comparison, each plot contains data from the SOHO/EPHIN spacecraft between 40 and 53 MeV (Muller-Mellin R. et al., 1995). The agreement between HEPD, other experimental data and theoretical forecast is good in all three considered periods, including both statistical and systematic uncertainties. The result can help constraining theoretical models of particle transport from the border of heliosphere, down to 1 AU.

From a comparison between the first spectrum (August 6, 2018 - January 15, 2019) and the last one (June 29, 2019 - January 5, 2020) an overall increase of 9% is observed (fig. 5.18), in good agreement with the variation

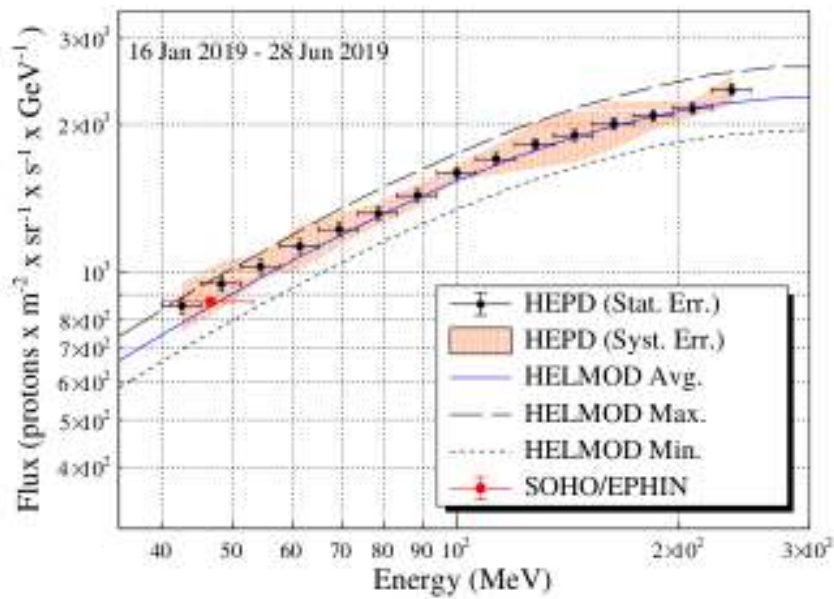


FIGURE 5.16: Galactic proton spectrum as function of energy in the period January 16, 2019 - June 28, 2019. Systematics uncertainties are present as a red shaded area. Also HelMod theoretical spectrum averaged over the corresponding period (blue line) and the SOHO/EPHIN experimental data (red point) are shown.

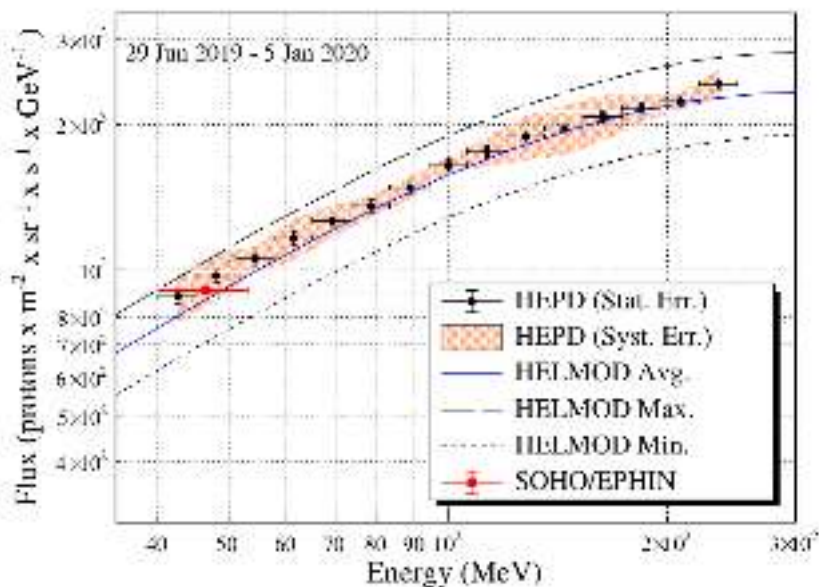


FIGURE 5.17: Galactic proton spectrum as function of energy in the period June 29, 2019 - January 5, 2020. Systematics uncertainties are present as a red shaded area. Also HelMod theoretical spectrum averaged over the corresponding period (blue line) and the SOHO/EPHIN experimental data (red point) are shown.

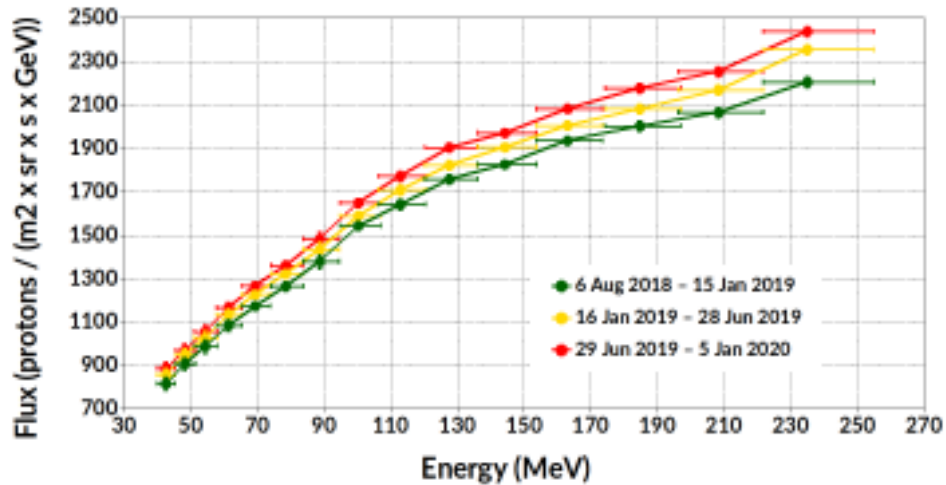


FIGURE 5.18: Galactic proton spectra as function of energy in the periods August 2018-January 2019, January 2019-June 2019, June 2019-January 2020. An increase between 2018 and 2020 is observed.

of SOHO/EPHIN data (8.5%). This trend can be explained with the effect of the solar modulation, lowering from 2018 to 2020, and causing a higher proton flux.

Conclusions

The work presented in this thesis described the tasks completed during the three years of my Ph.D., entirely in the framework of the CSES-Limadou collaboration, held in the clean rooms of Physics Department at University of Rome Tor Vergata.

The main targets of this work consist in reconstructing the several challenges and efforts which showed up in event reconstruction and data analysis, up to a good scientific reliability level, and in getting to the end with reasonable, although preliminary, results that can place the HEPD in an international scientific setting as a valid and needful experiment for CR physics community. Here phases and conclusions of this thesis are reported, together with some future perspectives for scientific data analysis.

The early stage of this work consisted in the MC software development, starting from the implementation of a detailed geometry and studying the main performance of the HEPD detector (acceptance and particle discrimination).

A very precise digitized ADC signal information was developed in the MC simulations. Exploiting the beam tests conducted on the flight model, MC software was tuned on the HEPD PMT response; the procedure required implementation of Geant4 optical physics list into MC software and study of elements involved in generation, transport and collection of optical photons inside all scintillator volumes and at PMT window; particular attention was given to the parameters of the scintillating materials, of the scintillator wrapping surface and of the geometry and quantum efficiency of PMT entrance window. The optical reconstruction revealed to be a good starting point for understanding HEPD internal processes and further data analysis possibilities.

On March 2018, with a group of Italian colleagues coming from other universities and institutions, I was involved in the commissioning phase for the online calibration of the HEPD, held at the Institute of Crystal Dynamics (ICD) in Beijing, China. This step was fundamental for the in-flight health check of the detector and its good development. The outcome of this phase

consisted in the freezing of the trigger configuration that would be used in the following data-taking period.

The work of analysis continued then with the energy reconstruction of a HEPD event with the usage of digitized MC in flight configuration. The MC digitization was important for the study of MC with the real response of the detector (including also electronic and physics effects), and was used for the analysis of selections applied to data and efficiency calculation. A method for energy determination, consisting in exploiting the last plane hit by the event to estimate its energy via simulation studies, was used as cross-check for energy reconstruction. During the last period of my research, I focused on calculation of a flux of galactic protons in three semiannual periods as function of energy; my presence at North-West University in Potchefstroom, South Africa was fundamental for analysis exchange ideas with groups involved in other CR experiments (PAMELA and AMS-02, for instance) and for the opening to international scientific community. Results are in very good agreement with another galactic proton experiment and with a theoretical model in all considered periods, taking into account both statistical and systematic uncertainties; also, a hint of time dependence due to solar modulation seems to be visible. The good reasonability of intermediate steps and the good agreement in calculation of proton flux makes this preliminary data analysis, despite ordinary difficulties, encouraging for future developments and analysis.

In conclusion, during these years, CSES-Limadou collaboration has integrated and tested a functioning detector for high-ionosphere analysis. Through a multi-method event reconstruction analysis, that was studied in detail, the group has also begun to produce the first scientific informations on galactic populations.

The main aims of the current period are now to identify and calculate the fluxes of the various particle populations detectable by the HEPD (galactic, trapped, quasi-trapped) and to confront its results in an international scientific environment. Another on-going activity is the study of proton fluxes inside the SAA. Older experiment results and theoretical model comparison will be of fundamental importance.

The CSES-Limadou collaboration is engaged with another project, still belonging to CSES missions. A second satellite is scheduled, named CSES-02. As the first one, it will investigate electromagnetic field and waves, plasma and particle perturbations and their correlation with geophysics activity: the

long-term target of the missions consist in the creation of a network of satellites orbiting around Earth to improve its observation from space.

In this framework, next steps will regard the integration of the detector HEPD-02 and the launch of CSES-02 in orbit, scheduled for March 2022. After the launch a dedicated analysis of HEPD-01 and HEPD-02 data will provide further information in ionospheric physics, energy spectra and composition of CR, belt particles stability and space weather phenomena.

The HEPD-02 project

This chapter is dedicated to the description of the HEPD-02 detector and the CSES-02 mission. In the framework of a collaboration program between CNSA and ASI, a second satellite is under development with the aim of seismo-electromagnetic observation from the space. It will be named CSES-02, in continuity with the first mission.

Among the payloads planned to be installed on the satellite, a particle detector is included. It will have the same scientific objectives of HEPD-01, and in particular to investigate energy spectrum and composition of CR, with particular reference to belts particles, to study space weather phenomena and to search for spatial and temporal stability of the inner Van Allen belts.

After a general introduction on the CSES-02 mission, the chapter describes in detail the instrument sub-detectors; a separated section is dedicated to the Monte Carlo software developed for the mission.

The CSES-02 mission

CSES-02 is a scientific mission dedicated to studying and monitoring electromagnetic field and waves, plasma and particles perturbations of ionosphere induced by natural sources and anthropocentric emitters and their correlation with geophysics activity.

CSES-02 satellite is now in advanced implementation stage and equipped with ten instruments: among them the High Energy Particle Detector (HEPD-02) and the Electric Field Detector (EFD-02) are being projected and will be assembled and integrated by the Italian group of the collaboration. With a dense chronological program, the launch is scheduled in March 2022; on March 23, 2019 the Memorandum Of Understanding between CNSA and ASI on CSES-02 cooperation was signed in Rome.

As the previous mission, CSES-02 is developed by CEA and INFN, together with several Chinese and Italian Universities and research Institutes. The two missions, CSES-01, currently in orbit, and CSES-02, in implementation stage, constitute together the first phase of the program.

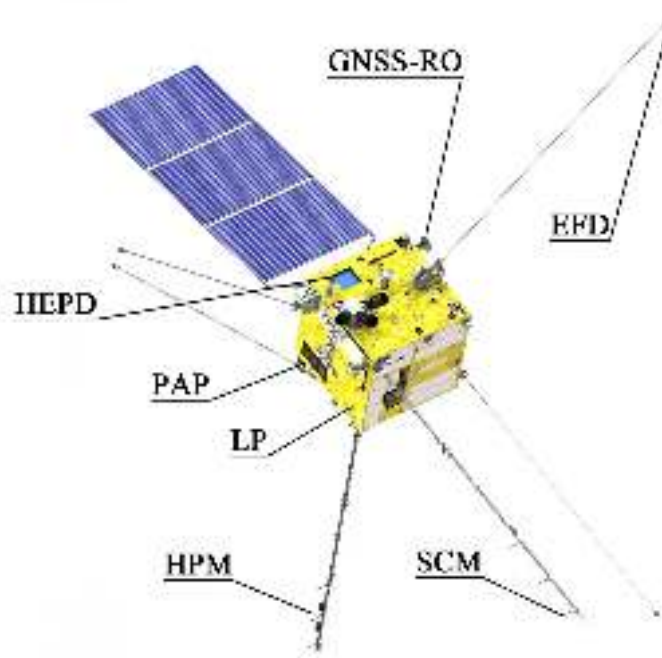


FIGURE 19: Configuration of CSES with the position of scientific payloads.

The Limadou collaboration constitutes the Italian participation to the CSES missions. It is funded by ASI and INFN, through a collaboration that includes several INFN sections (Bologna, Naples, Roma Tor Vergata, Torino), the INFN Center TIFPA of Trento, the INFN National Laboratories of Frascati, and several Universities: Bologna, Roma Tor Vergata, Torino, Trento, Uninettuno. INAF-IAPS, INGV, CNR-IFAC (Institute of Applied Physics) are also involved.

CSES-02 satellite is based on the Chinese CAST2000 platform. It has a mass of 900 kg and a peak power consumption of 900 W. The satellite will be placed at a 98° Sun-synchronous circular orbit at an altitude of about 500 km. It will move on the same orbital plane of CSES-01, with a phase shift of 180° with respect to the first satellite, in order to optimize the timing between two passages over the same site, and to reduce the temporal resolution. Data will be transmitted in X-band at 120 Mbps. The expected lifetime of the mission is 6 years.

The payloads on board consist of a Search-Coil Magnetometer (SCM) and a High Precision Magnetometer (HPM) to measure respectively the components and the total intensity of the magnetic field; an Electric Field Detector (EFD) to measure the electric field; a plasma analyzer and a Langmuir

Operative T	-10 / 35° C
Data budget	<= 100 Gb/day
Mass budget	< 45 kg
Energy range (e-)	3 - 100 MeV
Energy range (p)	30 - 200 MeV
Angular resolution	10° @ 3 MeV e-
Energy resolution	10% @ 5 MeV e-
Power budget	< 45 W
Scientific Data Bus	RS-422
Data Handling Bus	CAN 2.0
Life cycle	> 6 years

TABLE 2: HEPD-02 requirements.

probe to measure the disturbance of plasma in ionosphere; a GNSS Occultation Receiver and a Tri-Band Beacon to measure the density of electrons; a Ionospheric Photometer; a Low Energy Electron Spectrometer and a High-Energy Particle Detector (HEPD-02) to measure the particle flux and their energy spectrum.

All the instruments will operate along the whole orbit. Most payloads will collect data in two operating modes: "burst mode" and "survey mode". The burst mode is activated when the satellite passes over the whole China territory and the regions with a strong seismic activity, while over all the other areas the survey mode will be used.

The detector

The High-Energy Particle Detector (HEPD-02) will measure the increase of electrons, protons and light nuclei fluxes due to short-time perturbations of the radiation belts caused by solar, terrestrial and anthropic phenomena; other scientific goals comprise solar studies (modulation, SEP, CME, Forbush decrease) and investigation of the coupling between seismicity and Van Allen local instability. As in CSES-01, the High-Energy Particle Detector will be installed on the satellite with the entrance window pointing at Zenith. Table 2 shows the most important requirement of HEPD-02.

Fig. 20 shows the HEPD-02 structural design and fig. 21 shows the frontal view of the detector. The detector layout is composed by several components described in detail in the following.

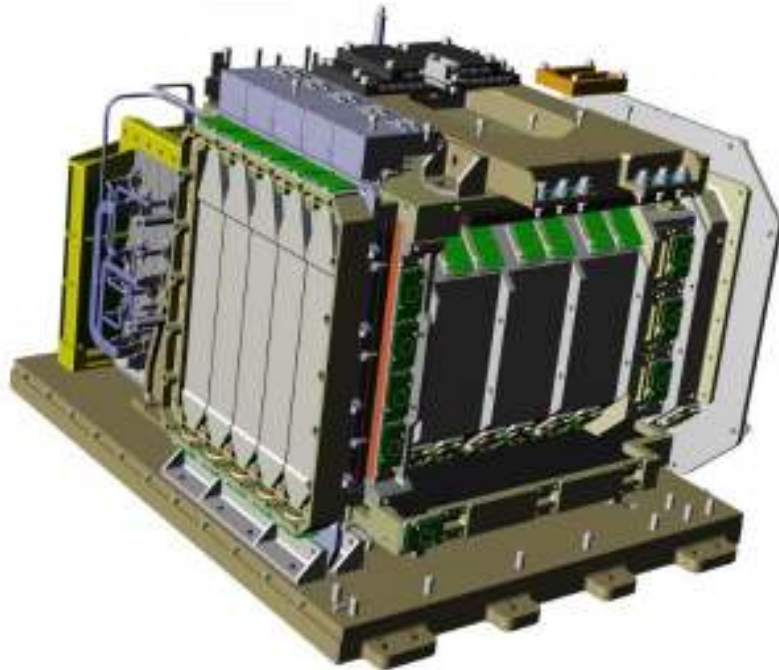


FIGURE 20: HEPD-02 structural design. One lateral veto plane has been removed to show the internal structure of the calorimeter.

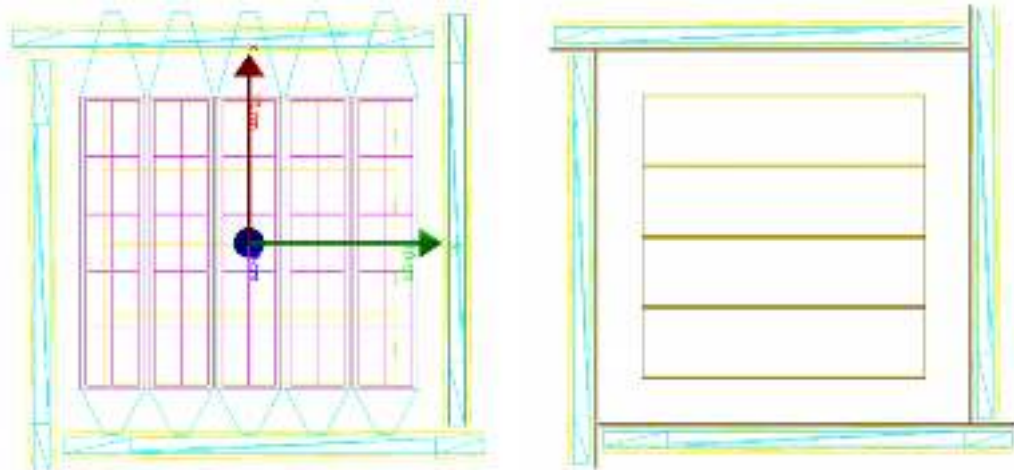


FIGURE 21: Left: HEPD-02 frontal view of the detector with the four lateral veto (cyan), the first trigger plane (blue), the tracker planes (magenta) and the second trigger plane (yellow). Right: HEPD-02 frontal view of the detector with the four lateral veto (cyan) and the only second trigger plane (brown).

Trigger detector

The trigger detector is composed of two scintillator planes: the first is a trigger plane made of 5 bars (dimensions $3.5 \times 16 \times 0.2 \text{ cm}^3$ each) read by means of light guides on both short sides, each of them terminating with a PMT; each bar is surrounded by a wrapping of aluminized mylar fixed with kapton tape; bars are separated each other and from the components adjacent to the plane by a composite plane in carbon. This plane is needed to generate a part of the trigger signal and to retrieve hit position and direction of the particle.

A second trigger plane of 4 bars (dimensions $3 \times 15 \times 0.8 \text{ cm}^3$ each) is read by two PMTs at opposite sides; each bar is surrounded by a wrapping of aluminized mylar fixed with kapton tape; bars are separated each other by a composite plane in carbon and from its adjacent components by composite carbon and a poron plane. The second plane is segmented in orthogonal direction to the first one to provide spatial information along the other coordinate.

Tracker

The tracker detector is made of ALPIDE CMOS pixel chip; ALPIDE is a $1.5 \times 3 \text{ cm}$ large MAPS (Monolithic Active Pixel Sensor) with 5012 rows \times 1024 columns $28 \mu\text{m} \times 28 \mu\text{m}$ pixels that are read out in a binary hit/no-hit fashion (Mager M. on behalf of the ALICE Coll., 2016). The detector is composed by 5 turrets; a single turret contains 3 planes, each with 2×5 sensors glued on a cold plate in carbon (see fig. 22). The whole tracker detector is separated from its adjacent components by a kapton plate. The aim of the tracker detector is the reconstruction of the direction of the particle, integrated by informations of the two trigger planes.

Calorimeter

The range calorimeter includes a tower of 12 plastic scintillator planes (dimensions $15 \times 15 \times 1.27 \text{ cm}^3$ each), divided in blocks of 4, and 2 planes each with 3 LYSO scintillator crystal crossed bars (dimensions $15 \times 15 \times 2.5 \text{ cm}^3$ each). Each plane of the tower and each LYSO bar is wrapped by an aluminized mylar fixed with kapton tape and is separated from its adjacent components by a poron plane; each block is separated from its adjacent components by a composite plane in carbon.

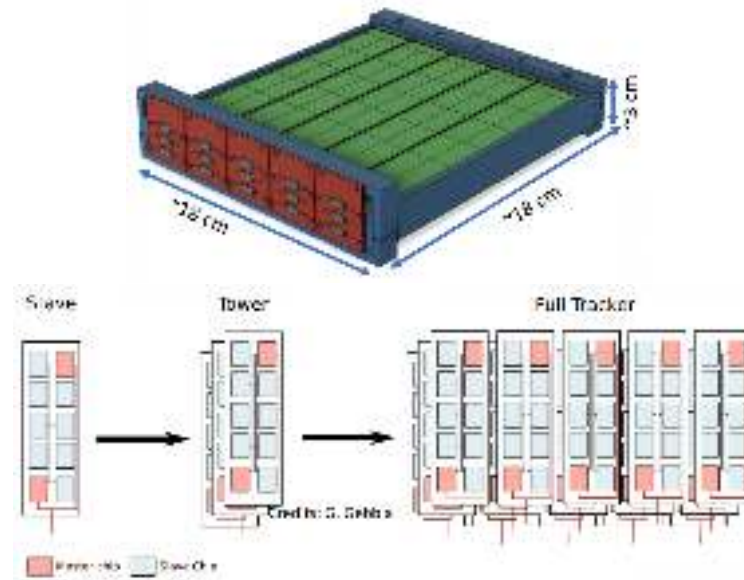


FIGURE 22: HEPD-02 tracker structural design (top) and electronic chips read out of stave, tower, tracker (bottom).

Veto detector

The veto detector is an anti-coincidence system, which surrounds the scintillator calorimeter and the second trigger plane, is made of 0.8 cm plastic scintillator veto planes. Each plane is wrapped by an aluminized mylar fixed with kapton tape and is separated from its adjacent components by composite carbon and a poron plane. These planes are used as containment planes.

Considering the fact that the major part of HEPD-02 scientific objectives are shared with the first one, the new detector's project was developed following the overall design of HEPD-01. However, some improvements were realized.

First of all, the direction determination has been remarkably strengthened by the addition of a further plane to the tracking system and of another segmented plane before the tracker, that is also included in the trigger logic; in this way, a triggered particle must necessarily pass throughout the tracking system for geometrical reasons. A second improvement in HEPD-02 was the removal of some passive materials (poron and carbon used in the mechanical structures) from the inside of the calorimeter: in HEPD-02 mechanical structures consist of plates of passive materials positioned between one scintillator planes.

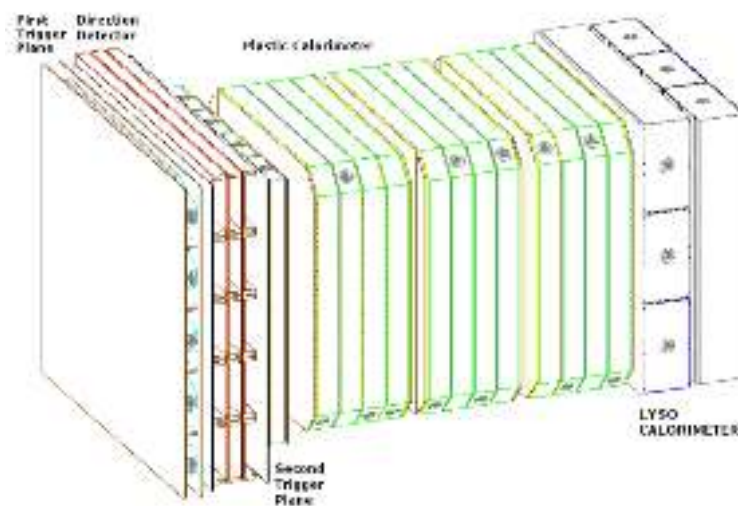


FIGURE 23: HEPD-02 Monte Carlo project design (CAD version dated December 23, 2019). Lateral veto planes are removed.

Monte Carlo software

Expected performances of HEPD-02 using different particles and energies were examined with a Monte Carlo software based on the Geant4 package (Allison, J. et al., 2006; Allison, J. et al., 2016). Fig. 23 shows the design of the detector geometry realized with the Geant4 Monte Carlo toolkit. Description and images reported in this work refer to CAD project version dated December 23, 2019.

The simulation software was realized and organized in several source files, each of them describing a particular set of the simulation:

- The detector geometry: active and passive elements are implemented, each one with its own material and dimensions; dimensions and distances are reproduced following the corresponding computer-aided design of the detector;
- the information about the primary particle: particle type, momentum direction, particle energy, generation positions; some configurations of particular importance (random generation, generation from plane, fixed point, ...) are already set;
- the physics lists;
- the output of the simulation (i.e., physical informations like energy or position).

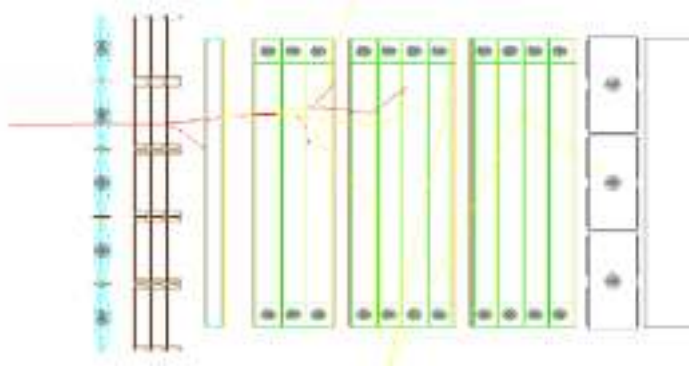


FIGURE 24: Simulated event of a 30 MeV electron entering perpendicularly to the detector window. tracks in red and in yellow represent electrons and photons respectively.

Detector geometry and primary particle informations can to be changed by a setup file separated from the source code.

Physics lists implemented in the software includes electromagnetic package, comprising all cross section phenomena in the interest range; predefined Geant4 physics packages were used (HadronElasticPhysics and IonElasticPhysics for elastic hadronic models, HadronPhysicsShielding and IonQMDPhysics for inelastic hadronic models); also optical physics is implemented, with the possibility of turning it on or off depending on necessity.

The output of the simulation is readable with ROOT data analysis software, with the format structured in an tree divided into branches; each branch stores an information about primary position, direction and energy, and deposited energies in each scintillator element.

Fig. 24 reports a simulated event of a 30 MeV electron entering perpendicularly to detector window.

HEPD-02 simulated performances

A simulation was carried out to study the performance of the detector. The simulated data set consisted in 1 million electrons and 1 million protons with uniform energy spectra, between 1 and 100 MeV and 1 and 300 MeV respectively, and angular spectra uniform in $\cos^2\theta$ in both cases. All following results, unless otherwise specified, refer to this data set.

Fig. 25 shows the minimum and maximum range detectable by the instrument, where minimum means energy thresholds for trigger and maximum

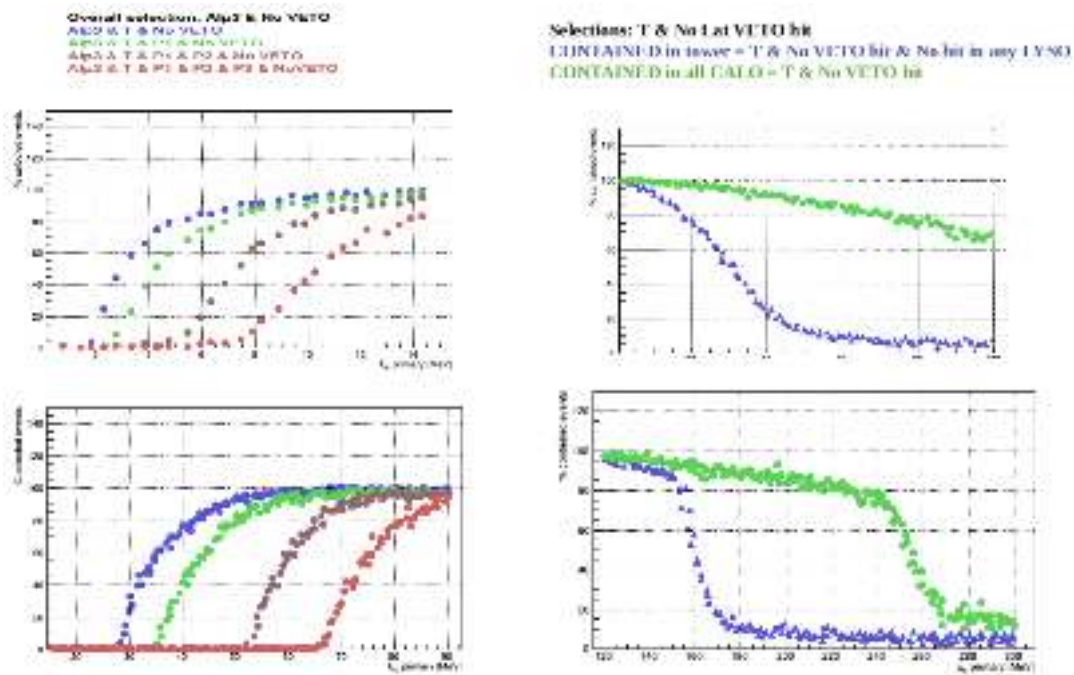


FIGURE 25: Left: Fraction (top) of electrons and (bottom) of protons passing some trigger conditions as a function of primary energy. Right: Fraction (top) of electrons and (bottom) of protons contained in the tower and in the calorimeter as a function of primary energy. In the legends, T stands for logic AND between energy release in first and in second trigger plane.

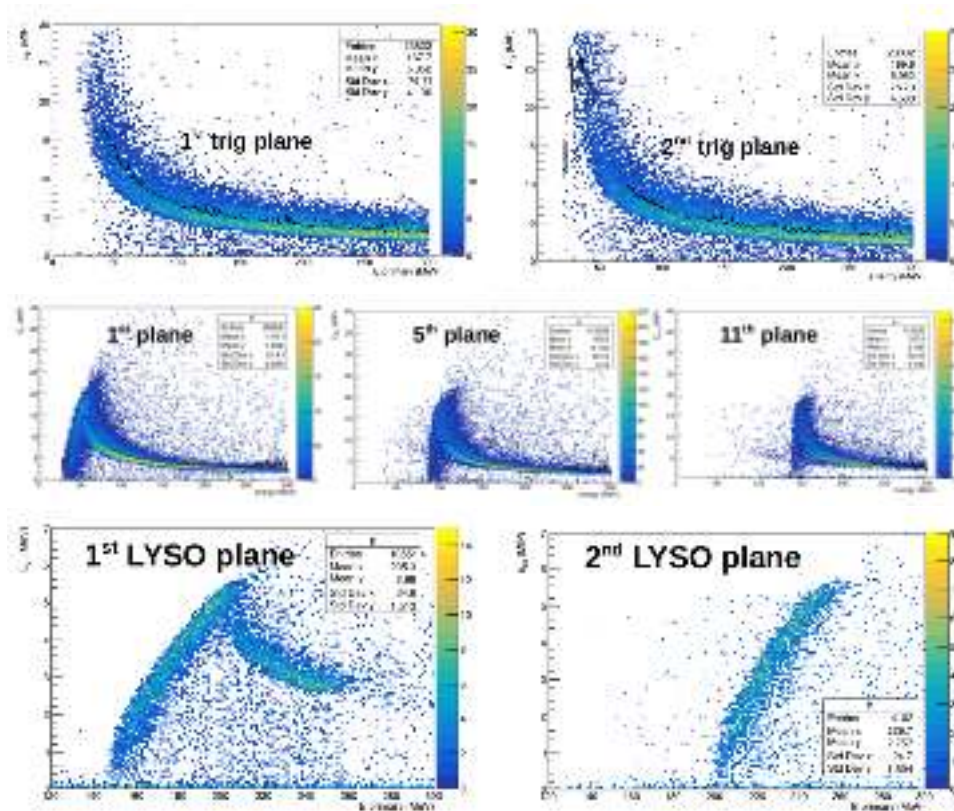


FIGURE 26: Energy in MIP-unit deposited in some scintillating elements (only some planes are shown) as function of primary energy for protons. Black points and error bars are the mean value of energy deposit in a certain bin of primary energy. The MIP value for each object is evaluated from fits in fig. 28.

means maximum energy at which an event is fully contained in the calorimeter. With respect to HEPD-01 (4.4), the energy thresholds are higher and the more planes are added to the trigger, the more the effect is visible; this can be explained to the greater quantity of material that must be traversed to generate the trigger. The maximum energy for full containment is similar for HEPD-01 and HEPD-02: the overall thickness is the same in both cases (16 planes of thickness 1 cm in the first case and 12 planes of thickness 1.3 cm in the second case).

The energy deposit in each scintillating element as function of the energy of the primary is represented in figs. 26 and 27 for protons and electrons respectively. Black points and error bars are the mean value of energy deposit in a certain bin of primary energy. The MIP deposited energy value for each element was evaluated as the energy deposit of a vertical 10 GeV proton (see fig. 28).

With respect to the first detector configuration, HEPD-02 design is projected to have a non negligible thickness before the tracking system, due to

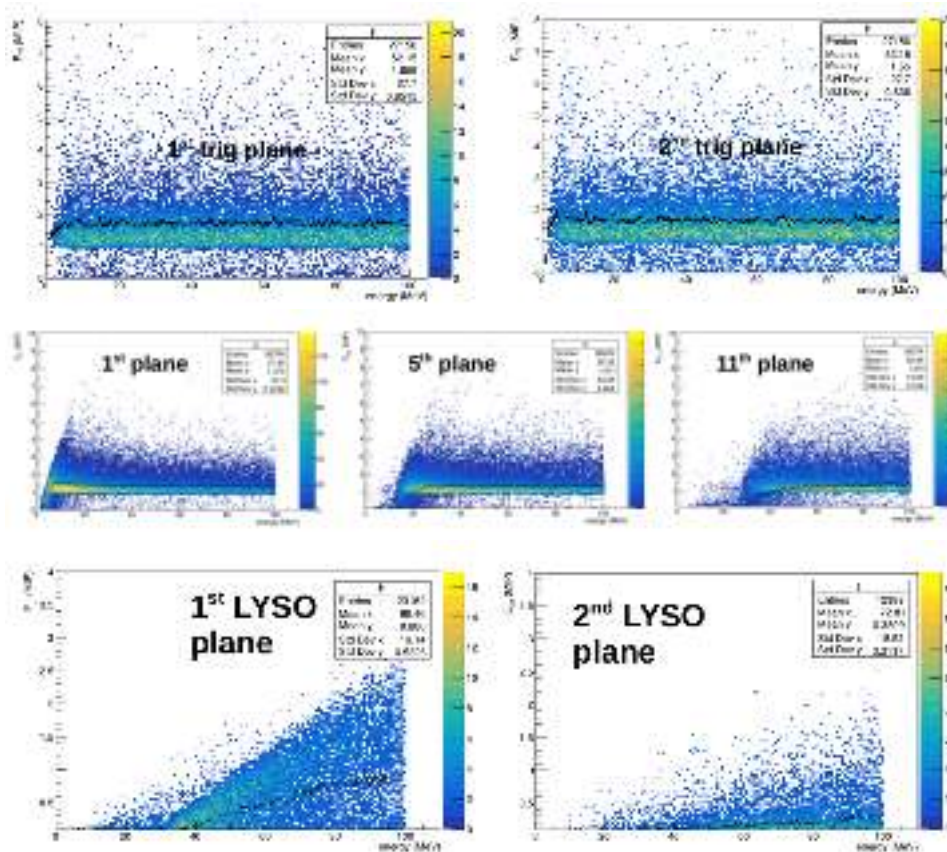


FIGURE 27: Energy in MIP-unit deposited in some scintillating elements (only some planes are shown) as function of primary energy for electrons. Black points and error bars are the mean value of energy deposit in a certain bin of primary energy. The MIP value for each object is evaluated from fits in fig. 28.

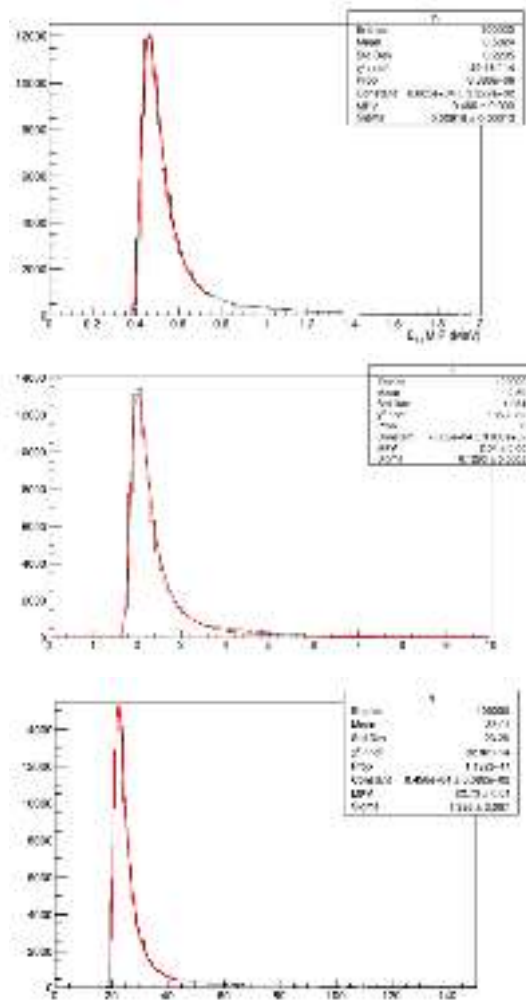


FIGURE 28: Deposit of energy respectively in one trigger bar (top), one calorimeter plane (center) and one LYSO bar (bottom) for a MIP particle (10 GeV, vertical proton). Distributions are fitted using a Landau function.

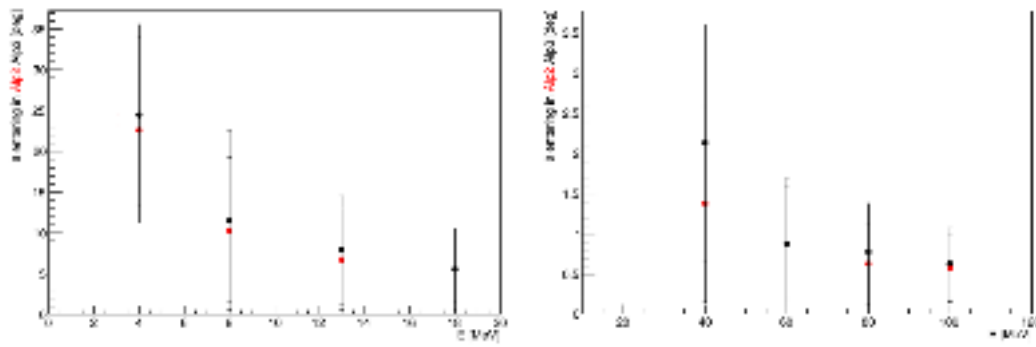


FIGURE 29: Multiple scattering effect for electrons (left) and protons (right). Y-axis shows the angle of the particle before entering in the 2nd Alpid plane (red) and before entering in the 3rd Alpid plane (black) for a vertically launched proton.

the presence of a 2 mm trigger plane and minor passive materials; it means that the original direction of the particle could be distorted because of multiple scattering in this thickness. Fig. 29 quantitatively reproduces this issue for electrons and protons; in the figure, Y-axis shows the angle of a vertically launched particle before entering in the 2nd Alpid plane and before entering in the 3rd Alpid plane, as function of energy. It can also be noted that multiple scattering due to protons, with respect to electrons, is much more negligible.

Fig. 30 reports the fraction of reconstructed energy for electrons in the range 2-10 MeV; deposited energy includes the release in all scintillating elements: the 2 trigger planes, the calorimeter tower and the 2 LYSO planes. In the whole range 2-10 MeV, a significant percentage of energy results lost (50% at 2 MeV, reducing to 20% at 10 MeV); the reason of this must be searched in the energy dispersion and to the presence of passive materials, that holds a predominant role for electrons at these energies; however, with a good MC simulator software, this energy loss can be efficiently reconstructed via unfolding procedures.

Because of the geometrical dimensions of the 2 trigger planes and the Alpid turrets, not every triggered event (i.e., event with energy release in both trigger planes) also passes for Alpid system. It results in an overall geometrical inefficiency of the tracking system. The evaluation of this inefficiency was calculated via MC software and its results are:

- the 35% of good events does not hit 1st Alpid plane;
- the 31% of good events does not hit either 1st or 2nd Alpid plane;

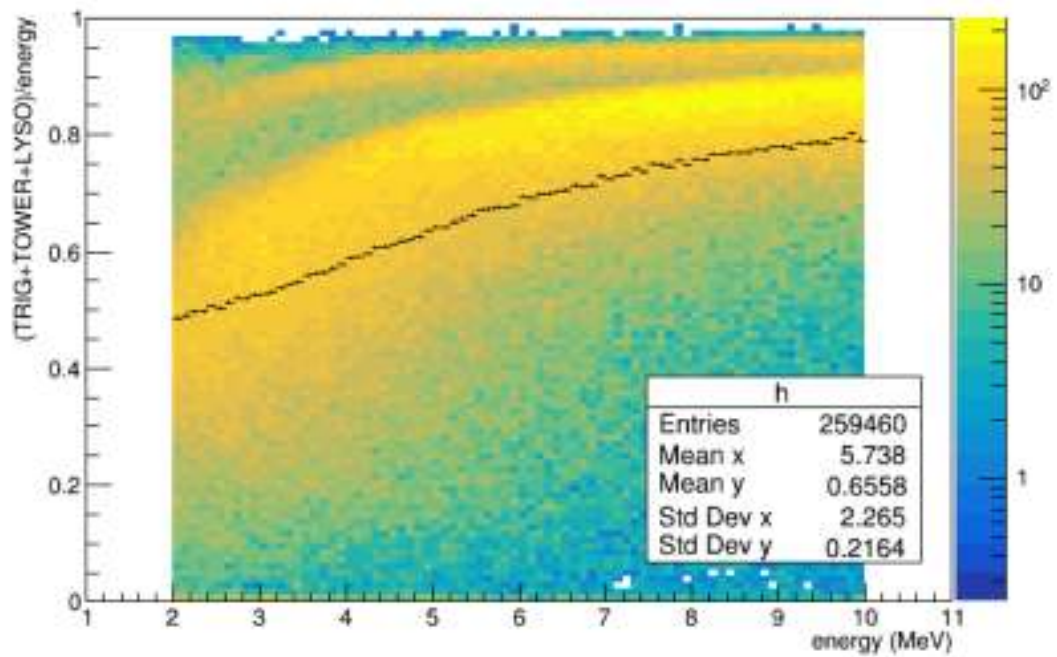


FIGURE 30: Fraction of energy deposited in the detector with respect to primary energy for electrons in range 2-10 MeV as function of primary energy; selections are: non-zero energy release in the 2 trigger planes and veto containment. Black points and error bars are the mean value of energy deposit in a certain bin of primary energy.

- the 26% of good events does not hit either 1st or 2nd or 3rd Alpile plane, i.e. does not release any information in the tracking system (see fig. 31);

where a "good event" means an event with a non-zero release of energy in the 2 trigger planes and in the first calorimeter plane and veto-contained.

LYSO radioactivity

LYSO material is a Cerium-doped Lutetium based scintillation crystal (chemical formula $\text{Lu}_{2(1-x)}\text{Y}_{2x}\text{SiO}_5$; see par. 3.1 in chapter 3 for more details). LYSO contains a naturally occurring radioactive isotope, ^{176}Lu , a β emitter. The decay results in a 3 gamma ray cascade of 307, 202 and 88 keV, where self-absorption of these photons results in the spectra in fig. 3.10 in a $1'' \times 1''$ LYSO cube.

The eventual possibility of a fake trigger due to a radioactive event was studied and examined in detail using MC.

At keV scale, photons only interact with matter via photoelectric effect; a radioactive photon secondary particle generated in LYSO material will be

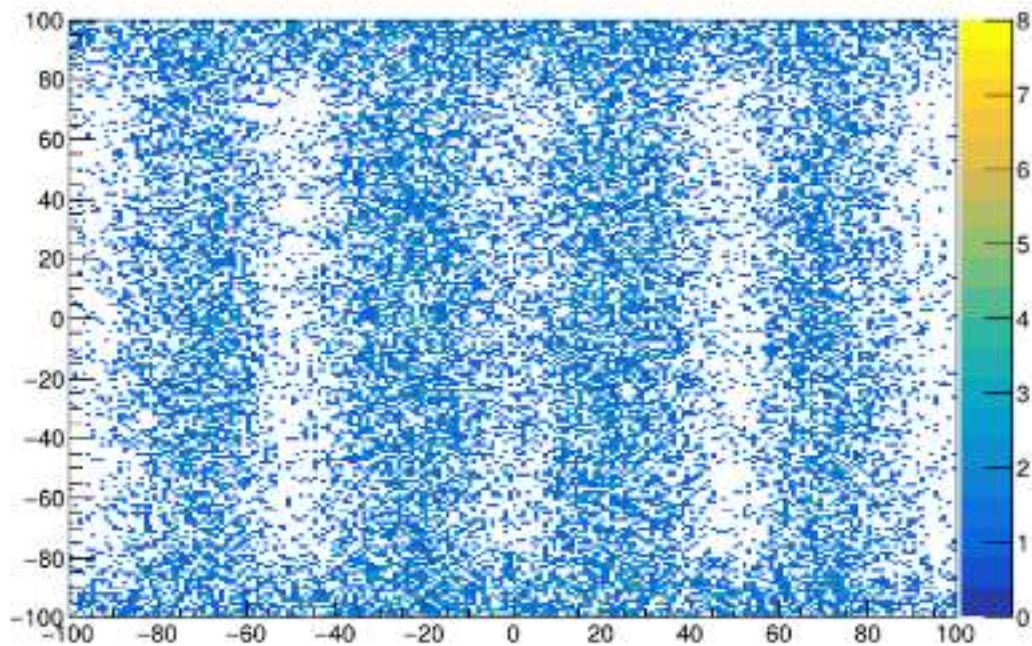


FIGURE 31: Generation surface of events with signal in both trigger planes, in the first calorimeter plane and veto-contained, but with no signal in any Alpide plane. Numbers on X- and Y-axis are in mm; colored Z-axis contains the number of entries.

then completely absorbed by LYSO material itself (photoelectric electrons don't have enough energy to exit from material) or traverse the whole calorimeter but release no signal being a neutral particle. Fig. 32 show the graphic visualization of 100 photons of 88, 202, 307 keV randomly generated in a LYSO bar of the first LYSO plane volume; none of them release a significant signal in the trigger planes, or even in the 1st calorimeter plane. Also beta-particles (energy spectrum in fig. 33 left) don't give any trigger; electrons with this energy can't reach the first calorimeter planes (see fig. 33 right).

Another effect involved in LYSO radioactivity is the energy deposition contribution of the radioactive event during a trigger data acquisition of a real event. The LSO radioactive rate is estimated as 307 Bq/ml (Wei Q., 2015). In the volume of $15 \times 15 \times 5 \text{ cm}^3$ of LYSO material, hypotizing a trigger window of about 50 ns, 0.017 decays are forseen in the trigger window; it means that, in 10 thousand events, $\simeq 170$ include a decay event. In a simulation of 10^4 protons of 10 GeV, vertical to the detector window, in 170 of them was included also a decay primary (88, 202, 307 keV gammas and an electron with maximum energy 596 keV, isotropic emission, generated randomly in

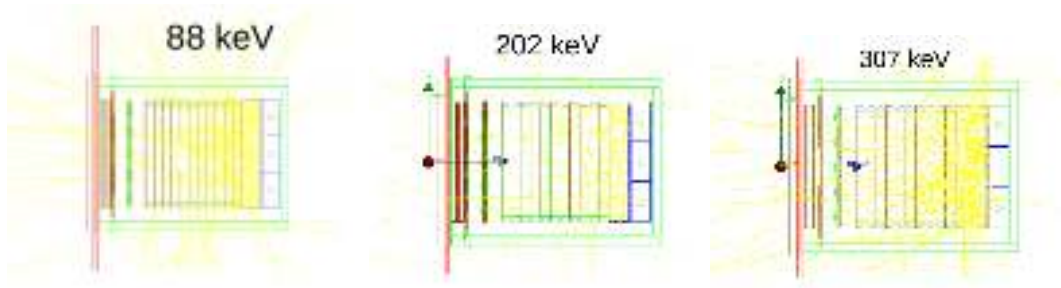


FIGURE 32: MC graphic visualization of 100 photons of 88 keV, 100 photons of 202 keV, and 100 photons of 307 keV photons (yellow tracks), randomly generated in a LYSO bar of the first LYSO plane volume.

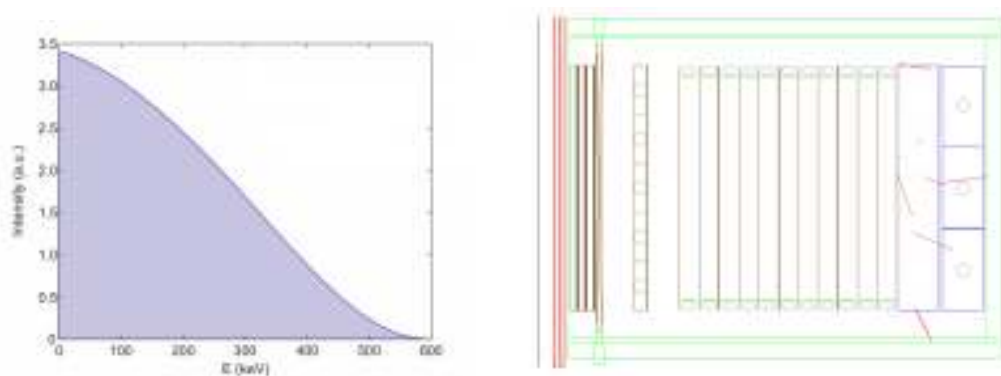


FIGURE 33: Left: energy spectrum of beta particles from radioactive ^{176}Lu decay; right: MC graphic visualization of 100 electrons (red tracks) with energy in range 0-596 keV, randomly generated in a LYSO bar of the first LYSO plane volume.

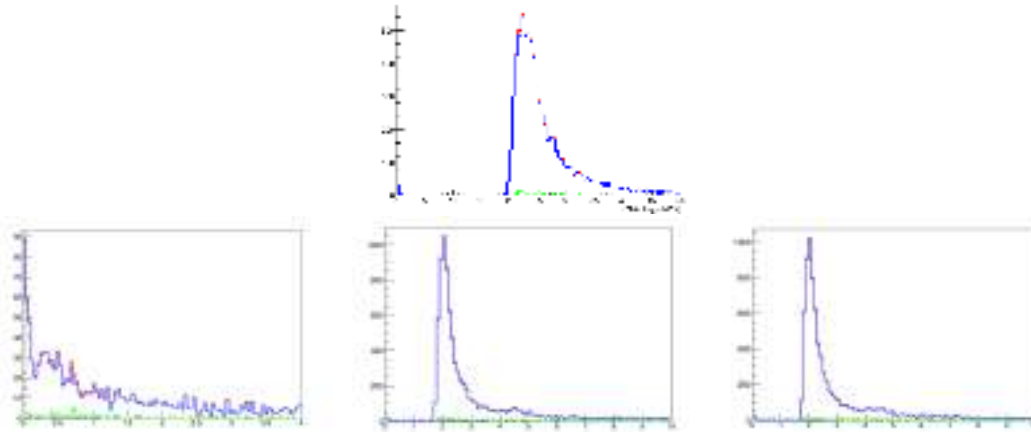


FIGURE 34: Deposited energy distribution in (top) the LYSO central bar of first plane, (bottom) in the LYSO adjacent bar of first plane and (bottom and bottom) in 2 planes of the calorimeter next to LYSO (P10 and P11) for all events (in red), events without decay (blue) and events with decay (green).

all volume). The results of the simulation exclude the possibility of an energy release that could modify the energy deposition of real events (fig. 34).

Publications

Here follows a list of articles, published by the author during the Ph.D. years:

- G. Ambrosi et al., "The HEPD particle detector of the CSES satellite mission for investigating seismo-associated perturbations of the Van Allen belts", *Science China Technological Sciences*, Volume 61, pp. 643-652 (2018)
- L. Carfora on behalf CSES/HEPD collaboration, "MC simulation of the High Energy Particle Detector on board the satellite CSES", *EPJ Web of Conferences*, Volume 209 (2019)
- P. Picozza et al., "Scientific goals and in-orbit performance of the High-Energy Particle Detector on board the CSES satellite", *The Astrophys. J. Suppl. Series*, Volume 243 (2019)
- Sotgiu A. et al., "Status and performance of the High Energy Particle Detector (HEPD) onboard the CSES-01 satellite", *Proceedings of Science, ICRC 2019*
- Scotti V. et al., "The High Energy Particle Detector (HEPD-2) on board the CSES-2 satellite", *Proceedings of Science, ICRC 2019*
- G. Ambrosi et al., "Beam test calibrations of the HEPD detector on board the China Seismo-Electromagnetic Satellite", *Nucl. Instr. Methods in Phys. Res. A*, Volume 974 (2020)
- S. Bartocci et al., "Galactic Cosmic-Ray Hydrogen Spectra in the 40-250 MeV Range Measured by the High-Energy Particle Detector (HEPD) on board the CSES-01 Satellite between 2018 and 2020", *The Astrophysical Journal*, Volume 901:8 (2020)

Here is a list of conferences attended by the author during the Ph.D. years and the correspondent contribution:

- Talk "HEPD: a new detector for particle and cosmic ray physics" at XIX Frascati Spring School "Bruno Touschek" in Nuclear, Subnuclear and Astroparticle Physics, Frascati, May 7-11, 2018
- Poster "MC simulation of HEPD detector. Performances and beam test analysis" at Roma International Conference on Astroparticle Physics RICAP 2018, Rome, September 2018

- Poster "Monte Carlo simulation of the HEPD of the space mission CSES-Limadou. Performances and calibration procedure" at Incontri di Fisica delle Alte Energie IFAE 2019, Naples, April 8-10, 2019
- Talk "The High-Energy Particle Detector on the space mission CSES-Limadou. Performance and calibration procedures" at 105th Congresso Nazionale SIF, L'Aquila, September 27, 2019

Bibliography

- A. W. Strong I. V. Moskalenko, V. S. Ptuskin (2007). “Cosmic-Ray Propagation and Interactions in the Galaxy”. In: *Ann. Rev. Nucl. and Part. Sci.* 57, pp. 285–327.
- Agostinelli, S. et al. (2003). “Geant4 - a simulation toolkit”. In: *Nucl. Instr. Meth. Phys. Res. A* 506, pp. 250–303.
- Aleksandrin S. Yu et al. (2003). “High-energy charged particle bursts in the near-Earth space as earthquake precursors”. In: *Annales Geophysicae* 21, pp. 597–602.
- Allison, J. et al. (2006). “Geant4 developments and applications”. In: *IEEE Transactions on Nucl. Sci.* 53.1, pp. 270–278.
- (2016). “Recent developments in Geant4”. In: *Nucl. Instr. Meth. Phys. Res. A* 835, pp. 186–225.
- Ambrosi G. et al. (2018). “The HEPD particle detector of the CSES satellite mission for investigating seismo-associated perturbations of the Van Allen belts”. In: *Sci. China Tech. Sci.* 61, pp. 643–652.
- Ambrosi, G. et al. (2019). “Beam test calibrations of the HEPD detector on board the China Seismo-Electromagnetic Satellite”. In: *Nucl. Instr. and Meth.* (AMS02 Collab.), M. Aguilar et al. (2015a). “Precision Measurement of the Helium Flux in Primary Cosmic Rays of Rigidities 1.9 GV to 3 TV with the Alpha Magnetic Spectrometer on the International Space Station”. In: *Phys. Rev. Lett.* 115, p. 211101.
- (2015b). “Precision Measurement of the Proton Flux in Primary Cosmic Rays from Rigidity 1 GV to 1.8 TV with the Alpha Magnetic Spectrometer on the International Space Station”. In: *Phys. Rev. Lett.* 114, p. 171103.
- Antcheva, I. et al. (2009). “ROOT - A C++ framework for petabyte data storage, statistical analysis and visualization”. In: *Computer Physics Communications* 180.12, pp. 2499–2512.
- (ATIC Collab.), A. D. Panov et al. (2009). “Energy spectra of abundant nuclei of primary cosmic rays from the data of ATIC-2 experiment: Final results”. In: *Bull. Russian Acad. of Science, Physics* 73.5, pp. 564–567.

- B. Heber et al. (2009). "Modulation of galactic cosmic ray protons and electrons during an unusual solar minimum". In: *Astrophys. J.* 699.2, pp. 1956–1963.
- B. T. Tsurutani et al. (1997). "Interplanetary Causes of Great and Superintense Magnetic Storms". In: *Geophys. Monogr. Ser. AGU Washington* 98, p. 266.
- Balogh et al. (2008). "Decrease in heliospheric magnetic flux in this solar minimum: Recent Ulysses magnetic field observations". In: *GeoPhys. Res. Letters* 35.22103, p. 4.
- (BESS Collab.), K. Abe et al. (2016). "Measurements of Cosmic-Ray Proton and Helium Spectra from the BESS-Polar Long-duration Balloon Flights over Antarctica". In: *Astrophys. J.* 822.2.65.
- Boschini M.J. et al. (2019). "The HelMod model in the works for inner and outer heliosphere: From AMS to Voyager probes observations". In: *Advances in Space Research* 64, pp. 2459–2476.
- Cao J. B. et al. (2018). "The electromagnetic wave experiment for CSES mission: Search coil magnetometer". In: *Sci. China Tech. Sci.* 61.5, pp. 653–658.
- Cecchini S. et Spurio, M. (2012). "Atmospheric muons: experimental aspects". In: *Geosci. Instrum. Method. Data Syst.* 1, pp. 185–196.
- (CREAM Collab.), H. S. Ahn et al. (2009). "Energy Spectra of Cosmic-Ray Nuclei at High Energies". In: *Astrophys. J.* 707, pp. 593–603.
- (CRN Collab.), D. Müller et al. (1991). "Energy spectra and composition of primary cosmic rays". In: *Astrophys. J.* 374, pp. 356–365.
- D. M. Sawyer, J. I. Vette (1976). "AP-8 Trapped Proton Environment for Solar Maximum and Solar Minimum". In: *NSSDC/WDC-A-R*.
- D. Pisa, M. Parrot and O. Santolik (2018). "Ionospheric density variations recorded before the 2010 Mw 8.8 earthquake in Chile". In: *J. Geophys. Res.* 116, p. 8.
- D'Agostini, G. (2010). "Improved Iterative Bayesian unfolding". In: *arXiv:1010.0632*.
- E. Thèbault et al. (2015). "International Geomagnetic Reference Field: the 12th generation". In: *Earth, Planet and Space* 67.
- Fermi, E. (1949). "On the Origin of the Cosmic Radiation". In: *Phys. Rev.* 75.8, pp. 1169–1174.
- (HEAO3-C2 Collab.), J. J. Engelmann et al. (1990). "Charge composition and energy spectra of cosmic-ray nuclei for elements from Be to Ni - Results from HEAO-3-C2". In: *Astron. & Astrophys.* 233, pp. 96–111.
- (HESS Collab.), F. Aharonian et al. (2007). "First ground-based measurement of atmospheric Cherenkov light from cosmic rays". In: *Phys. Rev. D* 75, p. 042004.

- Hesse, V. (1912). "Über Beobachtungen der durchdringenden Strahlung bei sieben Freiballonfahrten". In: *Physikalische Zeitschrift* 13, pp. 1084–1091.
- J. F. Valdés-Galicia, L. X. Gonzalez (2016). "Solar modulation of low energy galactic cosmic rays in the near-earth space environment". In: *Advances in Space Research* 57, pp. 1294–1306.
- (JACEE Collab.), K. Asakimori et al (1998). "Cosmic-Ray Proton and Helium Spectra: Results from the JACEE Experiment". In: *Astrophys. J.* 502.1, pp. 278–283.
- Kane, R. P. (2002). "Some Implications Using the Group Sunspot Number Reconstruction". In: *Solar Physics* 205.2, pp. 383–401.
- L. Wang et al. (2015). "Preliminary proposal of scientific data verification in CSES mission". In: *Earthq. Sci.* 28.4, pp. 303–310.
- Lario et al. (2013). "Intense solar near-relativistic electron events at 0.3 AU". In: *Journal of Geophys. Res.: Space Physics* 118, p. 11.
- Longhair, M. S. (1981). *High energy astrophysics*. Cambridge University Press.
- M. E. Aleshina et al. (1992). "Correlation between earthquake epicenters and regions of high-energy particle precipitations from the radiation belt". In: *Cosmic Res.* 30, pp. 65–68.
- M. Piersanti et al. (2017). "Comprehensive Analysis of the Geoeffective Solar Event of 21 June 2015. Effects on the Magnetosphere, Plasmasphere and Ionosphere System". In: *Solar Phys.* 169.
- Mager M. on behalf of the ALICE Coll. (2016). "ALPIDE, the Monolithic Active Pixel Sensor for the ALICE ITS upgrade". In: *Nucl. Instr. and Meth. Phys. Res. A* 824, pp. 434–438.
- Muller-Mellin R. et al. (1995). "COSTEP - Comprehensive Suprathermal and Energetic Particle Analyser". In: *Solar Physics* 162, pp. 483–504.
- N. A. Tsyganenko (1989). "A magnetospheric magnetic field model with a warped tail current sheet". In: *Planetary and Space Science* 37, pp. 5–20.
- P. Picozza et al. (2019). "Scientific Goals and In-orbit Performance of the High-energy Particle Detector on Board the CSES". In: *Astroph. J. Suppl. Series* 243.16.
- (PAMELA Collab.), O. Adriani et al. (2011). "PAMELA Measurements of Cosmic-ray Proton and Helium Spectra". In: *Science* 332, pp. 69–72.
- (2015). "Re-entrant albedo Proton Fluxes Measured by the PAMELA Experiment". In: *J. of Geophys. Res. - Space Physics*. URL: <https://arxiv.org/abs/1504.06253>.
- Peretti E. et al. (2019). "Cosmic ray transport in Starburst Galaxies and possible observables". In: *Proceedings of Science (ICRC 2019)* 382.

- Picozza, P. et al. (2017). "HEPD: a particle detector for the CSES space mission". In: *Proc. of Science ICRC 2017, 12-20 July BEXCO*.
- Piersanti M. and Villante U. (2016). "On the discrimination between magnetospheric and ionospheric contributions on the ground manifestation of sudden impulses". In: *Journal of GeoPhys. Res.: Space Physics* 121, The cosmic-ray albedo.
- R. Battiston and V. Vitale (2013). "First evidence for correlations between electron fluxes measured by NOAA-POES satellites and large seismic events." In: *Nucl. Phys. B Proceedings Suppl.* Pp. 1–10.
- R.A. Nymmik et al. (1996). "Galactic cosmic ray flux simulation and prediction". In: *Adv. Space Res.* 17.2.
- (RUNJOB Collab.), V. A. Derbina et al. (2005). "Cosmic-Ray Spectra and Composition in the Energy Range of 10-1000 TeV per Particle Obtained by the RUNJOB Experiment". In: *Astrophys. J.* 628.1, pp. L41–L44.
- S. Basu et al. (2002). "GPS proxy model for real-time UHF satellite communications scintillation maps from the Scintillation Network Decision Aid (SCINDA)". In: *Radio Science* 39.
- Sotgiu, A. (2018). "Development of the control and data handling software for the High-Energy Particle Detector and preliminary data analysis". In: *PhD Thesis Univ. Tor Vergata*.
- Space Aeronomy, Belgian Institute for. *SPENVIS*. <https://www.spENVIS.oma.be/help/background/background.html>. [Online].
- Sullivan, J.D. (1971). "Geometrical factor and directional response of single and multi-element particle telescopes". In: *Nucl. Instrum. Method.* 95, pp. 5–11.
- The Pierre Auger Collab. (2007). "Correlation of the Highest-Energy Cosmic Rays with Nearby Extragalactic Objects". In: *Science* 318.5852, pp. 938–943.
- (TRACER Collab.), M. Ave et al. (2008). "Composition of Primary Cosmic-Ray Nuclei at High Energies". In: *Astrophys. J.* 678.1, pp. 262–273.
- Treiman, S. B. (1953). In: *Phys. Rev.* 91.
- V. Sgrigna et al. (2002b). "Preseismic natural emissions from the Earth's surface and their effects in the near Earth space. A project for monitoring earthquake from space". In: *EOS Trans. AGU* 83.
- (2005). "Correlations between earthquakes and anomalous particle bursts from SAMPEX/PET satellite observations". In: *Journal of Atmospheric and Solar-Terrestrial Physics* 67.15, pp. 1448–1462.

- Vette, J. I. (1991). *The AE-8 Trapped Electron Model Environment*. NSSDC/WDC-A-R&S 91-24.
- Wei Q. (2015). "Intrinsic Radiation in Lutetium Based PET Detector: Advantages and Disadvantages". In: *arXiv: Instrumentation and Detectors*.
- X. Q. Li et al. (2018). "The high-energy particle package on board CSES". In: *Radiation Detection Technology and Methods* 3.22.
- X. Shen et al. (2011). "The earthquake-related disturbances in ionosphere and project of the first China seismo-electromagnetic satellite". In: *Earthq. Sci.* 24, pp. 639–650.
- (2018). "The state-of-the-art of the China Seismo-Electromagnetic Satellite mission". In: *Sci. China Tech. Sci.* 61.5, pp. 634–642.
- X. Zhang et al. (2013). "Burst increases of precipitating electrons recorded by the DEMETER satellite before strong earthquakes". In: *Nat. Hazards Earth Syst. Sci.* 13, pp. 197–209.